12-15-2014

Measurement of Polarization Observables P_z, P^s_z, and P^c_z in Double-Pion Photoproduction Off the Proton

Yuqing Mao
University of South Carolina - Columbia

Measurement of Polarization Observables P_z, P_z^s, and P_z^c in Double-Pion Photoproduction off the Proton

by

Yuqing Mao

Bachelor of Science
Soochow Univeristy 2007

Submitted in Partial Fulfillment of the Requirements

for the Degree of Doctor of Philosophy in

Physics

College of Arts and Sciences

University of South Carolina

2014

Accepted by:

Steffen Strauch, Major Professor

Volker Credé, Committee Member

Ralf Gothe, Committee Member

Jeffery R. Wilson, Committee Member

Lacy Ford, Vice Provost and Dean of Graduate Studies

Acknowledgments

This thesis could not have been possible without the help and support of many people. Professor Steffen Strauch offered me the opportunity to work with him, instructed me on the research, and provided me with continuous guidance. Professor Yordanka Ilieva helped me in many areas, including methodology and inspiration throughout the years while I was at the University of South Carolina. Many thanks to Dr. Nicholas Zachariou who helped me out with many analysis details and to the FROST group at Jefferson Lab for their help and insights about the polarized target and analysis of the g9 data. I am also very thankful to all the members of my Ph.D. Examining Committee for their kind and helpful comments throughout the years of my Ph.D. research.

Abstract

Meson production from excited nucleons is important in the study of baryon resonances and pion photoproduction is attracting much attention. To date a rather large amount of unpolarized cross-section measurements have been reported for both single- and double-pion photoproduction. However, polarization observables provide complementary information as they probe different combinations of transition amplitudes. The database for polarization observables remains quite sparse. Double-pion photoproduction have been studied in Hall B at Jefferson Lab with linearly polarized tagged photon beams incident on longitudinally polarized protons. The experiment covered center-of-mass energies between 1.4 GeV and 2.3 GeV. The target was a FROzen Spin butanol Target (FROST) and the final-state particles were detected by the CEBAF Large Acceptance Spectrometer (CLAS). In various polarization configurations, asymmetries of the experimental yields are constructed to extract polarization observables. In order to evaluate the background from unpolarized bound nucleons in the butanol target, the data collected from an additional unpolarized carbon target is used. A set of single- and double-polarization observables, P_z, P_z^s and P_z^c were extracted; the double-polarization observables for the first time. The double-pion observables show even or odd symmetries, as expected by parity conservation, and are compared with results of an effective Lagrangian model by A. Fix. The model predictions have the same symmetry behavior as the data and resemble main features of the data in most kinematic bins. In the comparison with models, the data test our understanding of the nucleon structure, establishes nucleon excitation and non-resonant reaction amplitudes, and possibly help to identify new baryon resonances.

Table of Contents

List of Tables

List of Figures

Chapter 1

Introduction

The study and investigation of the world's micro structure and characteristics is of essential importance for the development of the understanding of the world we are living in. Baryons have attracted much attention for the key value to reveal the standard model, the strong force, and the underlying theory of Quantum chromodynamics (QCD). Despite numerous experiments and theoretical studies on the topic, unsolved questions on baryon resonances remain and are the motivation for further research.

1.1 Standard Model and QCD

The theories and discoveries of thousands of physicists have resulted in a remarkable insight into the fundamental structure of matter: ordinary matter in the universe is found to be made of a few basic building blocks called fundamental particles, quarks and leptons, governed by four fundamental forces (the strong, weak, electromagnetic, and gravitational forces). The best understanding of how these particles and three of the forces (not including gravity) interact with each other is encapsulated in the Standard Model of particle physics. Developed in the early 1970s, it has successfully explained almost all experimental results and precisely predicted a wide variety of phenomena. Over time and through many experiments, the Standard Model has become established as a well-tested physics theory.

Quantum chromodynamics (QCD) is a quantum field theory describing the interactions between color charged quarks and gluons which make up hadrons (baryons

and mesons). Quarks carry one of three different color charges and one of six flavor quantum numbers (up, down, strange, charm, bottom, and top). QCD is a non-abelian gauge theory with color $SU(3)$ symmetry. The theory is an important part of the Standard Model of particle physics. A huge body of experimental evidence for QCD has been gathered over the years [1].

1.2 Baryon spectroscopy

Baryons are strongly interacting fermions with the baryon number B equal to 1. In addition to the nucleons, there are other baryon families, like the Δ particles, Λ particles, Σ particles, and Ξ particles [2]. All baryons except of the proton are unstable. The proton has a lifetime exceeding approximately 10^{29} years. Unstable baryons will eventually decay into protons.

Baryons containing up, down, and strange quarks (u, d, and s) with strangeness quantum number S and electric charge Q can be organized into an octet, for baryons with spin 1/2, and into a decuplet, for baryons with spin 3/2. These representations are based on the antisymmetric wave-function and the symmetric behavior of the flavor quantum number. The octet and decuplet are representations of the of the $SU(3)$ flavor group. Figures 1.1 and 1.2 show the decuplet and octet baryons.

Baryon spectroscopy is concerned with the study of the properties of baryons, especially their masses and decays. These studies have provided essential clues that led to the development of QCD. The measurement of the spectrum of the excited states of the nucleons is also providing insight into their structure and internal degrees of freedom.

Figure 1.3 compares the experimental N-resonance spectrum with calculations in the framework of a relativistic quark model [4]. While the model describes well the lowest-mass resonances for each total spin and parity, J^π, it predicts many more states at higher masses than have experimentally been observed. This is the well-

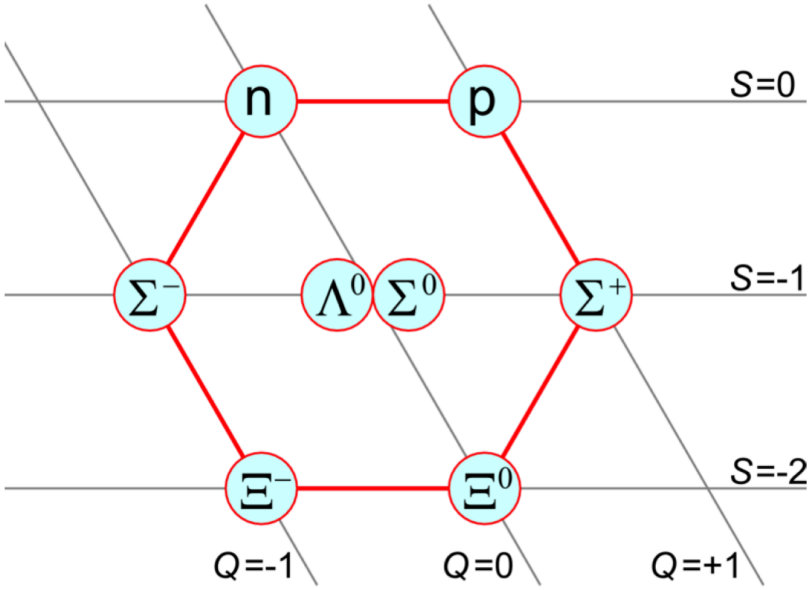

Figure 1.1 Octet: Baryons composed of u, d, and s quarks with spin-1/2 are classified based on the strangeness flavor quantum number and the electric charge. The figure is from Ref. [3].

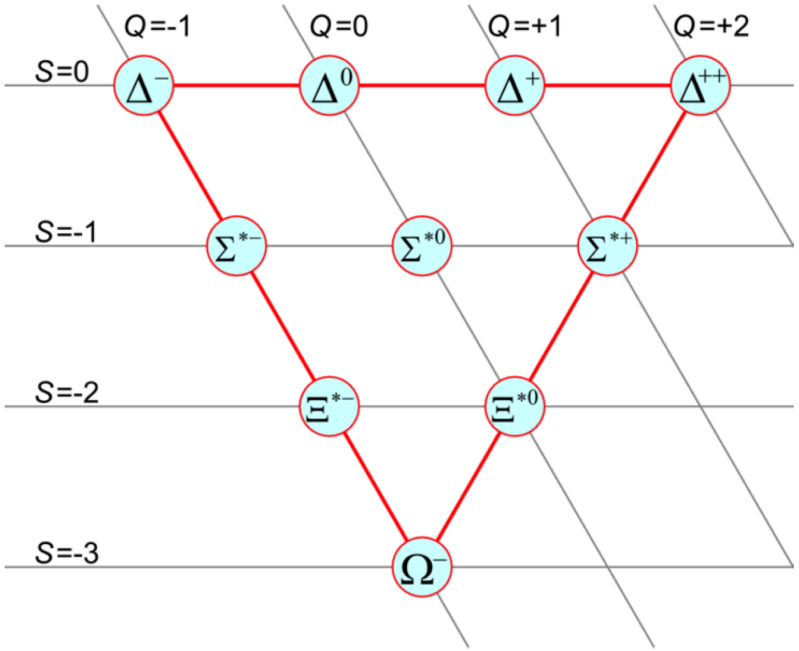

Figure 1.2 Decuplet: Baryons composed of u, d, and s quarks with spin-3/2 are classified based on the strangeness flavor quantum number and the electric charge. The figure is from Ref. [3].

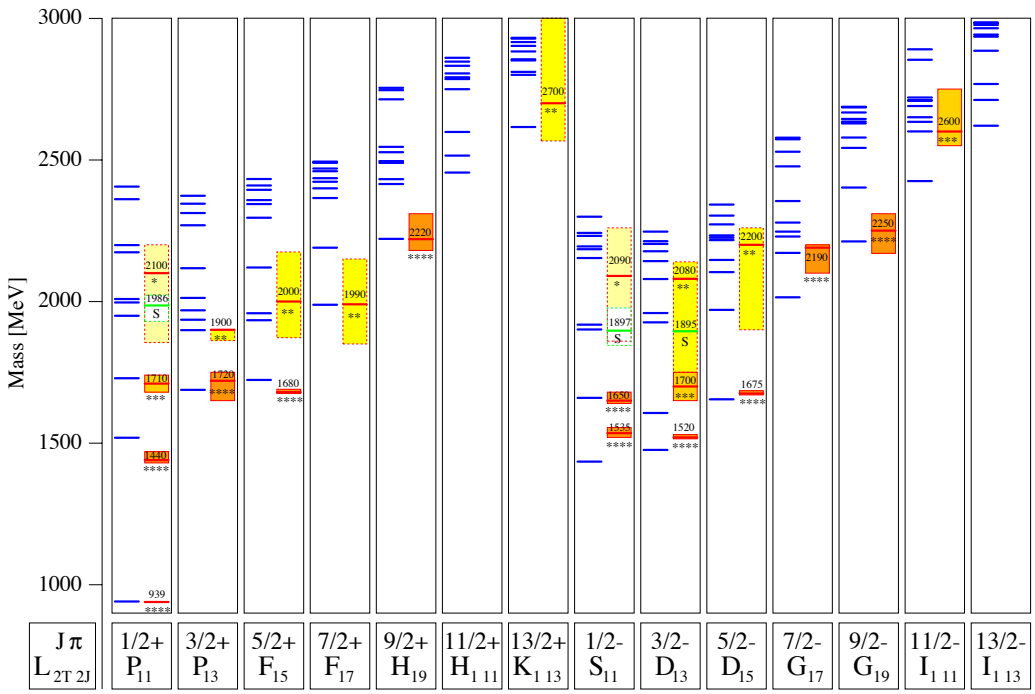

Jπ L 2T 2J	1/2+ P11	3/2+ P13	5/2+ F15	7/2+ F17	9/2+ H19	11/2+ H1 11	13/2+ K1 13	1/2- S11	3/2- D13	5/2- D15	7/2- G17	9/2- G19	11/2- I1 11	13/2- I1 13

Figure 1.3 Experimental N-resonance spectrum (right part of each column) and calculated spectrum (left part of each column) in a relativistic quark model [4]. The resonances are classified by the total spin J and parity π. The figure is from Ref. [4].

known "Missing Resonance" problem [5].

One difficulty in experiments is that these resonances are overlap each other, due to their broad widths. So far, most nucleon resonances have been established by elastic pion scattering experiments, e.g. [6]. However, states that decouple from $N\pi$ are suppressed [7]. This led scientists to study nucleon resonances in other reactions. The difficulty can be avoided by photo-production experiments with the potential to measure a richer baryon spectrum. Because of that, the experiments of photo-induced meson production off the nucleon is more researched recently and world wide.

A large amount of data on photo-production of many final-states were accumulated, and these data made a significant impact on the extracted properties of baryon resonances. A number of groups have undertaken couple-channel analyses of pion- and photo-induced channels and new resonances were found or determined to better

precision [1]. However, the work is still far away from the final success to completely explain the nature of baryon resonances.

The higher lying excited states decay not only through the single-meson emission to the ground state of the nucleon, but also through the intermediate excited states [8] with emission of double or multiple mesons. The multiple-stage decay induces the double- or triple- meson production reactions, which dominate the decay branching ratio at higher excitation energies. Figure 1.4 shows the total cross sections for various meson photoproduction channels in the photon energy range from 200 to 800 MeV.

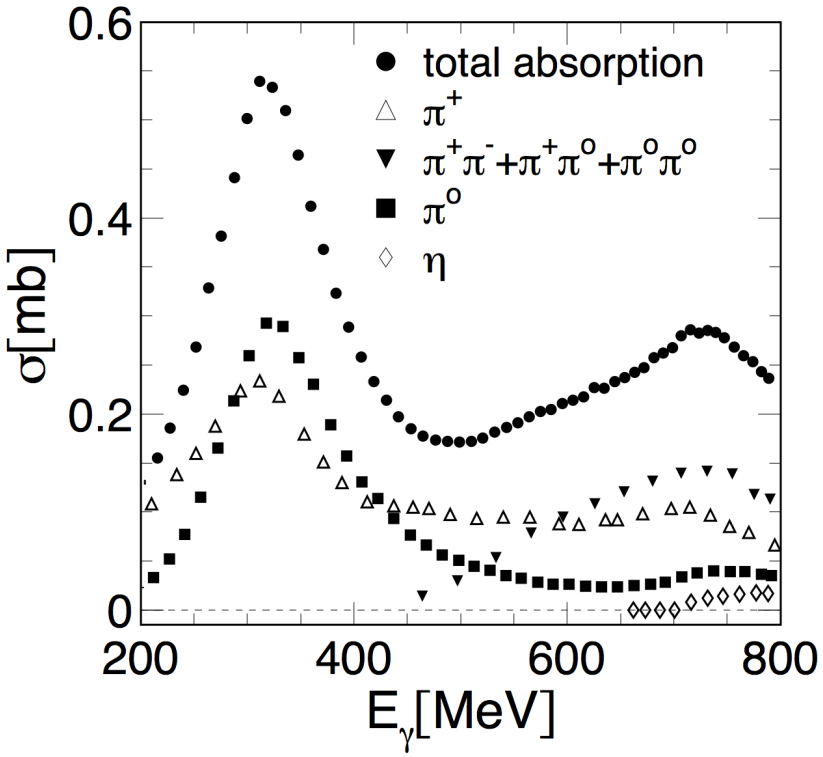

Figure 1.4 Total cross section for meson-photoproduction with contribution from individual channels. The figure is from Ref. [9].

In the second resonance region the situation becomes more complicated due to the presence of three strongly overlapping resonances, the $N(1440)1/2^+$, $N(1520)3/2^-$, and $N(1535)1/2^-$. Moreover, these resonances decay into various mesons, giving $N\pi$, $N\eta$, and $N\pi\pi$ final-states as represented in Fig. 1.4. In this region, the first challenge

is therefore to find methods to disentangle these resonances and understand their individual contributions. This has been done for single-pion photoproduction, in which partial-wave analyses have provided a good separation of the three resonances in this channel. The $N(1535)1/2^-$ resonance has a much larger branching ratio ($\approx$ 42%) into $N\eta$ than any other resonances. The η photoproduction reaction is therefore preferred by experimentalists and theorists to study this resonance. The large η-decay branching ratio is difficult to explain within the framework of quark models and has triggered many interrogations and many publications about the nature of the $N(1535)1/2^-$. Finally, our understanding of the second resonance region would not be completed without an accurate description of the double-pion channel, which contributes to more than half of the cross section in this energy region. Double-pion photoproduction will be extensively discussed in the following sections.

A series of models have been constructed to describe the baryon resonances. The first attempt was coming from the standard harmonic oscillator model, which is still a main tool trying to simplify the problem. One example is the quark shell model [10], which constructed a very simple multi-dimensional harmonic potential to confine the quarks. From this model, the resonance spectrum can be calculated and compared to the data. In a later stage, a series of QCD modified harmonic oscillator models were proposed to address the resonance spectrum. But the appearance of charm quantum number [11] made the things more complicated. The $SU(3)$ was extended to $SU(4)$ flavor symmetric group after the discovery of c quarks. The large mass of the additional quark broke the symmetry.

Continued research on both experimental and theoretical sides is needed to address the problem. On the theoretical side, the number of resonances relates to the effective degree of freedom of non-strange baryons [12]. The model of three equivalent valence quarks is a popular assumption. One of the alternatives is the quark-diquark clustering model [13, 14, 15], where a point like quark pair is considered as staying in

its 'frozen' ground state. If two of the three quarks are bound together, the number of effective degree of freedom is decreased and fewer resonances are predicted. The non-relativistic flux-tube model [16, 17] is the third option. More resonance states are predicted in this model through the inclusion of possible excitations of flux tubes as predicted by lattice QCD.

The mass spectrum of excited baryon states is also calculated from several quark models (QM). The non-relativistic QM from Isgur and Karl [18], for example, leads to a good qualitative understanding of the negative parity resonances by assuming a structure of three constituent quarks that are confined by a harmonic oscillator potential and interact through a residual one-gluon-exchange interaction. In order to describe the positive parity states, they had to introduce an additional anharmonicity into the confining oscillator potential that lowers the mass of the first positive parity resonance ($N^*(1440)$) [19]. The relativized QM for baryons [20] gave a good qualitative picture of the baryonic spectrum by using an interaction which can be decomposed into a color Coulomb part, a confining interaction, a hyperfine interaction, and a spin-orbit interaction between quarks. The confinement is provided by a Y-type string interaction between all three quarks. One (of several) difficulties with this model is that the low lying positive parity resonances are systematically overestimated by at least 100 MeV. A rather different interaction mechanism was used by Glozman and Riska [21]. In their model, two quarks interact via pion exchange. This flavor-dependent force is responsible for the low mass of the Roper resonance, $N^*(1440)$. Thus the two interaction mechanisms of the Glozman/Riska model and the Isgur/Karl/Capstick model are quite different and it is not clear whether the mass spectrum should be described by either one of these interactions or a mixture of both [22].

The photo- and electro-excitation of baryon resonances have been studied by several groups using different models. Li and Close [23] found the Q^2 dependence of

the $\gamma N \to N^*$ helicity amplitudes to be very sensitive to the structure of the Roper resonance. While the non-relativistic three-quark model, q^3, is not able to describe the Q^2 behavior, a hybrid quark-gluon model, q^3G, was initially in agreement with early experimental data. A similar conclusion was reached by Capstick [24], who found large disagreement in the photo-production amplitude of the Roper between a theoretical calculation in a non-relativistic q^3 model, including relativistic corrections and the experimental data. However, Capstick pointed out that relativistic effects are very important in these amplitudes. They were able to describe the helicity amplitudes using a relativized q^3 QM. Recent electroexcitation data of the Roper resonance from CLAS for Q^2 up to 4.5 GeV^2 provide strong evidence in favor of $N(1440)1/2^+$ as a first radial excitation of the q^3 ground state and the presentation of the Roper resonance as a q^3G hybrid state is ruled out [25].

On the experimental side, most of the published data so far focused on unpolarized cross-section and single-polarization observables, with the exclusive choice of either the polarized beam, target, or recoil nucleon. The single-polarization observables are more straightforward to access in both the experimental requirements and analysis method.

However, in order to determine the complete picture of the contributing amplitudes for the resonance production and decay mechanisms, the measurement of a set of well chosen single- and double-polarization observables are necessary. This thesis focuses on the extraction of a set of single- and double-polarization observables in a measurement with polarized beam and target. The reaction channel used is $\gamma p \to p\pi^+\pi^-$. The double-pion decay channel dominates in the higher energy region, which provides the possibility to investigate resonances higher than second resonance region. In further, the resonances decay through a series of complex decay chains, with the presence of N^*, ρ, and Δ. Measuring the decay chains is beneficial for the better understanding of the decay mechanism. It also provides various methodologies

for the data analysis. Another advantage of the double-pion channel is the multiple choice of kinematic variables. Unlike the single-pion reaction, where the cross section is only two-differential, the double-pion channel contains a complicated five-differential cross section. A large variety of kinematic variable choices are available to study the polarization observables under various conditions.

This thesis presents the first extraction of the beam-target double-polarization observables P_z^s and P_z^c. The photon energy range is from 0.6 to 2.4 GeV, covering the second resonance region and higher baryon resonances. Both of the observables are the z-components for the double-polarization observables $\vec{P}^s$ and $\vec{P}^c$; defined in Eq. (2.4) below. In the experimental setting, both the photon beam and target proton were polarized. The details of the experiment are illustrated in Chapter 3. By using various combinations of polarized yields from different polarization orientations, a set of asymmetries was constructed to isolate the observables for extraction. Due to limited statistics, the observables could not be extracted differentially in all five kinematic variables. The data were integrated over at least three out of five kinematic variables to gain enough statistics. The results are finally compared with model predictions [26]. More and deeper discussion of the analysis are stated in Chapters 4 and 5. The research on this topic helps not only to enhance the world database for single- and double-polarization observables. Together with the knowledge of other polarization observables based on the future analyses and experiments, a global picture of observables is promising to reveal the mystery of baryon resonances and decay mechanisms.

1.3 Models for the Double-Pion photoproduction

The total cross section of the $\gamma p \to \pi^+\pi^0 n$ and $\gamma p \to \pi^0\pi^0 p$ reactions have been obtained for the first time using the large acceptance detector DAPHNE [27] and high intensity tagged photon beams with energies from 400 to 800 MeV. The cross

section of the channel $\gamma p \to \pi^+\pi^- p$ has also been measured with good accuracy. In this energy region the $\Delta(1232)$ and $N(1520)3/2^-$ resonances dominate the production. DAPHNE-experiments have motivated several theorists to develop the model for the $\gamma N \to \pi\pi N$ reaction. The theoretical studies for the $\gamma p \to \pi^+\pi^- p$ reaction revealed that the double-pion photoproduction is dominated by the $\pi\Delta(1232)$ intermediate state, which arises from the Δ Kroll-Ruderman and Δ pion-pole term, shown in Fig. 1.5 (a) and (b), and the $N(1520)3/2^-$ excitation in Fig. 1.5 (c) [28]. The interference between the Δ Kroll-Ruderman and $N(1520)3/2^-$ excitation processes is essential to reproduce the energy dependence of the total cross section.

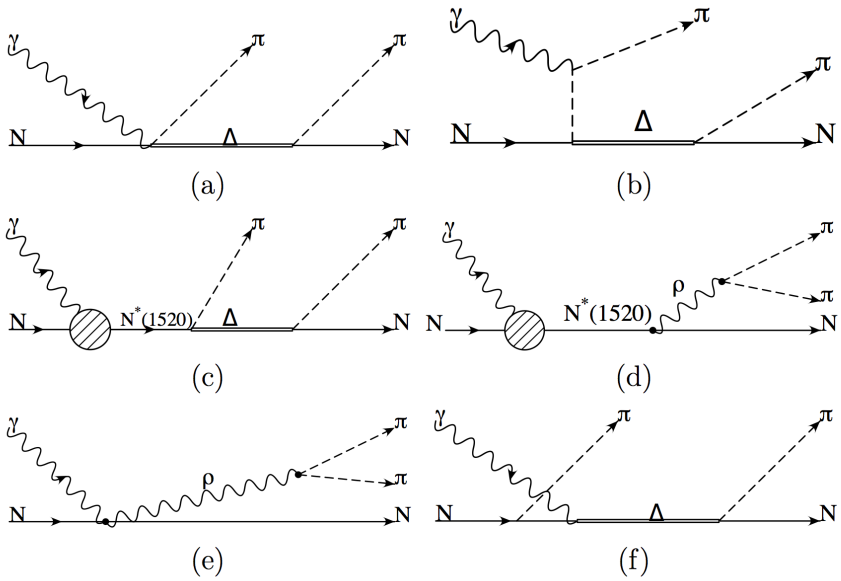

Figure 1.5 Diagrams for the double-pion production. (a) The Δ Kroll-Ruderman term, (b) the Δ pion-pole term, (c) the $N^* \to \pi\Delta$ contribution, (d) the $N^* \to \rho N$ contribution, (e) the ρ Kroll-Ruderman term. (f) The $\pi\Delta$ production accompanied by the nucleon exchange. The figure is taken from Ref. [28].

Other efforts from the theory side are being carried out to study the double-pion photoproduction. The Excited Baryon Analysis Center (EBAC) at Jefferson Lab [29] was established in 2006 with the goal of performing a dynamical coupled-channels analysis [30] of the world πN and γN scattering data in order to determine

meson-baryon partial-wave amplitudes and to extract N^* parameters. The developed dynamical coupled-channel (DCC) reaction model [31] is based on an energy-independent Hamiltonian formulation and satisfies the essential two- and three-body unitarity conditions. Since the bare N^* states are defined as the eigenstates of the Hamiltonian, in which the couplings to the meson-baryon continuum states are turned off, the extracted bare states can be related to the hadron states from constituent quark models and those from Dyson-Schwinger approaches. Within the EBAC model, the bare N^* states become resonance states through the coupled reaction processes. Thus, the model explicitly allows one to distinguish between the couplings of the bare N^* states and the meson-cloud (meson-baryon dressing) effects. A brief overview of EBAC results is given in [30]. First results from the DCC model were reported on the pion-induced reactions $\pi N \to \pi N$, $\pi N \to \eta N$, and $\pi N \to \pi\pi N$. The application of the model was also discussed for the analysis of π photoproduction as well as electroproduction, which contains the channels γN, πN, ηN and $\pi\pi N$. A simultaneous analysis of both single- and double-pion photoproduction is published. The authors note that the analysis of the single-pion production reactions alone is not enough to determine the amplitudes associated with the electromagnetic interactions. Both channels are required for the extraction of reliable information on N^* states below $W = 2$ GeV.

A. Fix has given a model prediction of the value of the observables by using the effective Lagrangian approach [26] for all the known decay processes. Figure 1.6 shows the cross section for the double-charged-pion process in the photon energy range from 0.3 to 1.5 GeV. The results are compared with the experimental data. The dash-dotted curve shows the contribution of the Δ Kroll-Ruderman term plus pion-pole term. The short dashed curve represents results including all resonance terms while the long dashed curve is for ρ_0 photoproduction via π_0 and σ-exchange. The solid curve shows the resulting cross section without $\Delta(1700)3/2^-$ and the dotted

one that for inclusion of $\Delta(1700)3/2^-$.

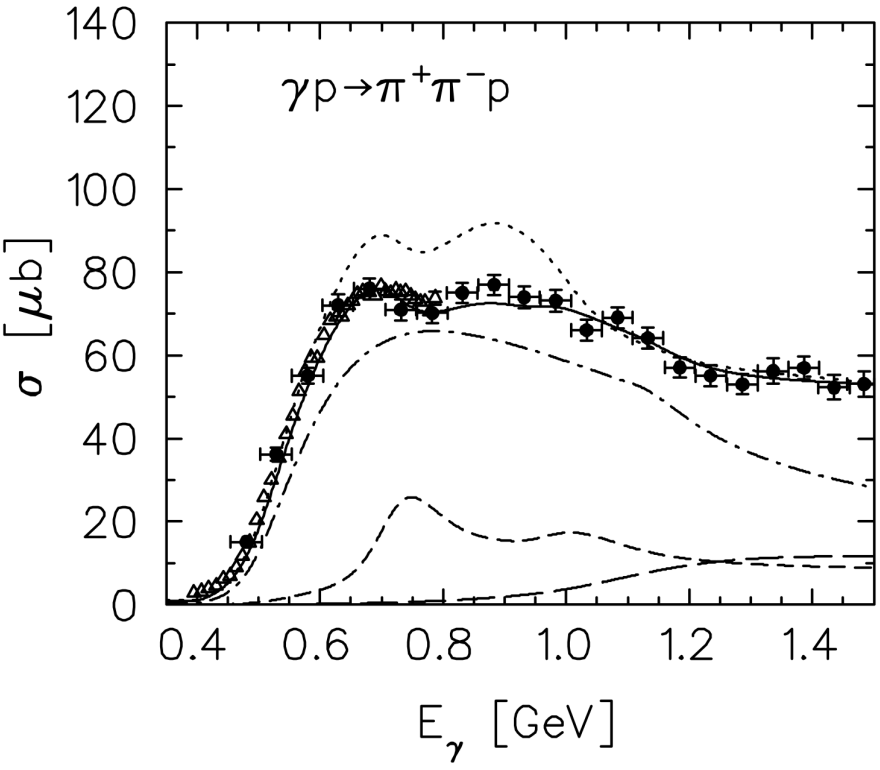

Figure 1.6 Total cross section for the double-charged-pion process in the photon energy range from 0.3 to 1.5 GeV. Model calculations [26] are compared with experimental data [32, 27]. Contributions of individual diagrams include the Δ Kroll-Ruderman term plus pion-pole term (dash-dotted); all resonance terms (short dashed); ρ_0 photoproduction via π^0 and σ-exchange (long dashed); and resulting cross section without (solid) and with the $\Delta(1700)3/2^-$ resonance (dotted). The figure is taken from Ref. [26].

Another effort is from the Bonn-Gatchina (BnGa) Group [33, 34, 35]. The cross sections for photo- and pion-induced production of baryon resonances and their partial decay widths to the two-body and multi-body final-states are also calculated in the framework of the operator expansion method. That approach is fully relativistic invariant, and allows to perform combined analyses of different reactions imposing directly the analysis and unitarity constraints. One method based on relativistic invariant operators, which are constructed directly from the four-vectors of the particles, was published. In an analysis of single- and double-pion photoproduction data,

the group showed that the observed resonance decay pattern is consistent with an interpretation of the Roper resonance as first radial excitation of the nucleon [36]. The BnGa group has also performed a systematic search for new baryon resonances in a multichannel partial-wave analysis [37]. The analysis of data included recent cross-section and polarization data from the double-pion photoproduction reaction. New resonances were found [37], including the $N(1880)1/2^+$, $N(1895)1/2^-$, $N(1875)3/2^-$, $N(2150)3/2^-$, and $N(2060)5/2^-$.

The analysis of a large number of single-meson photoproduction reactions performed in the framework of this method revealed a number of new baryon states.

1.4 Existing Measurements

Figure 1.7 shows recent total cross section data for $\gamma p \to \pi^0\pi^0 p$. The strong contribution of the $N(1520)3/2^-$ resonance to the $\gamma p \to \pi^0\pi^0 p$ reaction is seen as the first peak at $E_\gamma \approx 730$ MeV.

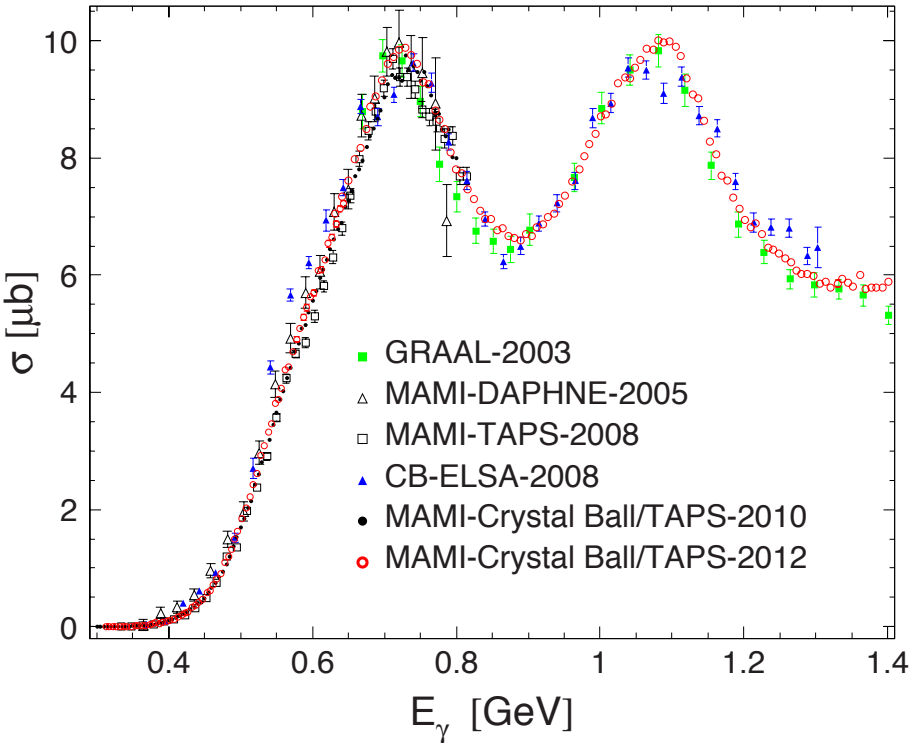

Figure 1.7 Total cross sections for $\gamma p \to \pi^0\pi^0 p$ are shown as a function of the incident-photon energy. The data are from GRAAL [38], CB-ELSA [39, 36], DAPHNE [40], TAPS [36], and Crystal Ball/TAPS [41, 42]. Figure adapted from Ref. [42].

However, total cross-section data alone are insufficient in the study of baryon resonances. Other observables, like polarization observables, are needed to constrain the models and partial-wave analyses. A series of exciting experiments has been carried out; in particular at the CLAS facility at JLab, the Crystal Barrel/TAPS experiment at ELSA, and the Crystal Ball/TAPS experiment at MAMI facility to measure the differential cross section, single- and double-polarization observables by using polarized (linear or circular) photon beams and polarized targets for the single- and double-meson photoproduction reactions.

Nucleon resonance excitations contribute to the total photoproduction cross sec-

tion. In the second resonance region the $N(1440)1/2^+$, $N(1520)3/2^-$, and $N(1535)1/2^-$ resonances dominate the cross section of the $\gamma p \to p\pi^+\pi^-$ reaction. When the ground-state nucleon is excited to the second resonance region, within a very short time, resonances decay back into the ground-state nucleon through various decay modes. An important decay channel is $N^* \to \Delta\pi$, following the emission of the second π meson during the decay of Δ. Another important channel is $N^* \to p\rho$. The vector meson ρ^0 has branch ratio of 99% to decay into $\pi^+\pi^-$. Figure 1.8 illustrates the different decay modes from N^*.

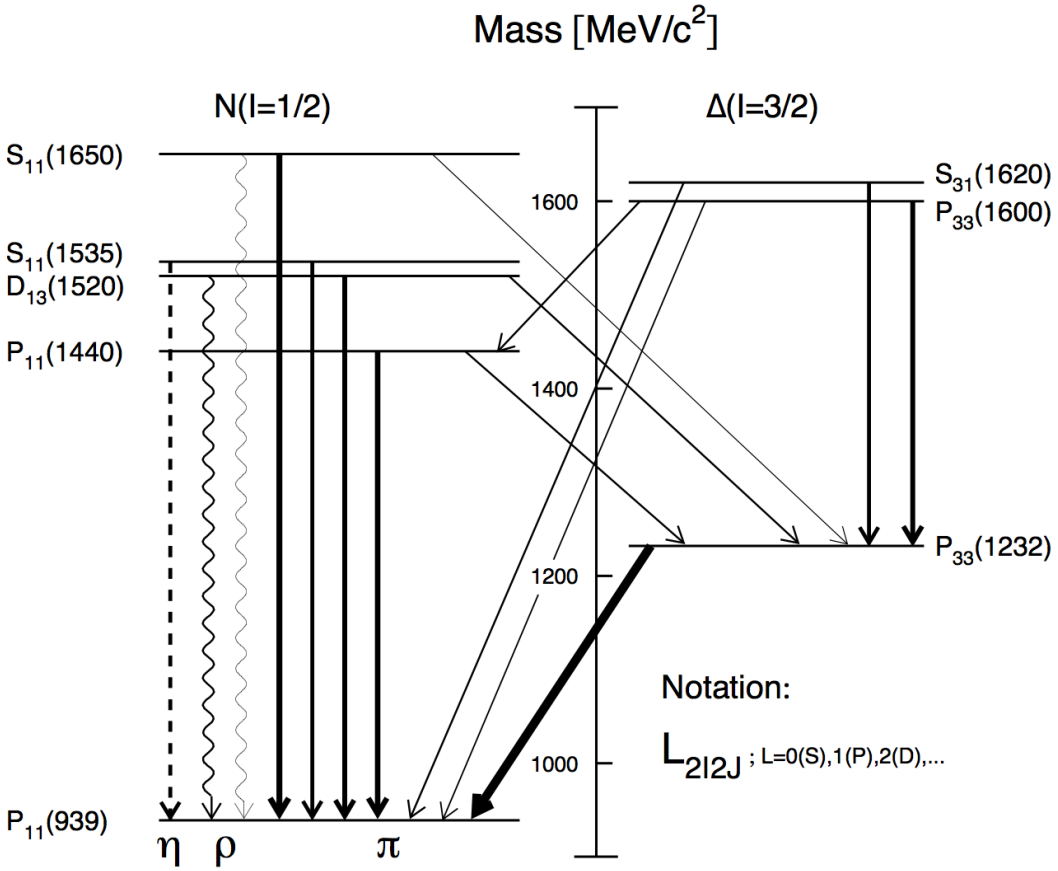

Figure 1.8 Nucleon excitation spectrum. The arrows are showing the mesonic decays of these resonances, the associated width is proportional to the respective branching ratio. Figure taken from Ref. [9].

In addition to the total cross-section, measurements of the invariant mass spectra of the $\gamma p \rightarrow p\pi^+\pi^-$ reaction were performed at Mainz [43]. These experimental results provide additional constraints for theoretical models.

Although it is widely agreed that the polarization observables are important, as they effectively constrain model predictions, experimental measurements were sparse because of the required polarized beams or targets or the need to measure nucleon recoil polarizations. The development of the technologies to polarize both beam and target opened the world to extract these observables. The first measurement of the beam helicity asymmetry in the $\gamma p \rightarrow p\pi^+\pi^-$ reaction was performed by CLAS collaboration [44]. Figure 1.9 shows the helicity asymmetry for nine different invariant mass bins.

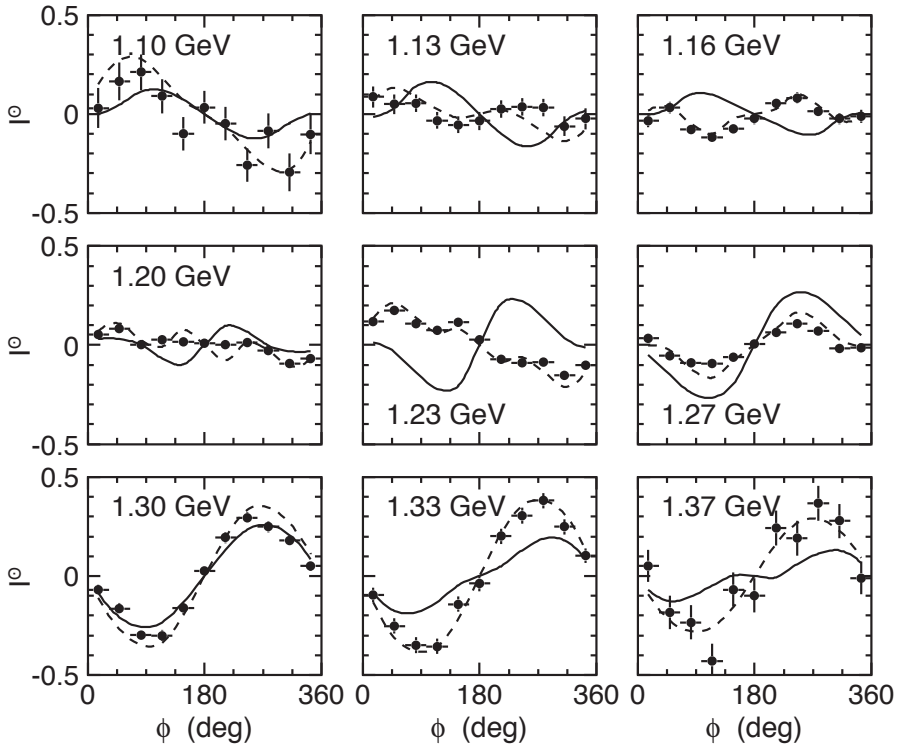

Figure 1.9 Helicity asymmetries at $W = 1.50$ GeV for nine bins of the invariant mass $M(p\pi^+)$, as indicated [44]. The solid curves are the results of Mokeev et al. [45, 46, 47]. The dashed curves show results of calculations by Fix and Arenhövel [26]. Figure from Ref. [44].

The asymmetry is an odd function of the azimuthal angle. The solid curves are the predictions by Mokeev [45, 46, 47] and dashed curves are the calculation by Fix and Arenhövel [26]. Since the cross section of double-pion photo-production is five dimensional, the binning in all of them is for statistical reasons impossible. Thus integrated asymmetries are shown to investigate more aspects of the helicity asymmetry. In Fig. 1.10 [44], the azimuthal angle was fixed to 105° allowing the study of helicity asymmetries for various invariant masses. The open triangles show the asymmetries at $W = 1.95$ GeV and the filled circles are at $W = 1.55$ GeV.

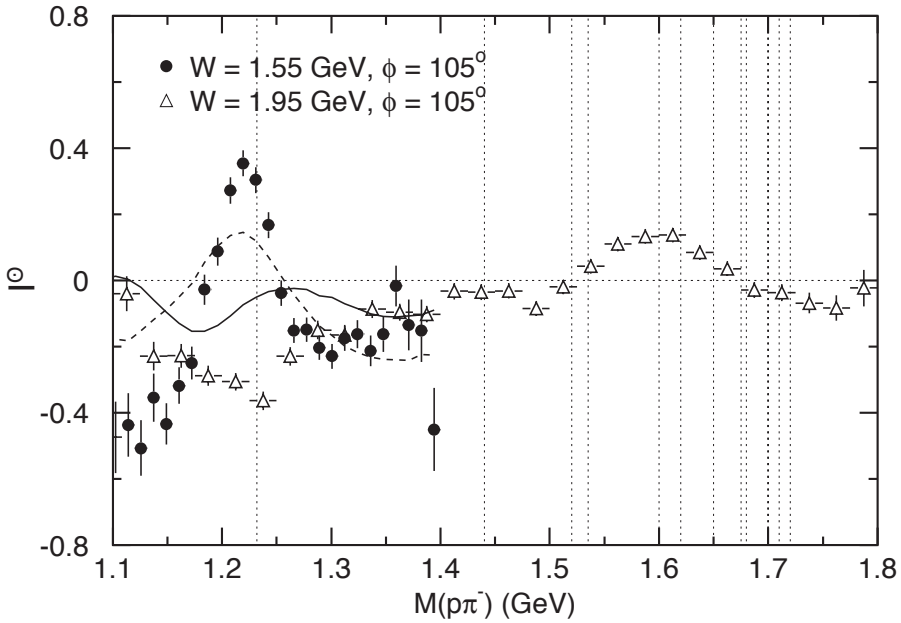

Figure 1.10 Helicity asymmetry as a function of the invariant mass $M(p\pi^-)$ for $W = 1.55$ GeV (filled circles) and 1.95 GeV (open triangles) and a 30°-wide ϕ-angle range centered at $\phi = 105°$. The curves are the results of Mokeev et al. [45, 46, 47] (solid) and Fix and Arenhövel [26] (dashed) for $W = 1.55$ GeV only.

Other measurements of the beam-helicity asymmetry were carried out at the MAMI accelerator in Mainz for three isospin channels, $\gamma p \to p\pi^+\pi^-$, $\gamma p \to n\pi^+\pi^0$ and $\gamma p \to p\pi^0\pi^0$ [48, 49, 50]. The circularly polarized photons were produced by bremsstrahlung of longitudinally polarized electrons. The photons were incident on an unpolarized proton target. The charged pions and the decay photons of π^0 mesons

were detected in an electromagnetic calorimeter with 4π coverage. Figure 1.11 shows an example of the beam helicity asymmetries for photon energies from 575 to 815 MeV for the $\vec{\gamma}p \to p\pi^+\pi^-$ channel [48]. Model predictions from Fix and Arenhövel [26] and Roca [51] are plotted for comparison. Due to the symmetric behavior of the observable I°, the extracted observables were fit by a sine-series, shown as green curves. The results of the measurements of the three double-pion channels will help in the future to investigate the properties of resonances as they challenge and constrain present models.

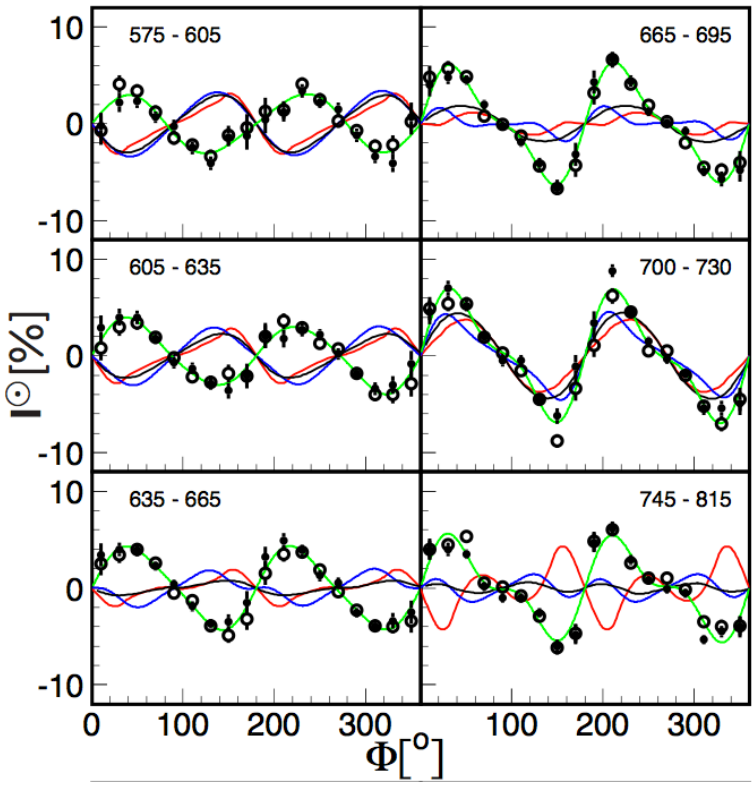

Figure 1.11 Beam-helicity asymmetry in the $\gamma p \to p\pi^+\pi^-$ channel for different bins of photon energy. Green curves: sine-series fit to the data. Red curves: Fix and Arenhövel model [26]. Blue: Roca [51], Black: Roca [51] for 4π acceptance. Figure taken from Ref. [48]

Chapter 2

Double-Charged-Pion Photoproduction

2.1 Kinematic Variables of Double-Charged-Pion Photoproduction

Before discussing the experimental facilities and data analysis, it is necessary to introduce the kinematic variables used in this thesis to describe the $\gamma p \to p\pi^+\pi^-$ reaction. There are two incoming particles and three final-state particles participating the reaction. The momentum vectors of these particles are used to define two reaction planes, called the scattering plane and the double-pion plane. The scattering plane is defined in the center-of-mass (CM) frame by the incoming photon beam and recoiling proton, while the double-pion plane is defined by the two π mesons. With the momenta of the incident photon, $\vec{k}$, and final-state paricles, $\vec{p}_p$, $\vec{p}_{\pi^+}$, and $\vec{p}_{\pi^-}$, the axes of the coordinate system in the scattering plane are

$$\hat{z} = \hat{k}, \qquad \hat{y} = \frac{\hat{k} \times (\vec{p}_{\pi^+} + \vec{p}_{\pi^-})}{|\hat{k} \times (\vec{p}_{\pi^+} + \vec{p}_{\pi^-})|}, \qquad \hat{z} = \hat{x} \times \hat{y}, \tag{2.1}$$

and in the double-pion plane[1]

$$\hat{z}' = \frac{\vec{p}_{\pi^+} + \vec{p}_{\pi^-}}{|\vec{p}_{\pi^+} + \vec{p}_{\pi^-}|}, \qquad \hat{y} = \hat{y}', \qquad \hat{z}' = \hat{x}' \times \hat{y}', \tag{2.2}$$

The two different reaction planes are shown in Fig. 2.1.

The angle Φ_{CM} is defined as the angle between scattering plane and double π plane. It is of special interest since it will be used as the main kinematic binning variable. Polar angle θ is the angle between π^+ vector and the opposite vector of recoiling proton, while angle θ_{CM} is that between incoming photon beam and recoiling

[1]The $\hat{z}'$ axis in this work is equal to $-\hat{z}'$ in Ref. [52].

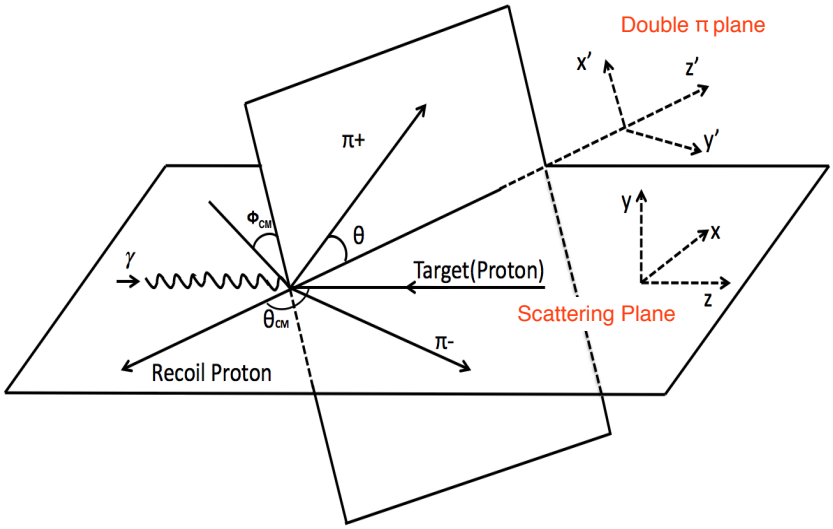

Figure 2.1 Reaction planes in center of mass frame. Photon beam and recoiling proton determine the scattering reaction plane and two π mesons determine the second reaction plane. The three kinematic angles and coordinate system are shown.

proton. The angle β in Eq. (2.5) is defined as the angle between the scattering plane and beam polarization direction.

2.2 Formalism of Polarization Observables P_z, P_z^s and P_z^c

The derivation of the polarization observables has been completed by W. Roberts [52] for the processes $\gamma N \to N\pi\pi$ and $\pi N \to N\pi\pi$. Roberts has developed a set of polarization observables that are accessible to final-states containing two pseudo-scalar mesons and a spin-1/2 baryon, such as $N\pi\pi$. He has already examined the observables that may arise using photon beams. The derivation is written for these observables in terms of both helicity and transversity amplitudes. The relationships among them are derived and expressed as the listed inequalities. He also indicates the measurements needed for each of the observables. A number of the observables can be measured in the near future based on the existing facilities, particular for

the double-pion process. Indeed, the photon polarization asymmetry $I^{\odot}$, has already been measured at Jefferson Laboratory for double-charged-pion process [53]. The new technology brought up the polarized targets which elicited the measurement of observables P_x, P_y and P_z. Coupling with circularly polarized beams allows the measurement of $P_x^{\odot}$, $P_y^{\odot}$ and $P_z^{\odot}$, while the linearly polarized photons help open the door to access $P_x^{s,c}$, $P_y^{s,c}$ and $P_z^{s,c}$. The experiments and analysis relating to the observables mentioned above will draw attention in the future.

The differential cross section is proportional to the amplitude $\mathcal{M}$ for the transition, $d\sigma \propto \overline{|\mathcal{M}|^2}$. The matrix elements $\mathcal{M}$ can be written as

$$i\mathcal{M} = \chi^{\dagger}(\mathcal{A}_j + \sigma_i \mathcal{B}_{ij})\phi\epsilon_j, \tag{2.3}$$

where the χ and ϕ are respectively the Pauli spinors representing the final and initial nucleons and $\vec{\epsilon}$ is the polarization vector of the initial photon. The vector $\mathcal{A}$ and the pseudotensor $\mathcal{B}$ are the quantities that contain all the details of the model used to describe the particular reaction which is being studied. Eight helicity amplitudes determine the reaction, $\mathcal{M}_1^{\lambda}$, $\mathcal{M}_2^{\lambda}$, $\mathcal{M}_3^{\lambda}$, $\mathcal{M}_4^{\lambda}$, where $\lambda = \pm$ is the helicity of the photon.

The polarized reaction rate for the double-pion photoproduction reaction, I, can be expressed in terms of polarization observables [52],

$$\begin{aligned}
\rho_f I =& I_0 \Big\{ (1 + \vec{\Lambda}\cdot\vec{P} + \vec{\sigma}\vec{P}' + \Lambda_i^{\alpha}\sigma^{\beta'} O_{\alpha\beta'}) \\
&+ \delta_{\odot}(I^{\odot} + \vec{\Lambda}\cdot\vec{P}^{\odot} + \vec{\sigma}\vec{P}^{\odot\prime} + \Lambda_i^{\alpha}\sigma^{\beta'} O^{\odot}_{\alpha\beta'}) \\
&+ \delta_l[\sin 2\beta(I^s + \vec{\Lambda}\cdot\vec{P}^s + \vec{\sigma}\vec{P}^{s\prime} + \Lambda_i^{\alpha}\sigma^{\beta'} O^{s}_{\alpha\beta'}) \\
&+ \cos 2\beta(I^c + \vec{\Lambda}\cdot\vec{P}^c + \vec{\sigma}\vec{P}^{c\prime} + \Lambda_i^{\alpha}\sigma^{\beta'} O^{c}_{\alpha\beta'})] \Big\}
\end{aligned} \tag{2.4}$$

while $\rho_f = \frac{1}{2}(1 + \vec{\sigma}\cdot\vec{P}')$ is the density matrix of the recoiling nucleon. The polarization observables are $\vec{P}$, that arise if the target nucleon is polarized, the nucleon recoil polarizations $\vec{P}'$, and the target/recoil polarizations $O_{\alpha\beta'}$. Observables with a

superscript s or c enter the reaction rate in the $\sin 2\beta$ and $\cos 2\beta$ terms, respectively. The photon beam can be polarized circularly or linearly with degrees of polarization of $\delta_\odot$ or δ_l, respectively. The degree of polarization of the initial-state nucleon target is $\vec{\Lambda}_i$.

In this thesis, the beam is only polarized linearly, $\delta_\odot = 0$, and the target is polarized longitudinally, $\Lambda_{i,x} = \Lambda_{i,y} = 0$. The polarized reaction rate then simplifies to:

$$\rho_f I = I_0 \left\{1 + \Lambda_z P_z + \delta_l \left[\sin 2\beta (I^s + \Lambda_z P_z^s) + \cos 2\beta (I^c + \Lambda_z P_z^c)\right]\right\}, \qquad (2.5)$$

where Λ_z stands for the target polarization along the direction of the incoming photon beam. In total five polarization observables are determining the reaction rate in Eq. (2.5); the observables P_z, P_z^s and P_z^c, which are the observables to be determined in this thesis, and the observables I^s and I^c, which were studied by Hanretty in the CLAS experiment g8 at JLab [54] and Sokhoyan in a CBELSA/TAPS experiment at ELSA [55].

Each polarization observable can be expressed in terms of a specific combination of helicity amplitudes. Due to various combinations, there are many different observables. Table 2.1 gives the unpolarized reaction rate, I_0 and the three polarization observables to be extracted in this thesis, P_z, P_z^s and P_z^c, in terms of the helicity amplitudes.

Table 2.1 Singe- and double-polarization observables P_z, P_z^s and P_z^c and their expressions in terms of helicity amplitudes.

Observable	Helicity Form
I_0	$\lvert M_1^-\rvert^2 + \lvert M_1^+\rvert^2 + \lvert M_2^-\rvert^2 + \lvert M_2^+\rvert^2 + \lvert M_3^-\rvert^2 + \lvert M_3^+\rvert^2 + \lvert M_4^-\rvert^2 + \lvert M_4^+\rvert^2$
$I_0 P_z$	$-\lvert M_1^-\rvert^2 - \lvert M_1^+\rvert^2 - \lvert M_2^-\rvert^2 - \lvert M_2^+\rvert^2 + \lvert M_3^-\rvert^2 + \lvert M_3^+\rvert^2 + \lvert M_4^-\rvert^2 + \lvert M_4^+\rvert^2$
$I_0 P_z^s$	$2\Im(M_1^+ M_1^{-*} + M_2^+ M_2^{-*} - M_3^+ M_3^{-*} + M_4^+ M_4^{-*})$
$I_0 P_z^c$	$2\Re(M_1^+ M_1^{-*} + M_2^+ M_2^{-*} - M_3^+ M_3^{-*} - M_4^+ M_4^{-*})$

These combinations of helicity amplitudes show that polarization observables can

be sensitive to the interference of helicity amplitudes and to their relative phases, the unpolarized cross section is not.

2.3 Model from A.Fix

Results from this work will be compared to model calculations by A. Fix ad H. Arenhövel [26]. In that paper, A. Fix has extended the elementary two-pion photoproduction operators to higher energies, and includes all four-star resonances with center-of-mass energy less than 1.8 GeV. This operator is based on the effective Lagrangian approach evaluating only the tree leveled diagrams, which is shown in Fig. 2.2 [26]. The necessary coupling strengths are determined by the hadronic and the electromagnetic decays of the resonances. The present approach is not allowing a high-precision description of the processes, mainly because of the non-relativistic treatment of the baryons. However, it should be able to account for the main feature of the reaction so that the qualitative conclusions about the underlying mechanisms can be derived. In the double-charged-pion channels, it a decent description of the cross-section data can be obtained, but only if the large contribution of the $\Delta(1700)3/2^-$ is excluded.

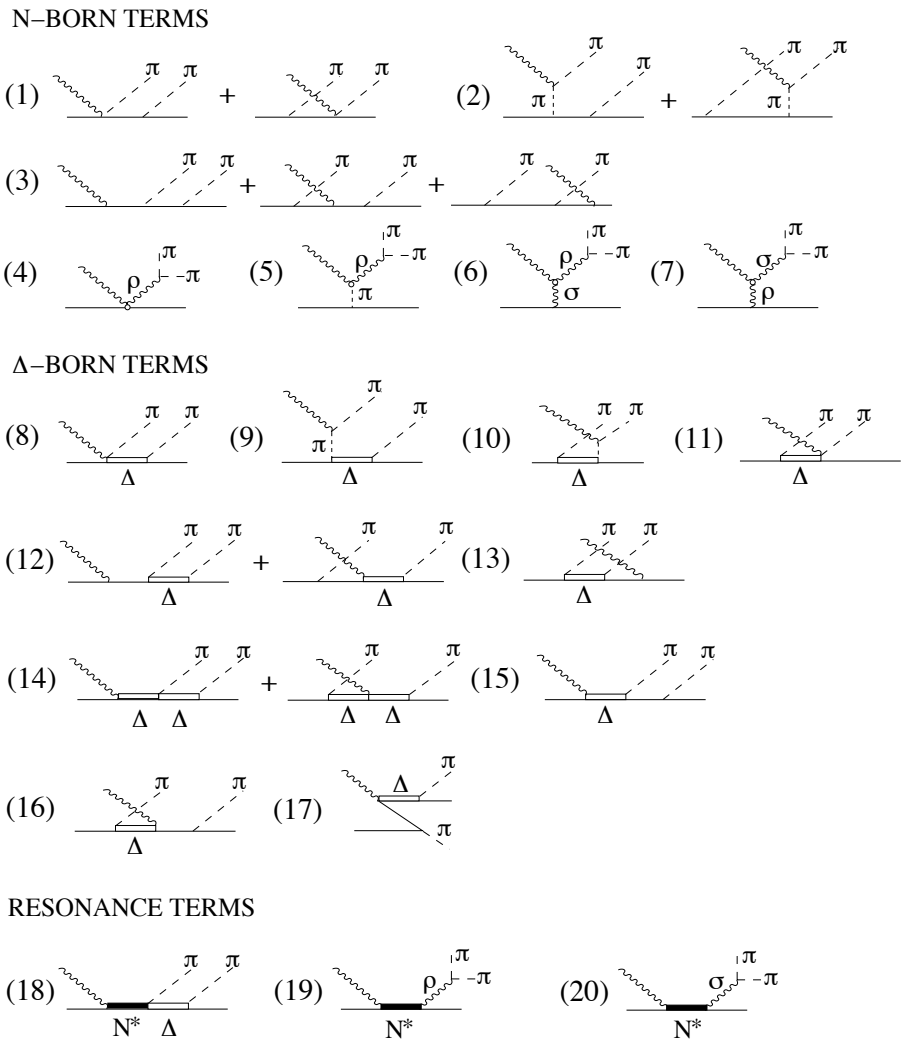

Figure 2.2 Diagrams for the reaction $\gamma N \to \pi\pi N$ used in the model by Fix and Arenhövel. The figure is taken from Ref. [26]

Chapter 3

Experimental facility

The work presented in this thesis utilized data from run g9a of Jefferson Lab experiment E06-013, "Measurement of $\pi^+\pi^-$ Photoproduction in Double-Polarization Experiments using CLAS" [56]. The data were taken with the CEBAF Large Acceptance Spectrometer (CLAS), which is housed in Hall B. A linearly-polarized photon beam was produced by coherent bremsstrahlung of the primary electrons on a crystal radiator. The photons were then incident on a stationary polarized proton target. The outgoing charged particles were detected by the CLAS. The reaction was then reconstructed using four-momentum vector conservation.

3.1 Overview of experiment g9a

The g9 experiment consists of two parts, g9a (target was longitudinally polarized) and g9b (target was transversely polarized). In both, g9a and g9b, data were collected with circularly- and linearly-polarized photon beams. The analysis presented here makes use of data taken with linearly-polarized photons in g9a, which took place from December 7, 2007 to February 2, 2008. Based on the nominal electron-beam energy, g9a can be divided into three different periods. Table 3.1 shows the time and the run ranges for each period.

In order to reduce the systematic uncertainties of the extracted polarization observables, data were taken with both, positive and negative target helicity and two different orientations of the photon-beam polarization. The photon polarization was either parallel or perpendicular to the Hall-B floor. The extraction of polarization

Table 3.1 Nominal electron-beam energies and corresponding data-taking periods and run ranges for the sample of g9a data used in this work.

Electron Beam Energy (GeV)	Dates (M/D/Y)	Run Range
3.539	12/07/07 - 12/20/07	55678 - 55844
2.751	01/05/08 - 01/11/08	55854 - 55938
4.599	01/17/08 - 02/03/08	55945 - 56152

observables makes use of an asymmetry between yields obtained with all possible combinations of beam polarization direction and target helicity. To give an idea about the amount of data collected for a given beam-target polarization combination, in Table 3.2 we show the total triggers collected for different energies of the coherent peak. In the table, and further in the text, we denote the beam and the target polarizations with δ and Λ, respectively. The superscripts $\parallel$ and $\perp$ denote the polarization orientations of the photon beam relative to the Hall-B floor. The superscripts $+$ and $-$ denote the polarization orientation of the target. One can see that data were collected for nine coherent peak positions, ranging from 0.73 GeV to 2.3 GeV, in steps of 0.2 GeV. During the g9a running period, data were also taken with amorphous radiator. Since the photon beam for these data was circularly polarized, they are not considered in this analysis.

In g9a, a single-sector level-2 trigger was used. The sector trigger was a coincidence between the time-of-flight and the start counters. The PMT signals of all TOF paddles in each sector were grouped in a logical OR. Similarly, the PMT signals of all ST paddle in each sector were grouped in a logical OR. For each sector, the TOF and the ST OR signals were grouped in a logical AND. When there was an AND signal in at least one sector, the signal was sent to the trigger supervisor and used to generate the gate signals for the ADCs and the start/stop signals for the TDCs. Since the distance from the target to the TOF counter is several meters, the range

Table 3.2 Total number of triggers (in millions) collected in g9a for various photon energies and different combinations of beam and target polarization directions.

Nominal Coherent Edge (GeV)	$\delta^{\parallel}\Lambda^{+}$	$\delta^{\perp}\Lambda^{+}$	$\delta^{\parallel}\Lambda^{-}$	$\delta^{\perp}\Lambda^{-}$
0.73	11.0	10.6	3.8	3.7
0.93	10.3	10.2	12.3	12.7
1.10	9.3	27.5	5.2	6.6
1.30	14.7	14.4	17.8	17.0
1.50	14.6	18.5	17.7	19.1
1.70	8.8	5.3	37.6	38.1
1.90	8.6	8.4	15.9	12.5
2.10	24.0	22.4	17.7	15.0
2.30	28.2	21.1	82.7	12.3

of particles times of flight to that detector is larger than to the start counter. Thus, the TOF sector OR signal was 120-ns long, while the ST sector OR signal was 25-ns long. The latter was delayed relative to the former, so that effectively it was the start counter detector that set the time of the trigger signal. All the times measured by the TDCs were relative to the trigger time. Level-2 trigger means that in addition to the TOF-ST sector coincidence, the hits in the drift chambers had to match patterns of likely tracks. The Level-2 trigger rejects events, such as due to cosmic rays, that do not originate in the target.

3.2 Continuous Electron Beam Accelerator Facility (CEBAF)

The Continuous Electron Beam Accelerator Facility (CEBAF) [57] in Newport News, VA, was built to provide high-duty electron beams for nuclear-physics experiments. It began operations in 1996.

The electrons are produced in the injector via photoelectric effect by shining laser light on a GaAs photocathode. The latter can provide polarizations of up to 80%. The

electron beam is accelerated to 67 MeV by a set of cryomodules. This pre-accelerated beam is injected into the main machine, which consists of two superconducting linear accelerators (linacs) and eight arcs that transport the beam between the two linacs. Each linac consists of 20 cryomodules, each of which is composed of 8 Niobium superconducting cavities. After leaving the injector, the electrons enter the north linac and then the first arc, where by the use of magnets they are transported to the south linac. Another arc bends the beam back to the north linac, and so on. Thus, the electrons can re-circulate through the accelerator up to 5 times (passes). At the time the experiment discussed here was conducted, each linac could accelerate the electrons to energies of up to 580 MeV, which means up to 1.16 GeV per pass and up to 6 GeV overall. From CEBAF the electron beam is extracted to three end stations (experimental halls), Halls A, B, and C. As the laser system in the injector actually consists of three 499-MHz (one third of the 1497-MHz frequency at which the linacs operate) diode lasers (each of which provides beam to one end station), the beam bunches arrive in Hall B every 2.004 ns. This system allows for a simultaneous beam delivery to the three halls, which is a unique feature of CEBAF. Figure 3.1 shows schematic overview of the accelerator and the three experimental halls. Full details of the accelerator can be found in Ref. [57].

At the time of writing this document, a 12-GeV upgrade of the accelerator has been in progress. The detectors in the existing halls are also being upgraded and a new Hall D has been built.

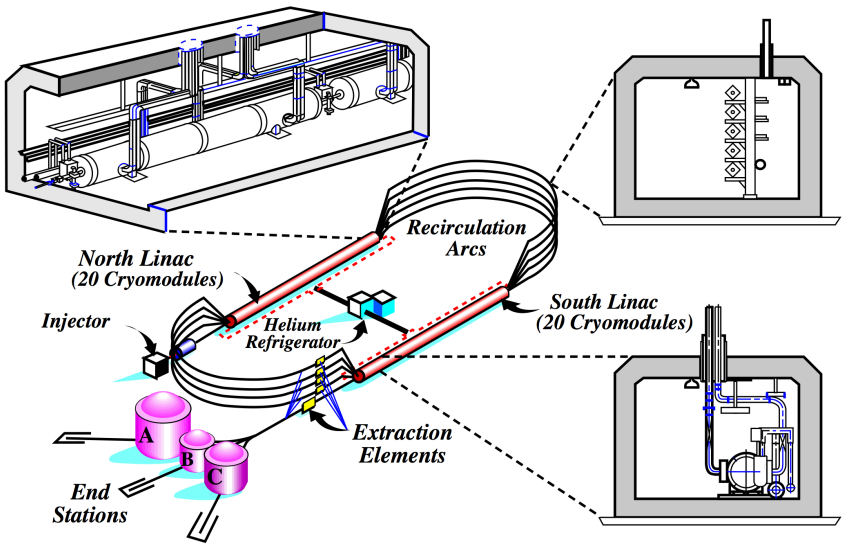

Figure 3.1 Schematic diagram of the CEBAF accelerator and the three experimental halls. One can see the two linacs and the bending arcs that transport the beam between the linacs. The figure is from Ref. [57].

Linearly-polarized photon beam

The linearly polarized photon beam for this experiment was produced by using the coherent bremsstrahlung technique [58]. The electrons extracted from the CEBAF accelerator were incident on a 50-μm thick diamond radiator. The latter is mounted on a goniometer, which allows the crystal to be moved vertically and horizontally, as well as to be rotated about three independent axes. The goniometer, thus, makes it possible to control the orientation of the crystal with respect to the electron beam, and therefore, to adjust the energy of the coherent bremsstrahlung. In order to enhance the intensity of the coherent radiation component over the incoherent component (and therefore the size of linear polarization in the coherent peak), the photon beam passes through a 2-mm-diameter collimator located approximately 23 m downstream from the diamond radiator. Tight collimation also provides for better separation of the main coherent peak from adjacent coherent peaks. With this technique, polarizations of up to approximately 80% have been achieved in CLAS experiments.

Since coherent radiation is produced when the momentum transfer from an electron to the crystal is equal to a reciprocal lattice vector, the spectrum of linearly-polarized photons is discrete. Typically, for a given orientation of the diamond with respect to the electron beam, a specific reciprocal-lattice vector is selected such that coherent bremsstrahlung is enhanced for the corresponding momentum transfer, which results in a peak (coherent peak) in the photon energy spectrum. Since one cannot orient the crystal in a way that selects only one reciprocal lattice vector, other coherent peaks are also observed in the spectrum, but with much smaller intensity and polarizations. This is shown in Figure 3.2 where one can see a typical linearly-polarized photon spectrum from a diamond radiator [59]. In Hall B the main coherent peak is obtained by selecting the $[02\bar{2}]$ crystal plane [60]. Incoherent bremsstrahlung

is also emitted, and the experimental photon energy spectrum contains incoherent component as well (even though tight collimation reduces its amount). In the experiment, the energy (position) of the main coherent peak is set to a desired nominal value by adjusting the polar angle of the crystal in lab system, while the orientation of the photon polarization is set by changing the azimuthal angle [59]. Once the orientation of the crystal was fixed, data were taken. During a data run (spanning usually over two hours) the set experimental conditions were not changed. The magnitude of the linear polarization is obtained by fitting theoretically calculated curves to the experimental energy spectrum of the collimated photon beam [61, 62].

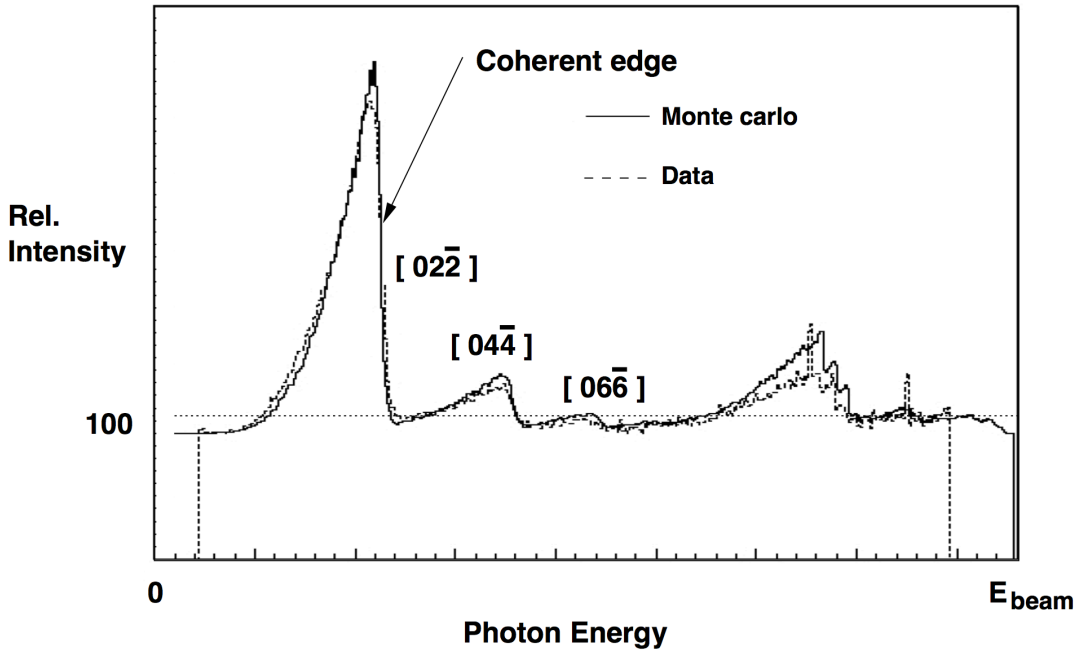

Figure 3.2 Typical energy distribution of coherent bremsstrahlung. The spectrum is normalized to a reference distribution obtained from amorphous radiatior. One can see the largest beam intensity when selecting the [02$\bar{2}$] plane. The intensity of the linearly polarized photon beam decreases gradually with the higher and higher order planes.

Tagging spectrometer

The tagging spectrometer (tagger) in Hall B [63] consists of a dipole magnet and two planes of scintillators (hodoscope) operating in the focal plane of the magnet. Figure 3.3 shows the components of the tagger. Electrons that do not emit

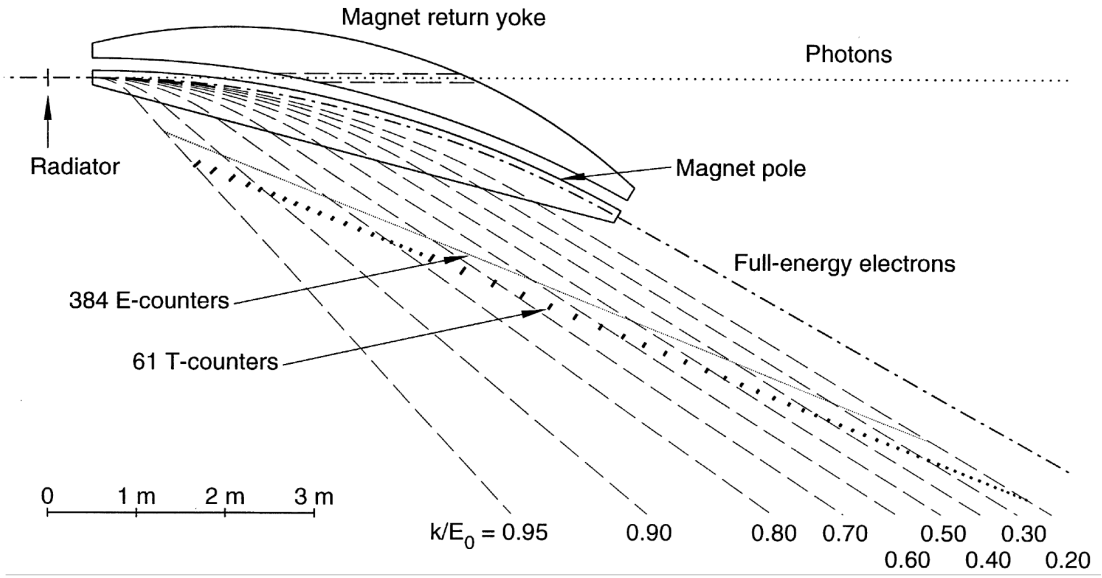

Figure 3.3 Schematic diagram of the Hall-B bremsstrahlung tagging system. The trajectories in the dipole field of beam-electrons with nominal energy, E_0, as well as of electrons that have radiated bremsstrahlung in the radiator can be seen. Two planes of focal-plane detectors, E-counters (solid gray line) and T-counter (solid dashes) allow for determining the energy and the time of the electron hit, respectively. The trajectory of the photon beam is shown by the dotted line. The figure is from Ref. [63].

bremsstrahlung in the radiator, are bent by the magnetic field along the optical axis of the magnet and directed to the beam dump. Electrons that have radiated photons, and have lost energy, are directed to the focal-plane hodoscope. The position of an electron hit (and therefore its energy) is measured by 384 partially overlapping scintillator paddles (E-counters) and is used to reconstruct the energy of the electron. This geometry yields effectively 767 energy bins and improves the resolution of the energy measurement. Behind the plane of the E-counters is located the T-plane

consisting of 61 partially overlapping scintillators, which yields effectively 121 timing bins. The T-counters are used to determine the time of an electron hit. The energy and the time of an electron hit are used to determine the energy and the time of the corresponding bremsstrahlung photon at the target.

The spectrometer allows tagging photons with energies between 20% and 95% of the energy, E_0, of the electron beam. The energy resolution is $0.001 \times E_0$ and the timing resolution is 110 ps. The latter is sufficiently low to resolve the 2.004-ns time structure of the electron beam, which is used to reduce accidental background.

Determination of the beam polarization

In order to extract polarization observables from data, the degree of linear photon polarization must be known. Observables are typically extracted over a photon-energy bin of a finite width. Since in g9a data were taken at discrete nominal coherent-edge positions that were 0.2 GeV apart, one energy bin in our analysis includes only data taken at one nominal coherent-edge position. For example the data in the bin $E_\gamma = 0.8 \pm 0.05$ GeV were all taken when the coherent edge was set to 0.93 GeV. Although all the events in one data run share only one nominal coherent edge, due to oscillations in the crystal, the actual position of the coherent edge fluctuates with respect to the nominally set position. Since the photon polarization is not directly measured, but obtained by fitting the experimentally-measured photon spectra to theoretical curves that do not describe well the variations of the coherent edge with time, the determination of the average photon polarization for a sample of events in one of our energy bins has multiple stages. Here we give a brief description of the procedure followed in this analysis.

We make use of the standard g9a polarization tables [64], which contain the photon polarization and its uncertainty as a function of photon energy and E-counter number. A polarization table was obtained for each setting of electron beam energy,

nominal coherent-edge position, actual coherent-edge position, and polarization-plane orientation (such as $\perp$ or $\parallel$). During the experiment, the scalers connected to the tagger E-counters provide the number of photons per E-counter. These spectra are accumulated over two-second intervals and are written to the data stream in special events. In order to determine the actual energy of the coherent edge during such a 2-s interval, the corresponding photon spectrum is divided by a measured reference incoherent-bremsstrahlung spectrum (taken when the electron beam is incident on amorphous radiator). The actual coherent-edge position is obtained using the spectrum of the ratio (called enhancement spectrum). The enhancement spectrum is not affected by channel-to-channel detector inefficiencies. The actual position of the coherent edge is written to the data stream every two seconds. For each electron-beam energy, photon polarization orientation, and nominal coherent-edge energy, the method used to produce the polarization tables [61] reads and histograms these coherent-edge positions. The histogram provides information about the variation of the coherent edge during the experiment. The range covered by the positions is binned in 2-MeV wide bins, and for each bin the corresponding enhancement photon-energy spectrum is constructed. The polarization values in the tables were then obtained by fitting theoretical curves to the enhancement spectra. The theoretical curves are from a calculation of the coherent bremsstrahlung, which takes into account experimental specifics, such as electron energy, radiator, collimation, etc. Quantities that are difficult to estimate a priori, such as smearing due to beam divergence, multiple scattering, and beam spot size, or the amplitude of the main coherent peak, are free parameters in the fit. The procedure is iterative and is fully described in [61, 62]. An example of the photon polarization as a function of photon energy for nominal coherent-edge position of 1.5 GeV in g9a is shown in fig. 3.4. With this procedure the photon polarization is determined with small uncertainty for photon energies within 200 MeV from the coherent-edge position. Beyond this range, the uncertainties are

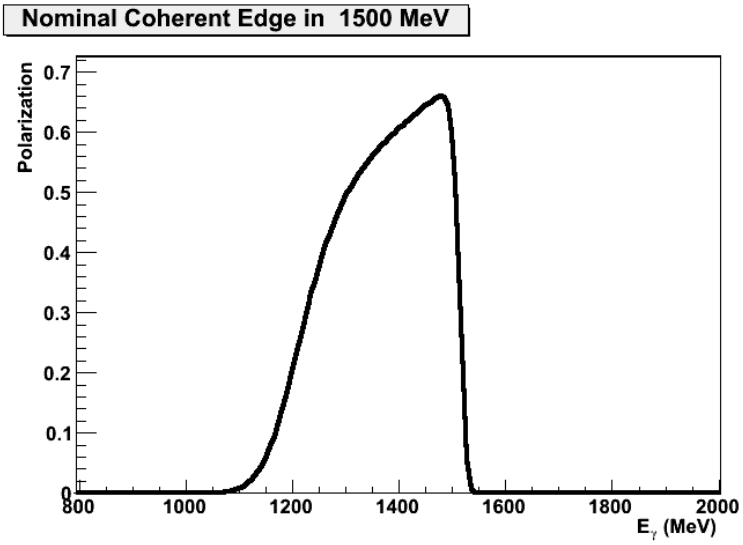

Figure 3.4 Magnitude of photon polarization as a function of photon beam energy as determined in the polarization table for nominal coherent-edge position of 1.5 GeV.

large, which makes those data unusable for extraction of observables that depend on photon-beam polarization.

In order to make use of the polarization tables, in our analysis for every physics event in CLAS, we first determine the actual position of the coherent edge, $E_{CohEdge}$, and the energy of the photon, E_γ, that initiated the reaction in the target. We accept only these events for further analysis, for which the energy of the photon was within 200 MeV below the coherent edge, i.e.,

$$E_{CohEdge} - 200 \text{ MeV} < E_\gamma < E_{CohEdge} \tag{3.1}$$

As mentioned above, in the experiment the position of the coherent edge is read every 2 seconds, and written in a special event in the data stream. In the analysis, we correlate all the physics events collected during that 2-s period with the special event recorded at the end of the period and assign that coherent edge to these physics events. The physics events collected during the next 2 seconds are assigned an actual coherent edge recorded at the end of that 2-s period and so on. Then, for every

physics event, we read the polarization from the corresponding polarization table. In the table, the value of photon polarization is given for discrete values of photon energies that are 9 MeV apart. For a given physics event in which the photon had energy of E_γ, we find in the table the entry with the closest larger photon energy and assign the corresponding photon polarization to that physics event. The photon polarization for a given kinematic bin is obtained as the average polarization of all physics events in that bin, which have passed all our selection criteria. If there is background contribution in this sample of physics events, we assume that the average polarizations of the signal and background are the same.

At the time of writing of this dissertation, there was no precise estimate of the overall systematic uncertainty of the method for estimating the photon-beam polarization. Since the self-consistency of the polarization can be controlled within 15% [65], in this work we use the value of 15% as an estimate of the systematic uncertainty of the photon-beam polarization.

3.4 FROzen Spin Target (FROST)

The experiment discussed here made use of the Hall-B FROzen Spin Target (FROST) [66] that was specifically designed and constructed at Jefferson Lab for the N* program. The polarized-target sample consists of 1.5-mm-diameter frozen butanol (C_4H_9OH) beads loaded into a 5-cm long, 1.5-cm diameter cylinder (target cap), which is made of Polychlorotrifluoroethylene (PCTFE) material. The cap is attached to a 25-cm long stainless-steel tube by a 0.13-mm thick aluminum vacuum window. The center of the target cap coincides with the center of the CLAS. Figure 3.5 shows a schematic diagram of the target.

The free protons in the butanol are polarized outside of the CLAS via Dynamic Nuclear Polarization in a magnetic field of 5 T and temperature of 200 – 300 mK. The target is then cooled down to frozen-spin temperature of about 30 mK and a weak

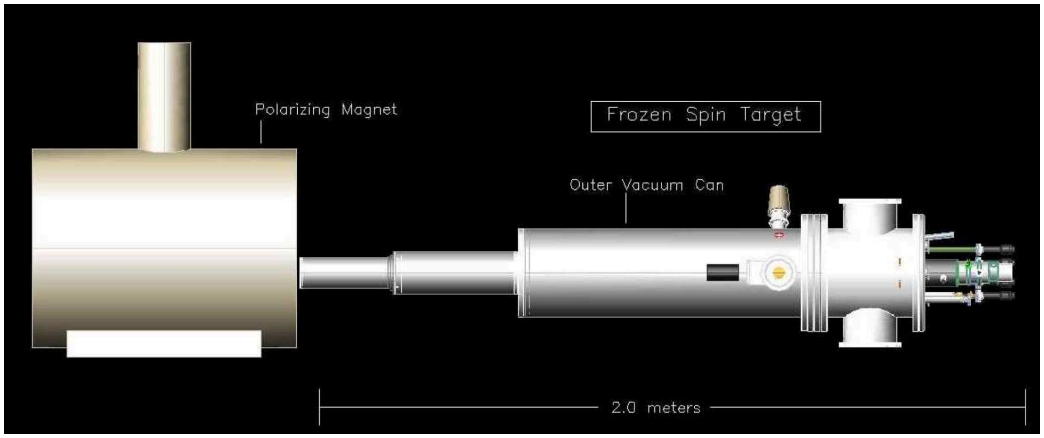

Figure 3.5 Schematic diagram of the FROST cryostat.

magnetic field created by a holding coil is turned on to maintain the polarization. The target is then inserted in the CLAS. A solenoid holding field of 0.56 T was used to maintain longitudinal polarization (this experiment), while a dipole field of 0.5 T was used for transversely polarized protons. The thickness of the holding coil is small, approximately 1 mm, to minimize the energy loss of outgoing particles. The degree of proton polarization was measured by means of the nuclear magnetic resonance (NMR) method [49, 136]. The average starting longitudinal polarization in the positive state was 84% and in the negative spin state was -86%. The relaxation time of the proton polarization was of the order of several thousand hours: with beam on the target, the polarization loss was about 1% per day. The use of FROST did not decrease significantly the angular acceptance of CLAS, particles scattered up to 135° in polar angle were detected.

Since scattering off unpolarized nucleons bound in the carbon and the oxygen nuclei in the butanol sample contributes a large amount of background, two additional targets for background studies were mounted in the target cryostat, outside of the holding coil: a 1.5-mm thick carbon foil and a 3.5-mm CH_2 foil, placed about 6 cm and 16 cm, respectively, downstream from the butanol. Full details of the FROST can be found in [67, 66].

In order to extract polarization observables from data, we need to know not only the polarization of the photon beam, but also of the target. The degree of proton polarization was measured by means of the nuclear magnetic resonance (NMR) method [67, 66]. In the g9a experiment, the free protons in the butanol target were polarized parallel (positive helicity) or anti-parallel (negative helicity) to the photon-beam direction. Figure 3.6 shows the helicity and the polarization degree of the target as a function of run number. The minimum target polarization degree was ap-

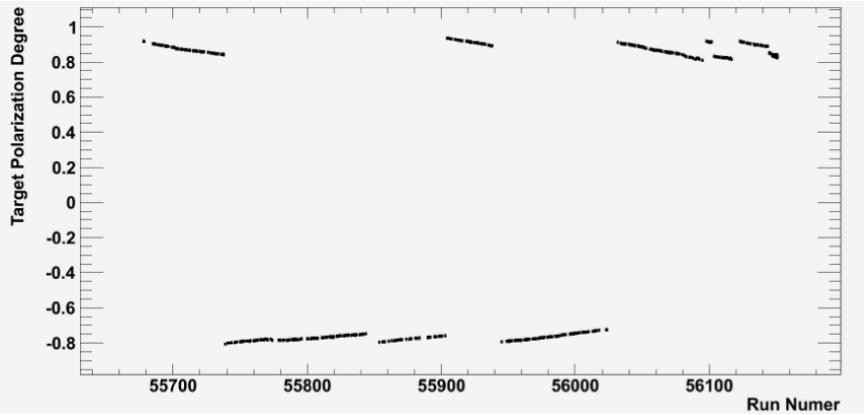

Figure 3.6 Target polarization as a function of run number for the g9a experiment. The experiment begins with run 55678 and ends with run 56151. The run range shown contains runs taken with linearly- and circularly-polarized photons. The runs analysed in this work are specified in Table 3.1.

proximately 72% and the maximum was around 90%. In the experiment, the target polarization is known as a function of run number. Systematic uncertainties in the target polarization have been estimated to be $\approx 6\%$ [68].

As the figure shows, the helicity of the target was flipped several times during the experiment, so that for each nominal coherent edge position data were taken with both positive and negative helicity. The change of target helicity, as well as the rotation of the polarization of the photon beam, were done in order to reduce the systematic uncertainty of the extracted polarization observables.

3.5 The CLAS detector

The CEBAF Large Acceptance Spectrometer (CLAS) [69] is installed in the experimental Hall B and is the main detector for large-acceptance experiments at Jefferson Lab. The CLAS is composed of multi-layer detector systems, each of which plays a unique role in particle tracking and identification.

The detector is radially symmetric around the beam line and encloses the experimental target. CLAS can operate with various types of polarized or unpolarized cryogenic, solid, or gas targets of various lengths. In the experiment discussed here, the beam was incident on a longitudinally polarized butanol target that was positioned at the center of the CLAS. The main component of the CLAS is the toroidal magnet (torus), which is used for momentum spectrometry. In real-photoproduction experiments, such as the one discussed here, the first detector surrounding the target is the start counter (ST) [70], which is used to determine the vertex time of a particle. ST is followed by three layers of drift chambers (DC) [71], which are used for tracking, electromagnetic calorimeters (EC) [72, 73] for detection of neutrals, time-of-flight counter (TOF) [74], and Cherenkov counter (CC) [75] for detection of the scattered electron in electroproduction experiments. Figures 3.7 and 3.8 show a side- and a down-stream view, respectively, of the CLAS.

The angular coverage of the CLAS is from 8° to 142° in polar angle and from 0° to 360° (excluding the angles occupied by the superconducting coils) in azimuthal angle. This angular acceptance is much larger compared to the acceptances of the spectrometers in Halls A and C, however the CLAS precision is lower as a compromise. Detailed description of each of the CLAS subsystems used in the g9a experiment is given in the following sections.

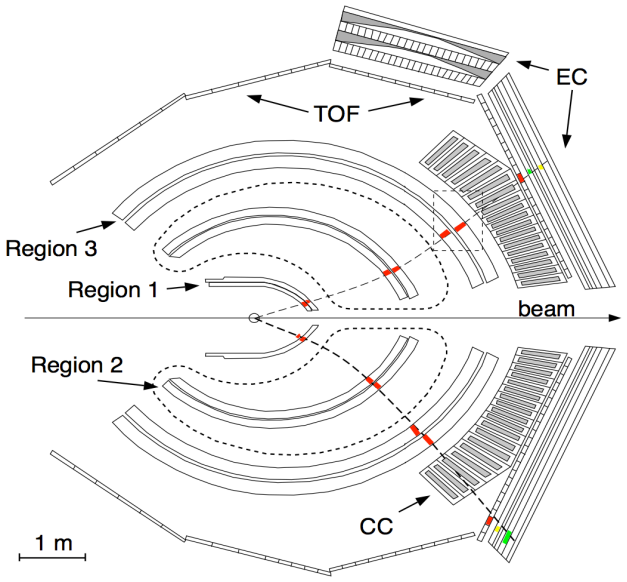

Figure 3.7 Sideview of the CLAS detector. At the center of the CLAS is the 5-cm long FROST target. One can see the three regions of drift chambers, the Cherenkov counter, the time-of-flight counter, and the electromagnetic calorimeter. The start counter, which surrounds the target before region 1 DC, is not shown. The short-dash line around Region 2 DC indicates the area of the magnetic field. The two dashed lines represent outbending particle trajectories. The figure is from Ref. [71].

Superconducting torus magnet

The torus magnet [76] consists of six superconducting coils, which separate the detector into six independent magnetic spectrometers (sectors) that are symmetrically positioned around the beam line. The space between each two coils is filled with tracking and timing detectors. The maximum current the coils can operate at is 3860 A, which provides a maximum field integral of 2.5 T·m at the most forward polar angle and a field integral of 0.6 T·m at 90°. In the experiment discussed here, the torus operated at a lower current, that provided maximum field of 1918 T. With a magnetic field that is stronger at small polar angles than at larger angles, the charged particles scattered in the forward direction are bent such that they can pass through all detectors in the CLAS. Figure 3.9 shows a map of the absolute magnetic-field-

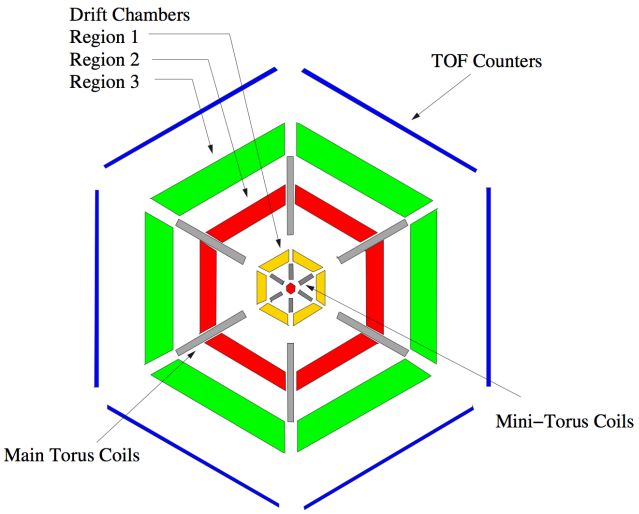

Figure 3.8 Downstream view of the CLAS detector. The six-sector structure of the CLAS can be seen. Each sector covers azimuthal-angle range of 60°. The mini-torus was not used in the g9a experiment. The figure is from Ref. [69].

strength between any two coils. With this field geometry, the charged particles are only bent radially, while their azimuthal angle is unchanged. Also, the geometry of the coils is such that the space at the center of the CLAS is field free, which allowed for the operation of a polarized target in this experiment.

Start counter

The start counter [70] is the first detector through which outgoing particles pass after they leave the target. The detector consists of 24 paddles (4 in each sector) of plastic scintillator surrounding the target. Each paddle has a straight section of 50.2 cm and a shorter, tapered end (”nose“) that is bent at 45° (see Fig. 3.10). With this geometry, the overall length of the start counter is 62 cm and its polar angular coverage matches well the polar-angle range covered by the CLAS. The light produced by a particle in a ST scintillator paddle is transported by a light guide to a photomultiplier tube, which then converts it to an electric signal. The amplitude and the time of the signal are digitized by an Analog-to-Digital Converter (ADC), and Time-to-Digital

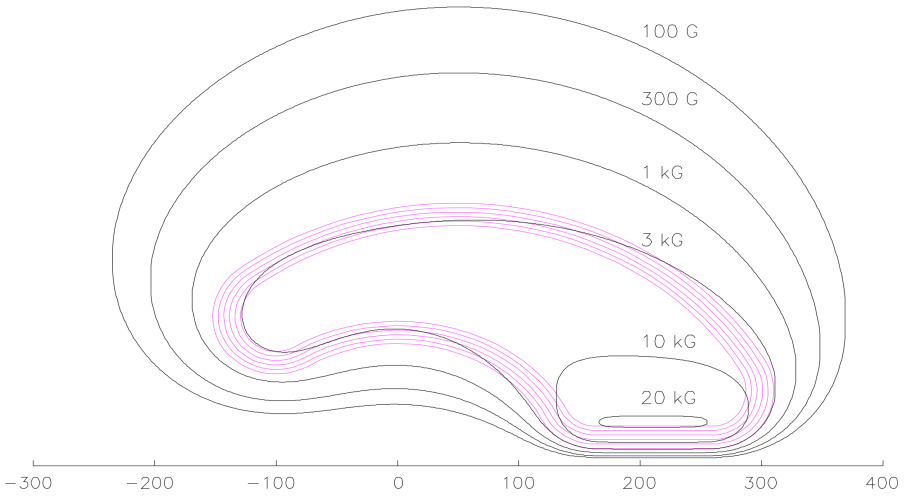

Figure 3.9 Absolute magnetic-field strength between a pair of coils. One can see that a large volume around the center of the CLAS is field-free. The polarized target for this experiment was positioned in this volume and the toroidal magnetic field did not have an effect on its operation. The figure is from Ref. [77].

Converter (TDC), respectively, for further analysis. The signal is also used in the CLAS trigger. During data processing, the TDCs are calibrated and their values are converted to times. In data analyses, the ST time is used to determine the time of the interaction at the vertex (CLAS vertex time). A comparison of the CLAS vertex time with the photon vertex time (which is independently measured by the tagger), allows to synchronize the particles detected in the CLAS with the tagged photon that initiated the reaction. This allows to significantly reduce accidental background events. In order to be able to resolve the 2.004-ns time structure of the electron-beam bunches, the timing resolution of the detector must be smaller than 2.004 ns and is typically between 290 ps and 330 ps depending on the hit position of the particle along a paddle. Although, ADC values were recorded in the data stream, they were not converted to energy during the data processing, and the energy loss deposited in ST was not used in this analysis.

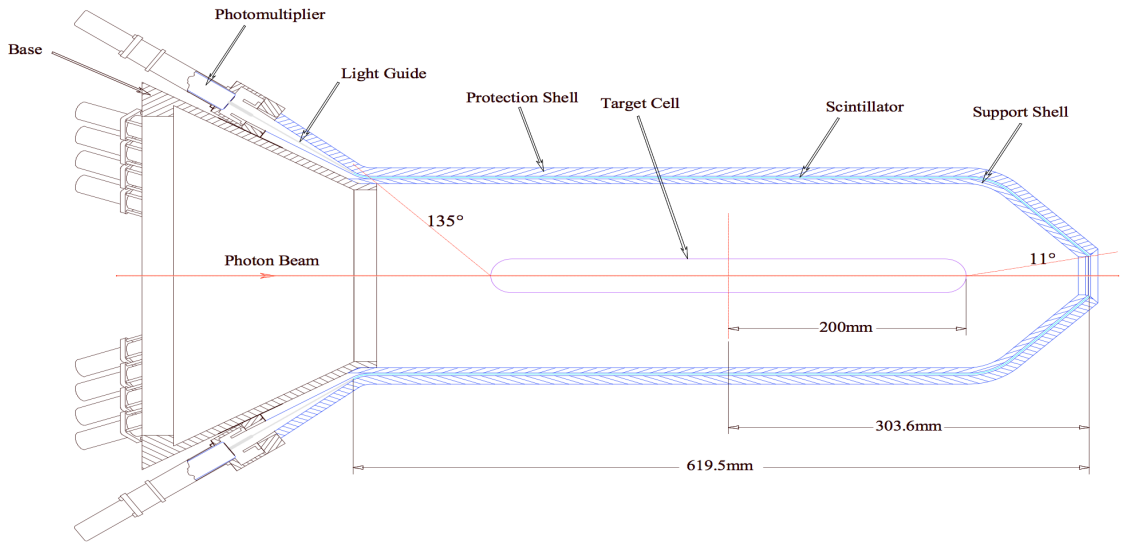

Figure 3.10 A side view of the start counter. In the forward direction each scintillating paddle is tapered and bent into a "nose". On the back one can see the light guides and the photomultipliers. The target shown is the standard 40-cm long unpolarized target. In this experiment the target was 5-cm long, which somewhat increases the forward and the backward polar angular coverage than as shown. The figure is from [70].

Drift chambers

The CLAS Drift Chamber system [71] consists of three regions of multi-layered drift chambers surrounding the target. Region 1 DC is located between the start counter and the most-inner part of the torus coils. Thus, charged-particle tracks in this region are straight lines. Region 2 DC is located radially outward from Region 1, and occupies the space of largest magnetic field, while Region 3 DC is outside of the magnetic coils where the magnetic field is fairly weak. Each DC region contains up to 12 layers of hexagonal drift cells (see example for Region 3 in Fig. 3.11). The field wires, made of 140-μm-diameter gold-plated aluminum are located at the vertices of each hexagon, while the sense wires, made of 20-μm-diameter gold-plated tungsten, are at the center of the hexagons. The cell radius increases as the radial distance from the target increases, and varies from 15 mm – 17 mm in Region 1 to 40 mm – 45 mm in Region 3. The chambers are filled with a gas mixture of 90% Ar and 10% CO_2.

When a charged particle passes through a cell it ionizes the gas and the ionization electrons are collected at the sense wire. The electric pulse resulting from a hit is shaped and amplified, and then directed to TDC. During data processing the TDC values are converted to times, the electron drift times are determined and converted to drift distances. The latter allows for precise determination of the position of a hit in each layer. The track of the particle is reconstructed by a fit to the hits in all layers.

By extrapolating a particle track from Region 1 to the target, the position of the vertex as well as the polar and the azimuthal angles of the particle at the vertex are determined. The magnitude of the three-momentum vector is obtained from the track curvature and the magnetic field. The CLAS resolution in polar angle is approximately 1 mrad and in azimuthal angle is about 4 mrad. The momentum resolution depends on polar angle and varies between 0.5% and 2%.

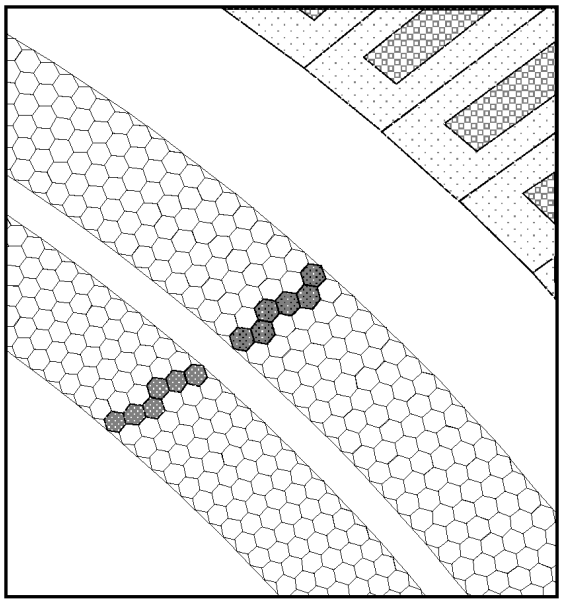

Figure 3.11 A zoomed-in schematic view of Region 3 DC. The hexagonally shape drift cells and their arrangement in 12 layers can be seen. The shaded hexagons indicate the path of a charged particle, which causes signals on the sense wires. The figure is from Ref. [71].

Time-of-flight Counter

The TOF subsystem [74] is placed outside of the magnetic field and for large polar angles is the most outward detector in the CLAS. At forward angles it is located between the electromagnetic calorimeter and the Cherenkov counter. The TOF is segmented in polar angle and in each sector it consists of 57 scintillator paddles. All the paddles are 5.08 cm thick, while their length and width varies with polar angle. The paddles are arranged such that each one is normal to the average particle trajectory (see Fig. 3.12). The polar-angle coverage of the TOF is from 8° to 142°. The readout of the paddles is similar to the readout of the ST scintillators. The signal due to the passage of a particle is directed to an ADC and a TDC, which are both calibrated during data processing. The timing signal is also used in the event trigger during data taking. The main purpose of the detector is to determine the time of flight of charged particles, which, when combined with the momentum information obtained from the tracking and the magnetic field, provides the main charged-particle identification (PID) in CLAS analyses. The timing resolution of the paddles varies with length and is between 100 ps and 160 ps. The system allows distinguishing pions from kaons for momenta up to 2 GeV/c. The combination of charged-particle energy loss in the TOF and the particle momentum could be used for a secondary particle identification, although this method is not very precise due to the large energy straggling.

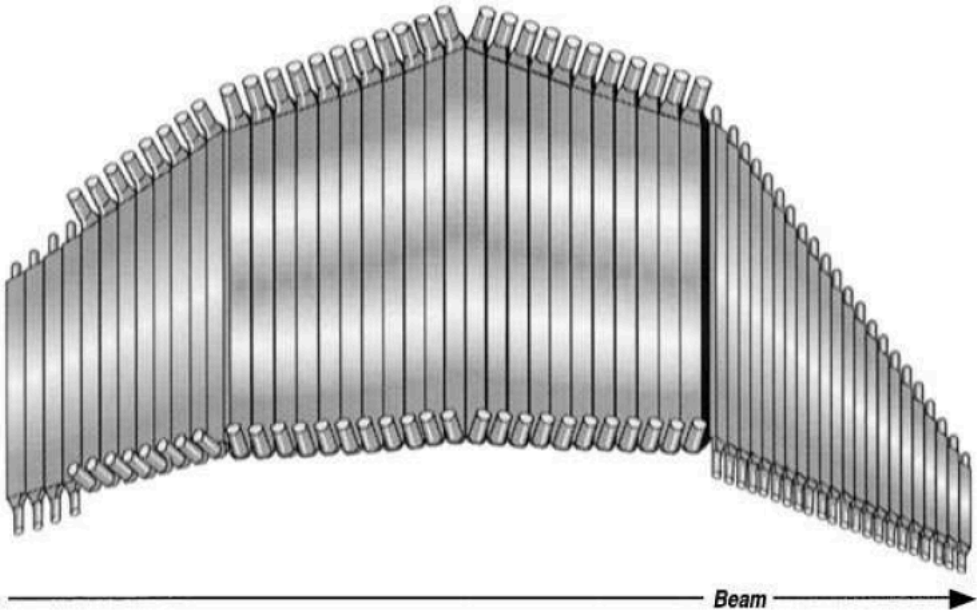

Figure 3.12 A 3-dimensional view of the TOF counter in one sector. The arrangement of the scintillation paddles in four different panels, as well as the photomultiplier tubes of each paddle, can be seen. The figure is from Ref. [74].

Chapter 4

Data Analysis: Particle and reaction channel identification

Two or three of the final-state particles in the $\gamma p \to p\pi^+\pi^-$ reaction were detected in CLAS. The charge and momentum of each particle were reconstructed from tracking information. Time of flight, momentum, and path-length data were used for particle identification. The initial-state photon for the event was selected by a coincidence requirement between the photon tagger and CLAS. The missing-mass technique was used to identify the reaction of interest. A discussion of the methods used to select the reaction of interest is given in the subsequent sections.

4.1 Raw-Data Analysis and Event Preselection

The data from CLAS experiments are stored on tape for analysis in a BOS format. BOS is a dynamic memory-management system for input and output of sets of data. Initial processing of the data, referred to as *cooking*, converts the raw data (digitized signal and time information of the detector's ADCs, TDCs, and channel IDs) using calibration parameters into meaningful quantities, such as particle tracks, energy, and time. The *cooked* BOS files, which include all the information needed for data analysis, contain events with detected particles from many reaction channels. To reduce the size of the files for easier data management, an initial filtering (skimming) to include only event candidates of the double-charged pion reaction channel was undertaken. This filtering reduces the size of each BOS file from 2 GB to about

14 MB. The BOS files use a specific data structure, so called *banks*, to classify the CLAS data. Hundreds of banks were defined for various purposes, whereas only data stored in a few banks are needed for analysis, like the EVNT bank, which records physical information of final-state particles, and the TAGR bank, which records the energy and timing information of incoming photons. The skimming not only removed a large number of events, but also significantly reduced the amount of saved banks to only those needed for this analysis.

The reaction of interest $\gamma p \to p\pi^+\pi^-$ has three final-state particles. Due to limited detector acceptance and efficiency, it is typical that not all three final-state particles are detected in CLAS. With the use of the missing-mass technique the reaction can be reconstructed with the identification of only two of the three final-state particles. This induces three possibilities to select event candidates for the reaction channel based on charge alone. Specifically, if all the three final-state particles were detected, the event should include two particle tracks of positive charge and one track of negative charge. If one of the positive particles was missed (either the proton or the π^+), only one positive track and one negative track would be recorded in the BOS file. The third possibility is that the negative particle, π^-, would be missing and only the two positive tracks would be recorded. For this reason, only events satisfying one of the above three possibilities were stored for subsequent analysis. Table 4.1 shows the information recorded for events that satisfy the initial skimming, including information from the EVNT, the SCPB (bank that holds information from the time-of-flight detector) and STPB (bank that holds information from the start counter) banks.

The reconstruction of the reaction channel using the missing-mass technique requires information of the incident photon that initiated the reaction. The incident photon energies and times at the center of CLAS are saved in the TAGR bank for all reconstructed photons. The tagger reconstruction software assigns a photon for

Table 4.1 The bank information kept for the skimmed files. The third column gives the number of tracks recorded for each event.

Quantity	Bank	Number	Comment
Run	HEAD	1	Run number
Event	HEAD	1	Event number, starts with 1 at run begin
Time	HEAD	1	Event Time, UNIX time
PhoE	TAGR	All	Photon Energy for each photon recorded
TPho	TAGR	All	Time of the photon after RF correction
Mom	EVNT	2 or 3	Particle momentum for each track
Beta	EVNT	2 or 3	Particle velocity for each track
Cx	EVNT	2 or 3	X direction (cosine) at track origin
Cy	EVNT	2 or 3	Y direction (cosine) at track origin
Cz	EVNT	2 or 3	Z direction (cosine) at track origin
ScPdHt	SCPB	2 or 3	Time-of-flight paddle number
StHid	STPB	2 or 3	Starter Counter paddle
Vert X	MVRT	1	x coordinate of the reaction vertex
Vert Y	MVRT	1	y coordinate of the reaction vertex
Vert Z	MVRT	1	z coordinate of the reaction vertex
Coh Edge	EPIC	1	Coherent edge
Coh Plan	EPIC	1	Coherent plane
Coh Radi	EPIC	1	Coherent radiator

each electron hit that passes a set of consistency checks developed to strongly reduce background and random electron hits not associated with a bremsstrahlung event. The photon timing information is used to select the photon that initiated the reaction and its energy is used to reconstruct the reaction channel. Additional information that is needed for the analysis is also saved, such as the reaction vertex from the MVRT bank, information about the run from the HEAD bank, and the incident photon-polarization orientation and coherent-edge position from the EPIC bank.

4.2 Exclusion of bad TOF scintillator paddles

The timing information used for particle identification comes from the time-of-flight detector. Ideally, the timing calibration would be of equal quality for all the paddles. Typically, however, some paddles are unstable with time, while others have a very low efficiency. In such cases the timing calibration procedure fails and the reconstructed times are wrong. If kept in the analysis, particles detected in such paddles would not be identified properly and will contribute to the background. In order to reduce background events, we have studied the performance of the TOF detector, identified problematic paddles, and removed the corresponding events from our data sample.

Figures 4.1, 4.2, and 4.3 show the number of protons, π^+, and π^-, respectively, for each TOF paddle in each sector. The yields are obtained after particle identification was done. The choice of logarithmic scale for the y axis emphasizes paddles for which the application of the PID criteria leads to significant reduction in particle yields. Paddles with yields that are at least an order of magnitude smaller than the yields of the neighboring paddles, systematically for all particle yields, are removed from the analysis. For example, paddles 44 and 46 in sector 6 have about 10 times smaller number of events than the neighboring paddles 43, 45, and 47, for proton, π^+, and π^-, and are excluded from the analysis.

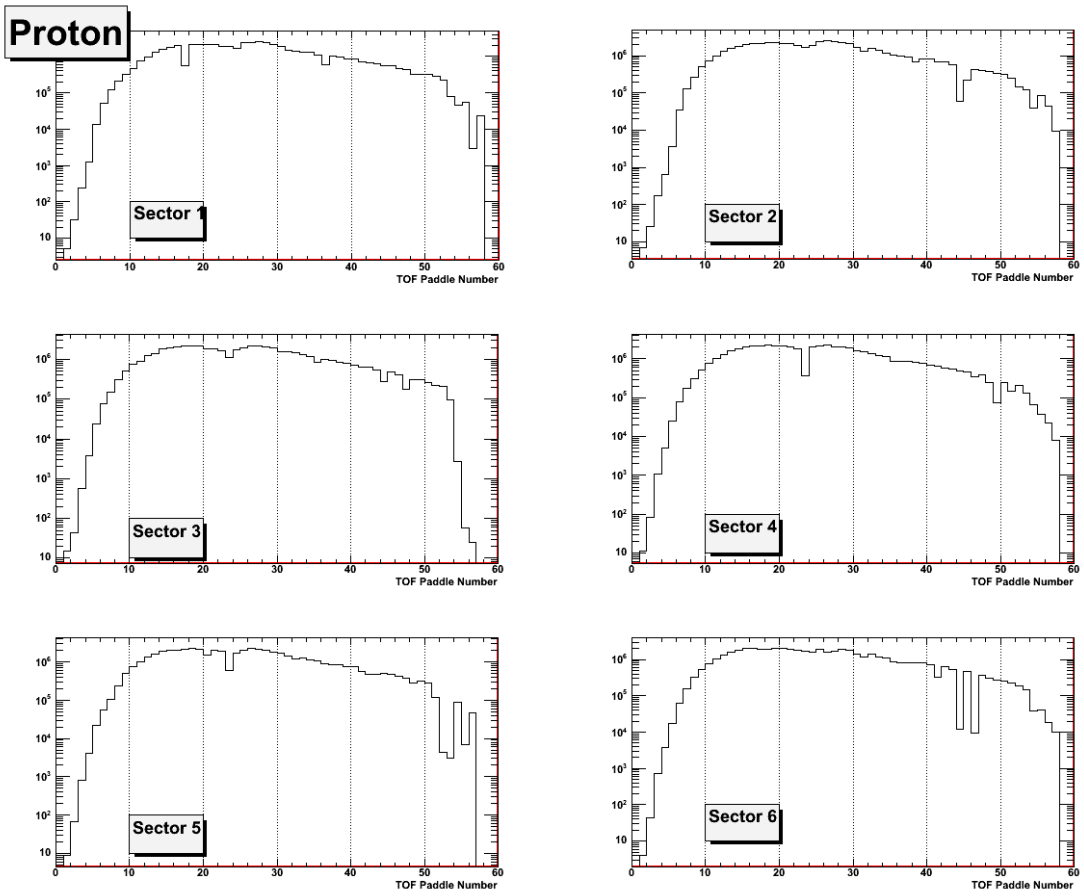

Figure 4.1 Proton event distributions as a function of TOF paddle number for each CLAS sector. Paddles with bad timing, leading to significant loss of events after applying particle-identification criteria, show as dips in the distributions and are excluded from further analysis.

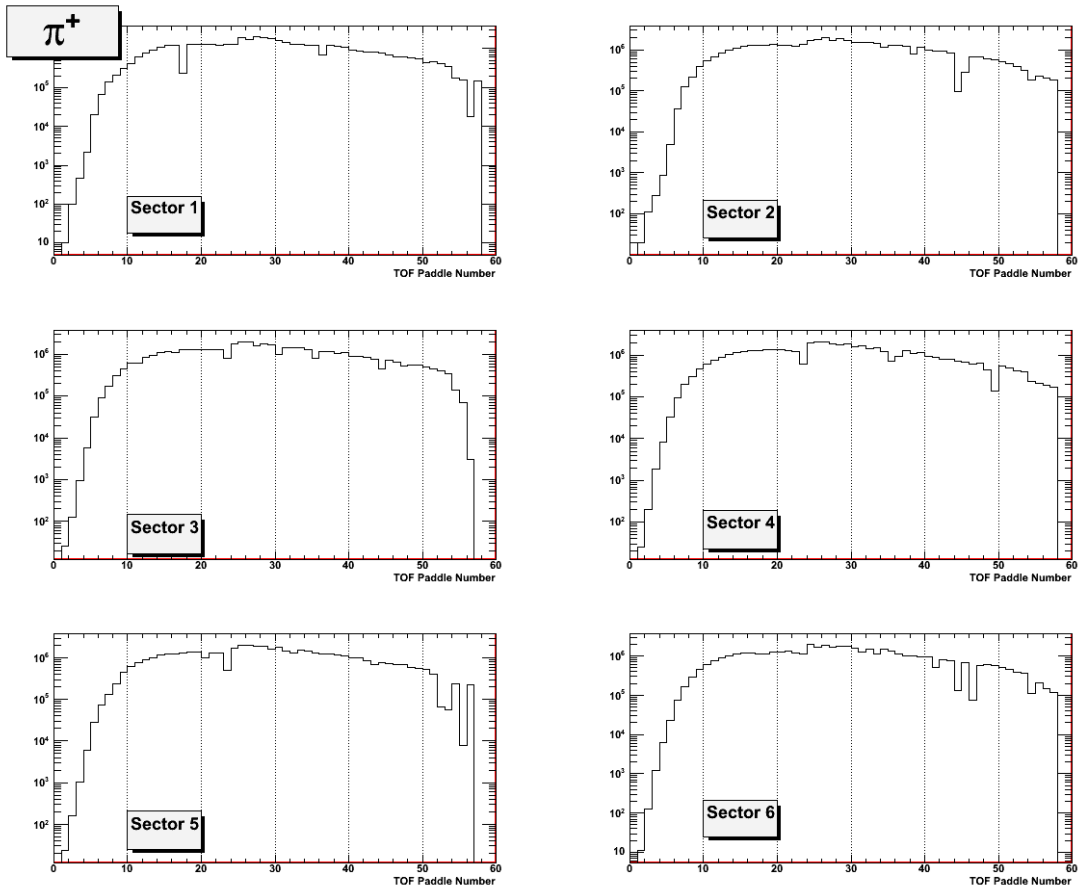

Figure 4.2 π^+ event distributions as a function of TOF paddle number for each CLAS sector. Paddles with bad timing, leading to significant loss of events after applying particle-identification criteria, show as dips in the distributions and are excluded from further analysis.

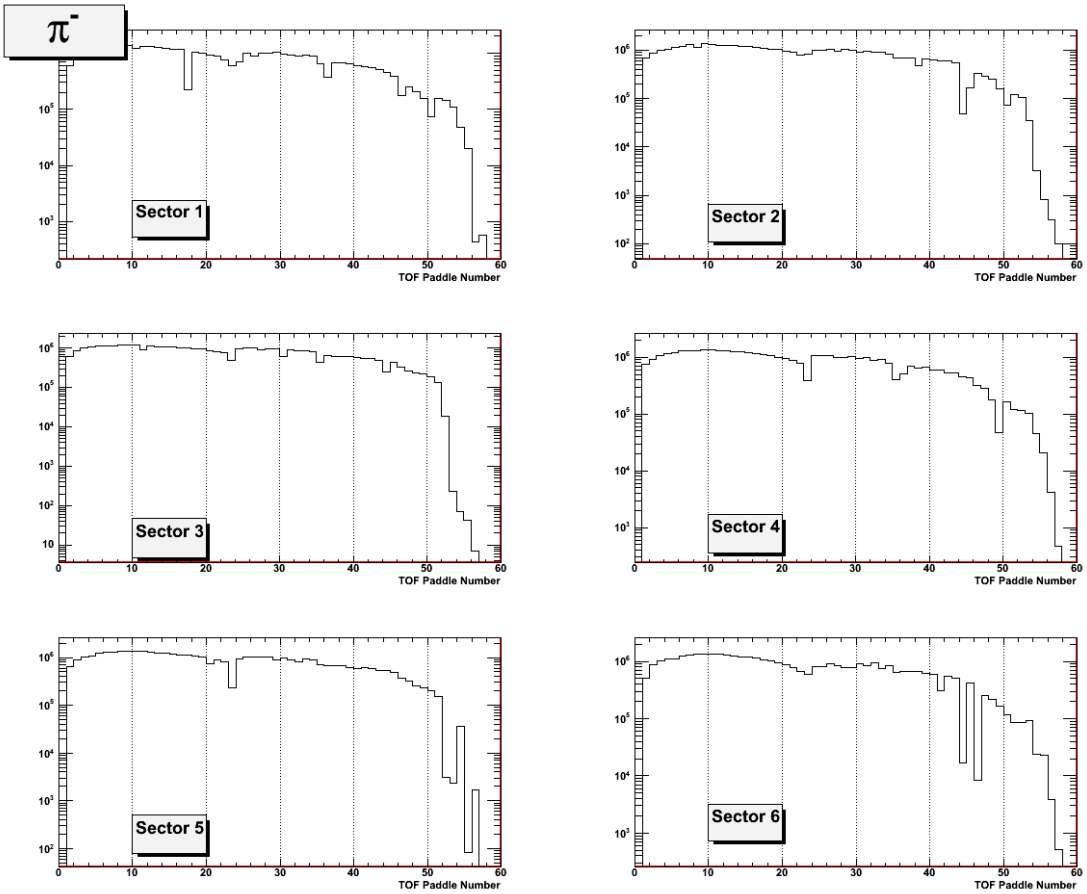

Figure 4.3 π^- event distributions as a function of TOF paddle number for each CLAS sector. Paddles with bad timing, leading to significant loss of events after applying particle-identification criteria, show as dips in the distributions and are excluded from further analysis.

Table 4.2 lists all TOF paddles that were removed from the analysis; tracks with hits in any of those paddles were not used. The removal of these tracks reduces the detector acceptance. It does otherwise not affect the extraction of the polarization observables from asymmetry measurements.

Table 4.2 List of bad TOF paddles excluded in the analysis.

Sector	Paddle Number			
1	17	36	56	
2	44	45	54	
3	23	35	44	
4	23	49		
5	23	52	53	55
6	41	44	46	

4.3 Reaction Vertex

The goal of this work is to extract polarization observables on the free proton for the reaction of interest. However, the polarized target in the experiment contains not only polarized unbound protons but also nucleons bound in the nuclei of carbon and oxygen. In addition, the target window contains aluminum. Nuclear reactions on the bound nucleon produce significant background that needs to be subtracted in the analysis. Since one cannot separate kinematically this background from the events of interest, the g9a ran with two additional unpolarized targets, a carbon and a polyethylene foils installed downstream of the butanol (see Chapter 3). The carbon target was used to study the bound-nucleon background. In the g9a experiment, however, events from a reaction vertex close to the carbon target were contaminated with events off free, unpolarized hydrogen. The effect of this hydrogen contamination was accounted for in the subsequent analysis; see Sec. 5.4. Events from all the targets were collected in the data sample. In order to identify the target in which the

reaction occurred (butanol, carbon, or polyethylene), the reaction vertex recorded in the MVRT bank is used. For the analysis of the polarized target asymmetry, the data of events that originated in the butanol target are used. Events that originate from the carbon and polyethylene targets are used for background subtraction and yield normalization, respectively. The reaction vertex is also used to determine the vertex time of the reaction from the photon time at the tagger.

The final-state particles in the $\gamma p \to p\pi^+\pi^-$ reaction can result from direct production or resonance decay. There are three main resonances, Δ^{++}, Δ^0, and ρ^0 [8], which can contribute to this reaction. Their very short lifetimes ($\sim 10^{-24}$ s) result in decay path-lengths that are much shorter than the detectors' resolution. Therefore, it is reasonable to assign to all the final-state particles the same reaction vertex.

The x, y, and z components of the reaction vertex recorded in the MVRT bank were determined by a least-squares fit to the reconstructed tracks, minimizing the distance of closest approach between them. Figure 4.4 shows the distribution of our 2- and 3-charged-track events over the z-component of the vertex. Events originating in the butanol target form the broad peak centered at 0 cm and are selected with a z-vertex cut between -3 and 3 cm, removing contamination from events that originate in the carbon target. Events originating in the carbon form a peak at 6 cm and are selected with a z-vertex cut between 5 cm and 9 cm. The peak at 16 cm is due to events coming from the polyethylene target.

In addition to the z-vertex cut, x- and y-vertex cuts were applied to exclude events that originate outside of the target. To accommodate the cylindrical shape of the FROST target, a circular cut of radius of 1.5 cm was applied. Figure 4.5 shows a two-dimensional distribution of the x and y vertex components of the two- and three-charged track events, as well as the cut applied.

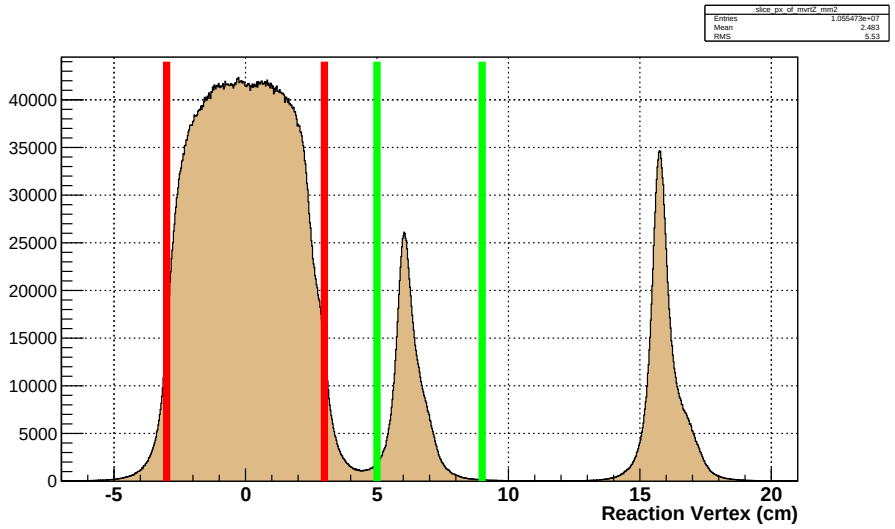

Figure 4.4 Event distribution over the z-component of the reaction vertex. The solid red lines indicate the cut selecting events originating in the butanol target, while the solid green lines show the cut applied to select events produced in the carbon target. The peak at 16 cm contains events from the polyethylene target. One can see that the CLAS provides a reasonable resolution to separate between the targets of interest in g9.

4.4 Particle identification

Particles were identified by means of the time-of-flight (TOF) technique. The measured time of flight for each track was compared with values that were calculated using path-length and momentum information from the drift chambers and an assumption about the particles' mass. The calculated and the measured values agree if the asummed mass is the mass of the detected particle. Table 4.3 lists the nominal mass of each candidate particle. ΔTOF is the difference of the two time of flights

$$\Delta TOF = TOF_{meas} - TOF_{calc}. \tag{4.1}$$

The track was then assigned the nominal mass of the candidate particle if $|\Delta TOF|$ was within a predetermined cut range (± 2 ns for protons and ± 1 ns for π mesons).

The value TOF_{meas} in Eq. (4.1) was measured by the time-of-flight detector, whereas the TOF_{calc}, was calculated using the particle's path length, L, from tracking

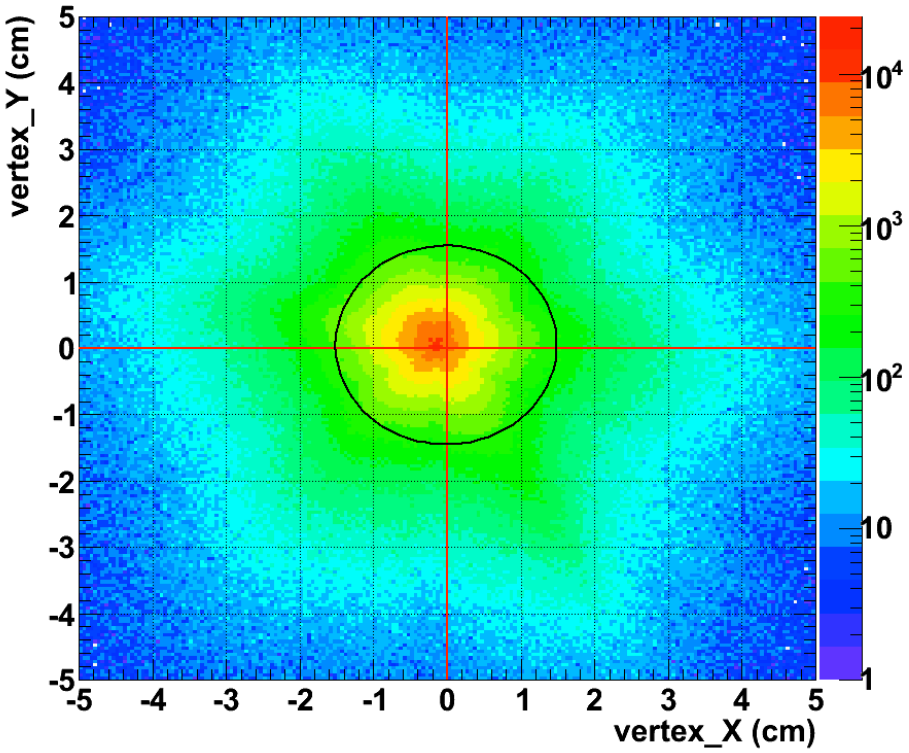

Figure 4.5 Distribution of the reaction-vertex x and y components (transverse to the beam line). The black circle indicates the radial vertex cut applied in this analysis.

Table 4.3 The nominal masses of candidate particles and the notation used for each track to identify the final-state particles.

Candidate	Mass (MeV)	Time Difference
p	938.27	ΔTOF_{proton}
π^+	139.57	ΔTOF_{π^+}
π^-	139.57	ΔTOF_{π^-}

and the calculated particle's speed, β_{calc},

$$TOF_{calc} = L \cdot \frac{1}{\beta_{calc}}. \tag{4.2}$$

The value, β_{calc}, was calculated using the measured momentum from the drift cham-

bers and an assumption about the particle's mass (see Tabel 4.3)

$$\beta_{calc} = \frac{p}{\sqrt{p^2 + m^2_{assumed}c^2}}. \tag{4.3}$$

For p/π^+ separation, two ΔTOF values were calculated; one assuming a proton mass (ΔTOF_{proton}) and one assuming a π^+ mass (ΔTOF_{π^+}). The ΔTOF that is within the cut range identifies the particle. If both ΔTOF values are outside of the cut ranges the event is removed from subsequent analysis. The same holds if both ΔTOF values were within the cut ranges, since particle identification could not be performed. The negative track is identified as π^-, if the ΔTOF_{π^-} value is within the cut range. Figures 4.6 and 4.7 show ΔTOF as a function of momentum for the positive tracks, assuming a π^+ and a proton mass, respectively, while Fig. 4.8 shows the ΔTOF as a function of momentum for negative tracks. The red lines indicate the cut used to identify the particles.

4.5 Photon selection

As mentioned before, photon selection is necessary for the reaction reconstruction. The photon selection is done using the time coincidence at the event vertex between the photon and the particles detected in CLAS. The tagger timing resolution ($\sim$ 110 ps) allows to distinguish events that originate from different beam bunches (produced every 2 ns) and to identify the photon that initiated the reaction. The coincidence vertex time is determined as

$$\Delta t_{vertex} = t_{TAGR} - t_{CLAS}, \tag{4.4}$$

where t_{TAGR} and t_{CLAS} are the time of the photon and the particle time, respectively, at the event vertex. The photon time at the center of CLAS, T_{tag}, is reconstructed by the tagger software using the electron hit timing information. Propagation of the photon to the event vertex is taken into account in the calculation of t_{TAGR}

$$t_{TAGR} = T_{tag} + \frac{z_{vertex}}{c}. \tag{4.5}$$

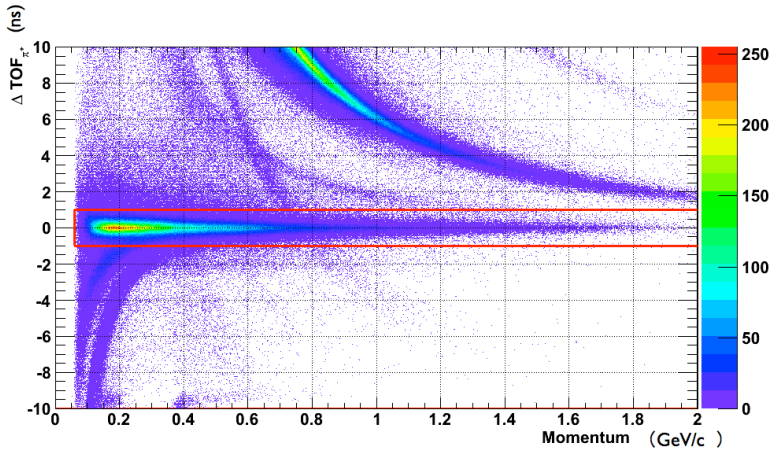

Figure 4.6 ΔTOF_{π^+} distribution as a function of momentum. The solid red lines indicate the cut used to identify the π^+. The high-intensity structure at $\Delta TOF_{\pi^+} > 0$ is due to true protons. The structure, which crosses the cut contains events with bad TOF paddles. These events are removed with the exclusion of bad TOF paddles. At $\Delta TOF_{\pi^+} < 0$ and low momenta one can discern structures containing positrons and positively-charged muons.

The vertex time for each track, t_{CLAS}, was calculated using time-of-flight information (hit time, T_{tof}, and path length from event vertex, L_{tof}) and the track's calculated speed using its nominal mass (after particle identification)

$$t_{CLAS} = T_{tof} - \frac{L_{tof}}{\beta_{calc}}. \tag{4.6}$$

The coincidence time Δt_{vertex} is calculated for each reconstructed photon and each track. Figure 4.9 shows the coincidence times using all final-state particles after particle identification. Typically, in CLAS analyses the photon that initiated the reaction is chosen as the photon that produces the smallest coincidence time Δt_{vertex} with the fastest final-state particle. In an attempt to reduce background channels, as well as events with recorded tracks that originate from different beam bunches, the photon selection in this anslysis contains additional criteria. Specifically, all reconstructed final-state tracks must yield Δt_{vertex} that selects the same photon. The

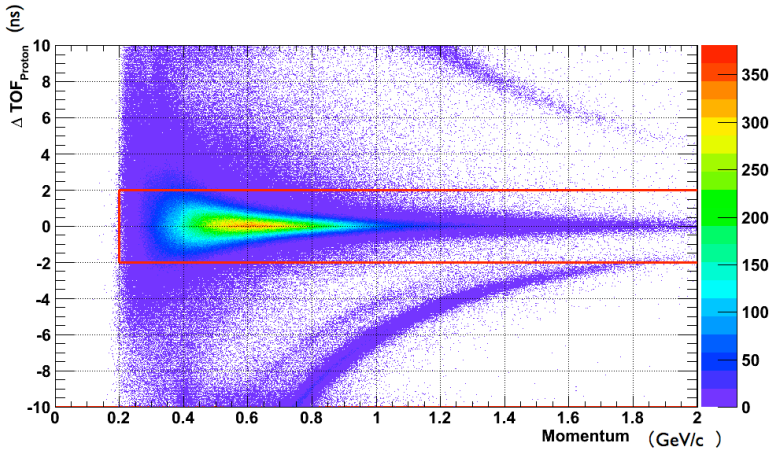

Figure 4.7 ΔTOF_{proton} distribution as a function of momentum. The solid red lines indicate the cut used to identify the protons. The high-intensity stripe at $\Delta TOF_{proton} < 0$ contains true π^+.

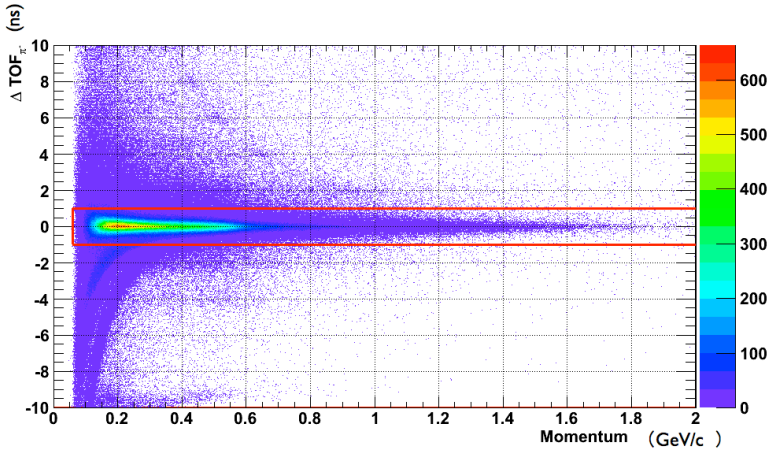

Figure 4.8 ΔTOF_{π^-} distribution as a function of momentum. The solid red lines indicate the cut used to identify the π^-. At $\Delta TOF_{\pi^-} < 0$ and low momenta one can discern structures containing electrons and negatively-charged muons.

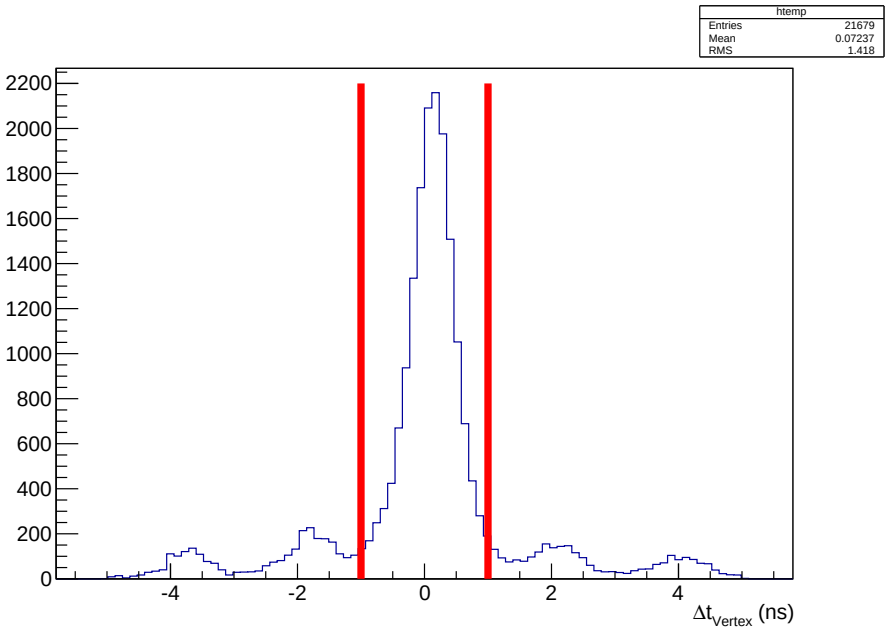

Figure 4.9 Vertex time difference distribution and ±1 ns cut range for photon-CLAS coincidences.

photon selected for each track is the one that results in the smallest coincidence time. In addition to this, if the selected photon is associated with a coincidence time larger that ±1 ns the event is removed from subsequent analysis (see Fig. 4.9). Finally, events in which all final-state particles yield more than one photon within the ±1 ns timing coincidence window, are also removed from subsequent analysis.

4.6 Identification of the reaction channel

Due to the limited CLAS acceptance, not all three final-state particles in the reaction $\gamma p \to p\pi^+\pi^-$ are always detected. It was mentioned before that with the use of the missing-mass technique the reaction can be reconstructed by detecting two of the three final-state particles. Four different cases, or *topologies*, are used to reconstruct this reaction, as described in Table 4.4. The reaction is then reconstructed separately for each topology using its associated data. For example, topology 1 contains only events in which three final-state particles (two positive and one negative) are detected

Table 4.4 Topology classification.

Topology	1^{st} positive track	2^{nd} positive track	Negative track
1	p	π^+	π^-
2	Missing	π^+	π^-
3	p	Missing	π^-
4	p	π^+	Missing

in CLAS, whereas topologies 2 and 3 contain only events with two final-state particles (one positive and one negative) detected in CLAS.

The missing-mass technique makes use of the four-momentum-vector conservation in an exclusive reaction. The four-momentum conservation of the $\gamma p \rightarrow p\pi^+\pi^-$ process states

$$\widetilde{p}_\gamma + \widetilde{p}_{target} = \widetilde{p}_p + \widetilde{p}_{\pi^+} + \widetilde{p}_{\pi^-}, \tag{4.7}$$

where $\widetilde{p}_i$ is the four vector of the particle i. For topologies 2 – 4, where one of the final-state particles is missing, four-momentum conservation yields

$$\begin{aligned}
\widetilde{p}_{missing} &= \widetilde{p}_\gamma + \widetilde{p}_{target} - \widetilde{p}_{\pi^+} - \widetilde{p}_{\pi^-} \text{ for Topology 2,} \\
\widetilde{p}_{missing} &= \widetilde{p}_\gamma + \widetilde{p}_{target} - \widetilde{p}_p - \widetilde{p}_{\pi^-} \text{ for Topology 3,} \\
\widetilde{p}_{missing} &= \widetilde{p}_\gamma + \widetilde{p}_{target} - \widetilde{p}_p - \widetilde{p}_{\pi^+} \text{ for Topology 4.}
\end{aligned} \tag{4.8}$$

Using Eq. (4.8), the invariant-mass squared of the missing particle is calculated as the square of its four-momentum

$$MM^2 = (\widetilde{p}_{missing})^2 = E^2_{missing} - \vec{P}^2_{missing}. \tag{4.9}$$

Figures 4.10 – 4.13 show the missing-mass squared distributions calculated using Eq. (4.9) for events from the butanol target and for all topologies. For each topology the distribution contains a gaussian peak at the mass-squared of the missing particle, containing events produced off free protons, and a background. Quasi-free production off bound nuclei does not lead to such a narrow missing-mass peak due to significant

smearing caused by Fermi motion. A missing-mass cut is applied to identify the missing particle and select the reaction. For the subsequent extraction of polarization observables, for each topology, only events within a $\pm 2\sigma$ range from the mean of the gaussian peak in the missing-mass distributions were used. The same cut ranges were also applied to the scaled carbon distribution to calculate the dilution factors (see Chapter 5).

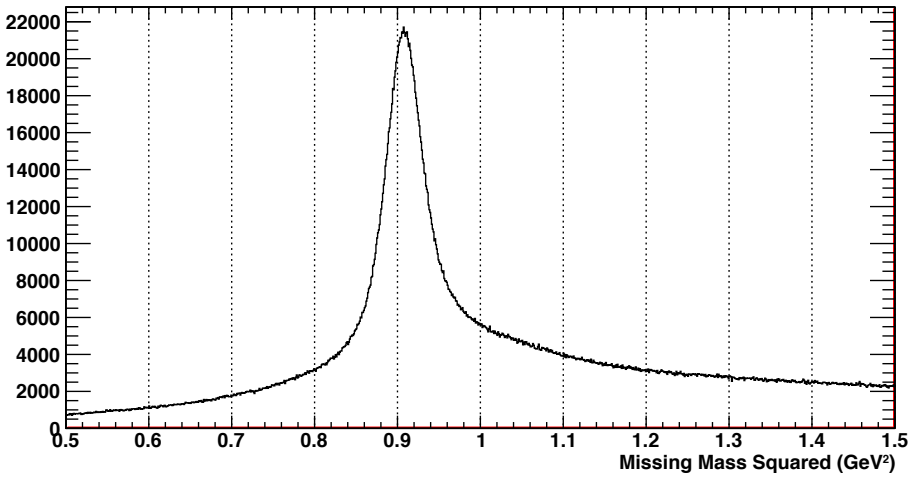

Figure 4.10 Missing-mass squared distribution in $\gamma p \to \pi^+\pi^- X$ for butanol-target events of topology 1 (all particles detected).

In topology 1, there is no particle missing, $\widetilde{p}_{misssing} = 0$. Due to finite detector resolution the missing-mass squared distribution shows in this case a narrow asymmetric peak centered at zero. However, the bound-nucleon background is easier to determine in a distribution of the missing-mass squared in the $\gamma p \to \pi^+\pi^- X$ reaction, although the proton has been detected in topology 1; Fig. 4.10.

Topology 3 shows a very interesting structure; see Fig. 4.12. A clear peak indicating the missing π^+ is seen along with an additional peak located at slightly lower values of missing-mass squared. This interesting feature of topology 3 was found to be a result from a reaction off a bound neutron in the butanol target. Specifically, events with detected p and π^- could also come from the $\gamma n \to p\pi^-$ reaction. Fig-

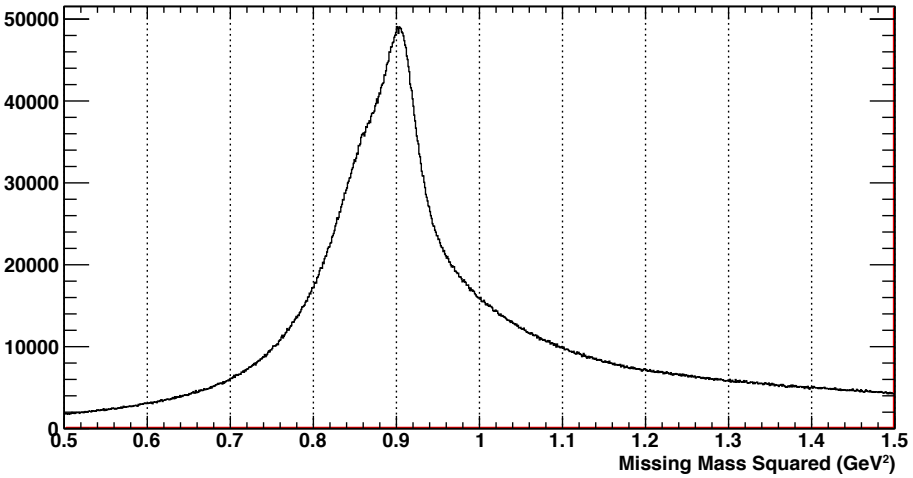

Figure 4.11 Missing-mass squared distribution in $\gamma p \to \pi^+\pi^- X$ for butanol-target events of topology 2 (p undetected). The shoulder at the low MM^2 side of the peak is due to background events.

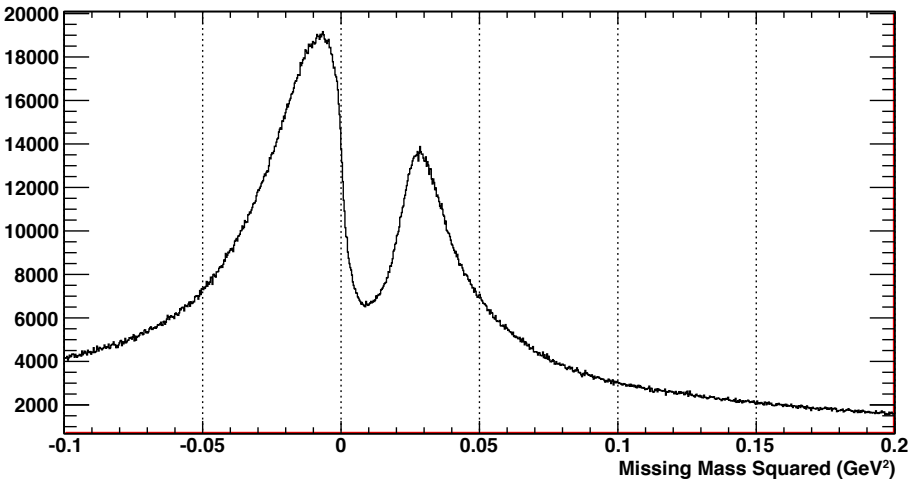

Figure 4.12 Missing-mass squared distribution in $\gamma p \to p\pi^- X$ for butanol-target events of topology 3 (π^+ undetected). The peak at $MM^2 < 0$ is due to background events off bound neutrons, $\gamma n \to p\pi^-$.

ure 4.14 shows the missing-mass squared in $\gamma p \to p\pi^- X$ as a function of the invariant mass of the pX pair. Two peaks are visible; one from the $\gamma p \to \pi^+\pi^- p$ reaction with $X = \pi^+$ and one from the background reaction $\gamma n \to p\pi^-$ with $X = 0$. To reduce contributions from this reaction, a two-dimensional cut was applied that preserves

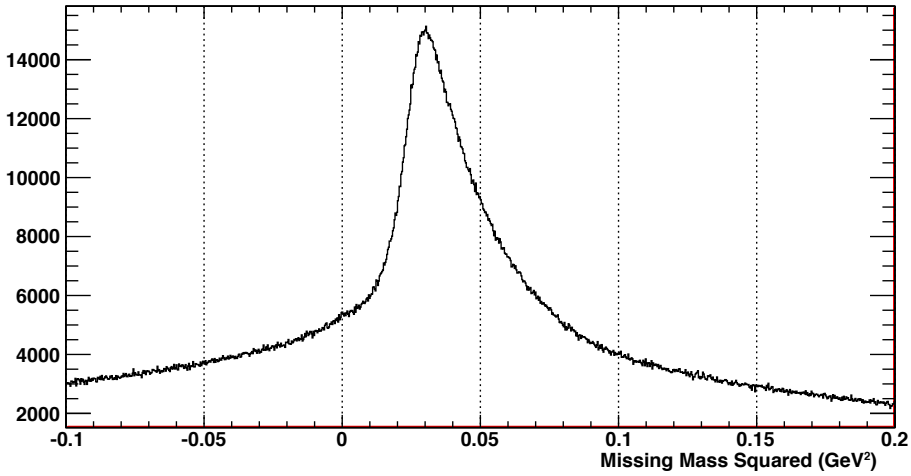

Figure 4.13 Missing-mass squared distribution in $\gamma p \to p\pi^+ X$ for butanol-target events of topology 4 (π^- undetected).

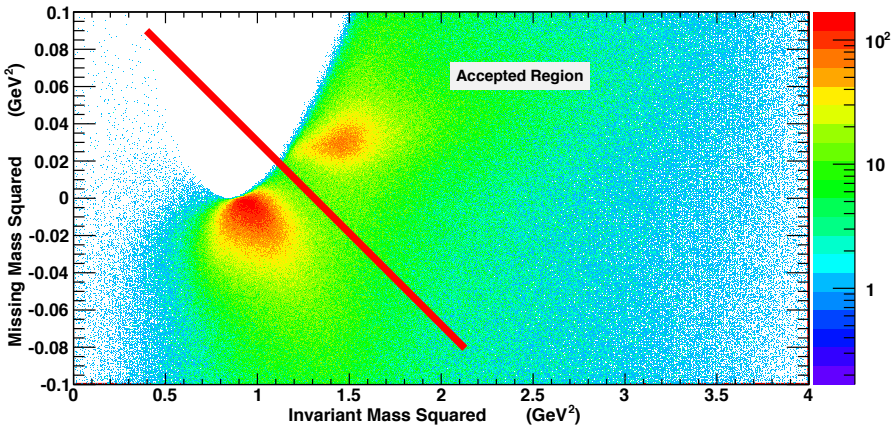

Figure 4.14 Missing-mass squared of $\gamma p \to p\pi^- X$. vs. invariant mass of pX pair. The left peak is from the reaction $\gamma n \to p\pi^-$, $X = 0$, and the right is from the double-pion photoproduction reaction, $X = \pi^+$.

most of the events from the $\gamma p \to p\pi^+\pi^-$ reaction. This cut is indicated by the red line in Fig. 4.14. The result of this cut is depicted in Fig. 4.15, which shows the missing mass squared of the reaction $\gamma p \to p\pi^- X$ before (red histogram) and after (black histogram) the two-dimensional cut mentioned above.

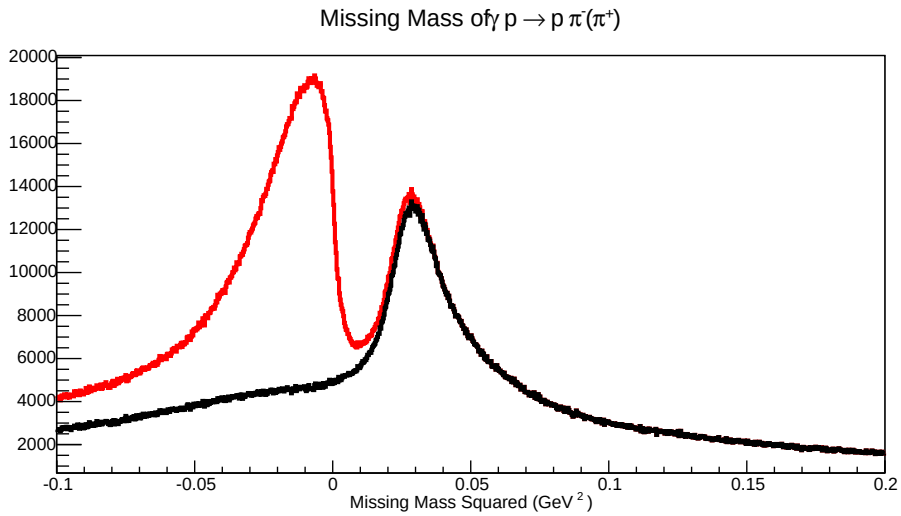

Figure 4.15 Missing-mass squared distributions of topology 3, $\gamma p \to p\pi^-(\pi^+)$ before (red curve) and after (black curve) the two-dimensional cut shown in Fig. 4.14. One sees that the cut significantly reduces background contribution from $\gamma n \to p\pi^-$ events.

Chapter 5

Data Analysis: Asymmetries and polarization observables

After the reconstruction of the reaction channel, experimental asymmetries were determined from linear combinations and ratios of yields from various beam and target polarization configurations. The polarization observables were extracted by simple fits to those expressions. This chapter covers the main steps taken to construct these asymmetries and determine the polarization observables of the reaction $\gamma p \to p\pi^+\pi^-$.

5.1 Construction of asymmetry

Equation (2.5) indicates how the reaction rate I depends on the polarization observables of interest and the angle β, defined as the angle between the scattering plane and the orientation of the photon polarization. During this experiment, data were collected using two orientations of the photon polarization; one parallel to the Hall-B floor (*Para* or $||$), and the other perpendicular to the Hall-B floor (*Perp* or $\perp$). The angle β can be calculated using the azimuthal angle ϕ_{lab} of the reaction plane as measured by the CLAS detector, and an angle α that denotes the orientation of the photon polarization in the lab,

$$\beta = \alpha - \phi_{lab}. \tag{5.1}$$

Figure 5.1 shows the angle β and how this is calculated using the orientation of the photon polarization orientation (angle α). Specifically, the angle β for the *Para*

($\alpha = 0$) and *Perp* ($\alpha = \pi/2$) orientation of the photon polarization are

$$\begin{aligned} \beta &= -\phi_{lab} \qquad \text{for } \textit{Para} \text{ orientation}, \\ \beta &= \frac{\pi}{2} - \phi_{lab} \qquad \text{for } \textit{Perp} \text{ orientation} \end{aligned} \tag{5.2}$$

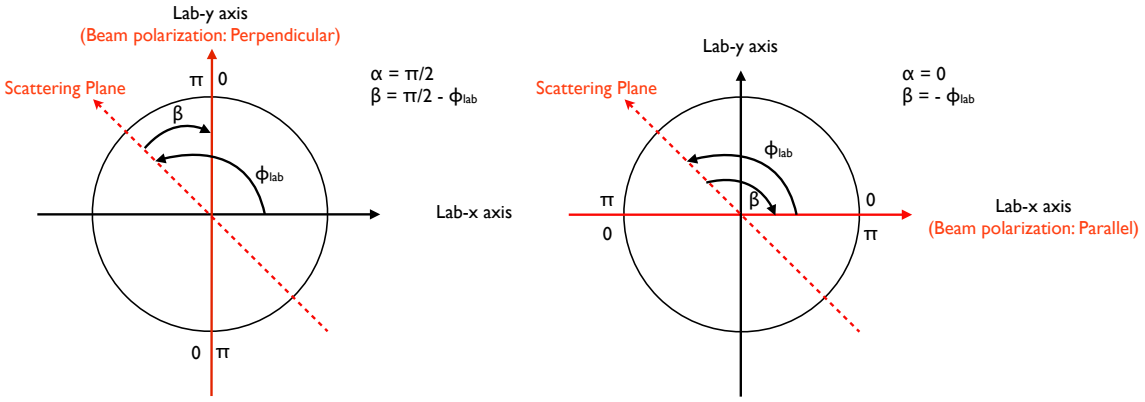

Figure 5.1 A visual representation of the angle β that denotes the angle between the scattering plane and the orientation of the photon polarization for the *Perp* (left) and *Para* (right) orientation.

The β-angular dependence of the reaction rate can then be expressed as functions of the lab angle, ϕ_{lab},

$$\text{for} \quad \textit{Para} \begin{cases} \sin 2\beta = -\sin 2\phi_{lab}, \\ \cos 2\beta = \cos 2\phi_{lab} \end{cases} \tag{5.3}$$

$$\text{for} \quad \textit{Perp} \begin{cases} \sin 2\beta = \sin 2\phi_{lab}, \\ \cos 2\beta = -\cos 2\phi_{lab} \end{cases} \tag{5.4}$$

The production rate, or reaction cross section, for the four different configuration of target ($+$ or $-$) and photon polarization ($\perp$ or $||$) can be written in terms of the

angle ϕ_{lab} (using Eq. (5.3) and Eq. (5.4))

$$\begin{aligned}
\sigma_+^{\perp} &= \sigma_0\{(1+\Lambda\cdot P_z)+\delta[\sin 2\phi_{lab}(I_s+\Lambda\cdot P_z^s)-\cos 2\phi_{lab}(I_c+\Lambda\cdot P_z^c)]\}\\
\sigma_+^{\parallel} &= \sigma_0\{(1+\Lambda\cdot P_z)+\delta[-\sin 2\phi_{lab}(I_s+\Lambda\cdot P_z^s)+\cos 2\phi_{lab}(I_c+\Lambda\cdot P_z^c)]\}\\
\sigma_-^{\perp} &= \sigma_0\{(1-\Lambda\cdot P_z)+\delta[\sin 2\phi_{lab}(I_s-\Lambda\cdot P_z^s)-\cos 2\phi_{lab}(I_c-\Lambda\cdot P_z^c)]\}\\
\sigma_-^{\parallel} &= \sigma_0\{(1-\Lambda\cdot P_z)+\delta[-\sin 2\phi_{lab}(I_s-\Lambda\cdot P_z^s)+\cos 2\phi_{lab}(I_c-\Lambda\cdot P_z^c)]\},
\end{aligned} \tag{5.5}$$

with Λ and δ representing the degree of target and photon polarizations (the signs that result from the scalar product of $\vec{\Lambda}$ with the polarization observables are already incorporated in the above equations).

Linear combinations of the different polarized cross section allow to isolate the observables of interest. Three linear combinations of the cross sections in Eq. (5.5) are used to isolate the unpolarized cross section, the single-polarization observable P_z, and the double-polarization observables P_z^s and P_z^c.

$$\begin{aligned}
(\sigma_+^{\perp}+\sigma_+^{\parallel})+(\sigma_-^{\perp}+\sigma_-^{\parallel}) &= 4\sigma_0\\
(\sigma_+^{\perp}+\sigma_+^{\parallel})-(\sigma_-^{\perp}+\sigma_-^{\parallel}) &= 4\sigma_0\Lambda P_z\\
(\sigma_+^{\perp}-\sigma_+^{\parallel})-(\sigma_-^{\perp}-\sigma_-^{\parallel}) &= 4\sigma_0\delta\Lambda(\sin 2\phi_{lab}\cdot P_z^s+\cos 2\phi_{lab}\cdot P_z^c)
\end{aligned} \tag{5.6}$$

The construction of asymmetries significantly simplifies the extraction of the polarization observables by removing detector acceptance effects and systematic uncertainties that are related in the determination of the unpolarized cross section σ_0. Two cross-section asymmetries allow the determination of the single- and double-polarization observables, respectively:

$$\frac{(\sigma_+^{\perp}+\sigma_+^{\parallel})-(\sigma_-^{\perp}+\sigma_-^{\parallel})}{(\sigma_+^{\perp}+\sigma_+^{\parallel})+(\sigma_-^{\perp}+\sigma_-^{\parallel})} = \Lambda P_z \tag{5.7}$$

$$\frac{(\sigma_+^{\perp}-\sigma_+^{\parallel})-(\sigma_-^{\perp}-\sigma_-^{\parallel})}{(\sigma_+^{\perp}+\sigma_+^{\parallel})+(\sigma_-^{\perp}+\sigma_-^{\parallel})} = \delta\Lambda(\sin 2\phi_{lab}\cdot P_z^s+\cos 2\phi_{lab}\cdot P_z^c). \tag{5.8}$$

In this analysis, similar expressions for the experimental yield asymmetries were fit with constant and trigonometric functions to determine P_z and P_z^s and P_z^c, respec-

tively. The following sections discuss how these asymmetries can be calculated using the polarized yields.

5.2 Experimental yields

Different polarization orientations of both the beam and target affect the polarized cross sections, which are reflected in the experimental yields; $Y_+^{\perp}$, $Y_+^{\parallel}$, $Y_-^{\perp}$ and $Y_-^{\parallel}$ (see Fig. 5.2).

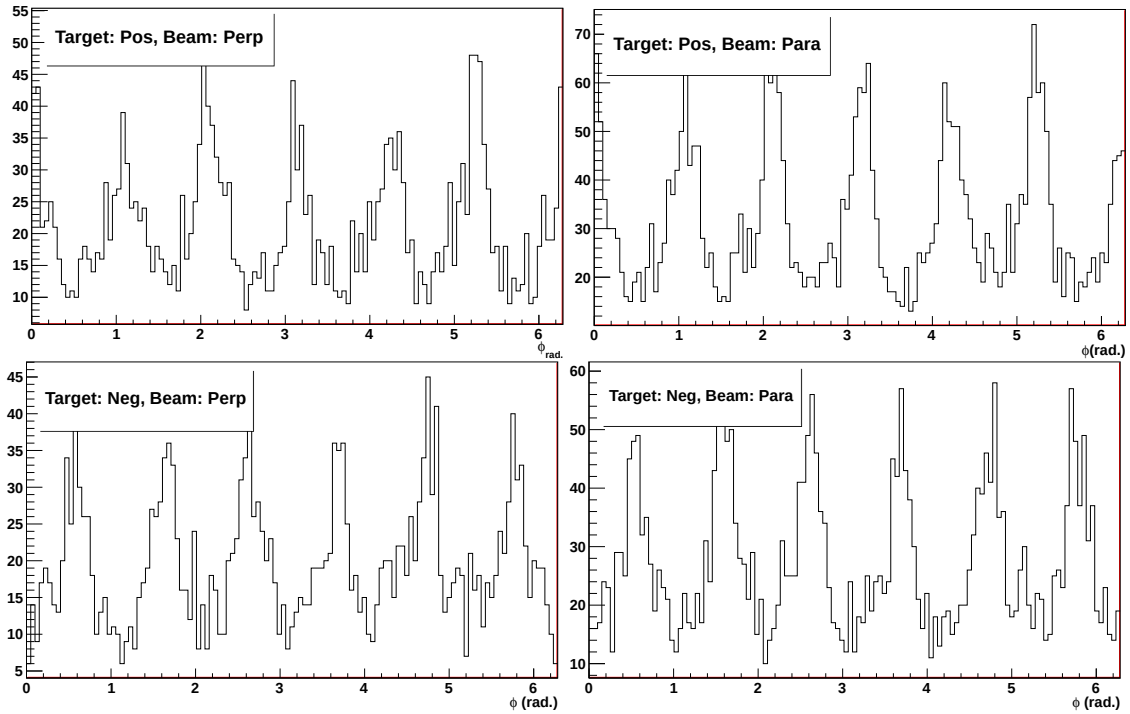

Figure 5.2 The yields for 4 various configurations, where the upper left is the yield of $Y_+^{\perp}$, the upper right is that for $Y_+^{\parallel}$, the lower left is that for $Y_-^{\perp}$ and the lower right is that for $Y_-^{\parallel}$ as a function of the azimuthal angle ϕ_{lab}. The four yields are examples from topology1 and photon energy of 1.3 GeV.

The yields from various beam and target polarization orientations have been obtained from different runs, thus a relative normalization of the yields to the luminosity on those runs is necessary for any further analysis to make the yields comparable. The normalization is implemented by the total number of events from the unpolarized polyethylene target without any cut, η_i, for each polarization configuration i.

The value of η_i is a measure of the photon flux. It is independent of the butanol target polarization and, if integrated over all azimuthal angles, independent of the photon beam polarization. Although the carbon target is also unpolarized, it was not used for normalization as it was already used for the background subtraction. The normalized yield, Y_i, was then obtained from the raw yield, Y_i^{Raw},

$$Y_i = \frac{Y_i^{Raw}}{\eta_i} \tag{5.9}$$

The polarized yields in one kinematic bin can be calculated by integrating the polarized cross sections folded with the detector acceptance A over the width of the kinematic variables ($\Delta\tau$ and $\Delta\phi_{lab}$) defining that bin. The polarized yield for one of the polarization configurations is then expressed as,

$$Y = c\int_{\Delta\tau}\int_{\Delta\phi}\sigma_0(\tau)(1 + P_1(\tau) + P_2(\tau)\sin 2\phi)\cdot A(\tau,\phi)d\phi d\tau \tag{5.10}$$

The variable τ represents all the other kinematic variables in which the yield is integrated over, such as the polar angle and invariant masses $IM_{p\pi^+}$, $IM_{\pi^-\pi^+}$. In Eq. (5.10), $P_1 = \Lambda P_z$ represents the single polarization-observable, while $P_2 = \delta\Lambda P_z^s$ represents the double polarization-observables; the term proportional to P_z^c has been neglected to simplify the expressions. The results for P_z^s apply to P_z^c also.

Under the assumption that the acceptance does not change much within a ϕ bin,

$$\int_{\Delta\tau}\int_{\Delta\phi} A(\tau,\phi)d\phi\, d\tau \approx \int_{\Delta\tau} A(\tau,\phi_i)\Delta\phi\, d\tau,$$
$$\int_{\Delta\tau}\int_{\Delta\phi} A(\tau,\phi)\sin 2\phi\, d\phi\, d\tau \approx \int_{\Delta\tau} A(\tau,\phi_i)\sin 2\phi_i \sin\Delta\phi\, d\tau,$$

Eq (5.10) can be simplified further,

$$Y(\phi_i) \approx c\int_{\Delta\tau}\sigma_0(\tau)\left[\Delta\phi + P_1(\tau)\Delta\phi + P_2(\tau)\sin 2\phi_i \sin\Delta\phi\right] A(\tau,\phi_i)\, d\tau$$

With a new constant, $c' = c \int\limits_{\Delta\tau} \sigma_0(\tau) A(\tau,\phi_i) \Delta\phi \, d\tau$, the yield can be expressed as,

$$Y(\phi_i) \approx c' \frac{\int\limits_{\Delta\tau} \sigma_0(\tau) \left[\Delta\phi + P_1(\tau)\Delta\phi + P_2(\tau) \sin 2\phi_i \sin\Delta\phi\right] A(\tau,\phi_i)\, d\tau}{\int\limits_{\Delta\tau} \sigma_0(\tau) A(\tau,\phi_i) \Delta\phi \, d\tau}$$

$$= c' \left[1 + \frac{\int\limits_{\Delta\tau} \sigma_0(\tau) P_1(\tau) A(\tau,\phi_i)\, d\tau}{\int\limits_{\Delta\tau} \sigma_0(\tau) A(\tau,\phi_i)\, d\tau} + \frac{\int\limits_{\Delta\tau} \sigma_0(\tau) P_2(\tau) A(\tau,\phi_i)\, d\tau}{\int\limits_{\Delta\tau} \sigma_0(\tau) A(\tau,\phi_i)\, d\tau} \sin 2\phi_i \frac{\sin\Delta\phi}{\Delta\phi} \right]$$

$$= c' \left[1 + \bar{P}_1(\phi_i) + \bar{P}_2(\phi_i) \sin 2\phi_i \frac{\sin\Delta\phi}{\Delta\phi} \right]. \tag{5.11}$$

Through the experimental yield the experiment has therefore access to the unpolarized cross section and acceptance weighted averages of the polarization observables. These weighted averages are determined in the present analysis. The ϕ dependence in the averages $\bar{P}_1(\phi_i)$ and $\bar{P}_2(\phi_i)$ disappears exactly if the acceptance of the CLAS factorizes, $A(\tau,\phi) \approx A(\tau)A(\phi)$. In the following we assume that averages are independent of ϕ. The term $\sin\Delta\phi/\Delta\phi$ in Eq. (5.11) accounts for a reduction in the amplitude of the angular distribution when the distribution is binned over finite bin sizes, $\Delta\phi$. The extracted double-polarization observables have been corrected for this effect.

5.3 Determination of asymmetries

In Eqs. (5.7) and (5.8) it was assumed that the beam and target polarization degrees are the same for all four polarization configurations. However, in the experiment events from different runs were taken with degrees of beam and target polarizations. For the four different setups, the degrees of beam and target polarizations are, $\delta_+^\perp$, $\delta_+^\parallel$, $\delta_-^\perp$, $\delta_-^\parallel$ and $\Lambda_+^\perp$, $\Lambda_+^\parallel$, $\Lambda_-^\perp$, $\Lambda_-^\parallel$, respectively. As a consequence, the cross sections are

$$\begin{cases} \sigma_+^{\perp} &= \sigma_0 \left\{ (1 + \Lambda_+^{\perp} P_z) + \delta_+^{\perp} [\sin 2\phi_{lab} (I_s + \Lambda_+^{\perp} P_z^s) - \cos 2\phi_{lab} (I_c + \Lambda_+^{\perp} P_z^c)] \right\} \\ \sigma_+^{\parallel} &= \sigma_0 \left\{ (1 + \Lambda_+^{\parallel} P_z) + \delta_+^{\parallel} [-\sin 2\phi_{lab} (I_s + \Lambda_+^{\parallel} P_z^s) + \cos 2\phi_{lab} (I_c + \Lambda_+^{\parallel} P_z^c)] \right\} \\ \sigma_-^{\perp} &= \sigma_0 \left\{ (1 - \Lambda_-^{\perp} P_z) + \delta_-^{\perp} [\sin 2\phi_{lab} (I_s - \Lambda_-^{\perp} P_z^s) - \cos 2\phi_{lab} (I_c - \Lambda_-^{\perp} P_z^c)] \right\} \\ \sigma_-^{\parallel} &= \sigma_0 \left\{ (1 - \Lambda_-^{\parallel} P_z) + \delta_-^{\parallel} [-\sin 2\phi_{lab} (I_s - \Lambda_-^{\parallel} P_z^s) + \cos 2\phi_{lab} (I_c - \Lambda_-^{\parallel} P_z^c)] \right\} \cdot \end{cases} \tag{5.12}$$

Figure 5.3 shows the values of both beam (upper panel) and target (lower panel) polarizations for various nominal coherent edge settings.

As before, linear combinations of the polarized cross sections, Eq. (5.12), can be used to isolate the single- and double-polarization observables if the differences in the degrees of the beam and target polarizations are taken into account. This is done by scale factors, which are the ratios of the polarization degrees:

$$s_1 = \frac{\Lambda_+^{\parallel}}{\Lambda_+^{\perp}}, \quad s_2 = \frac{\Lambda_-^{\parallel}}{\Lambda_-^{\perp}}, \quad s_5 = \frac{\delta_+^{\parallel}}{\delta_+^{\perp}}, \quad s_6 = \frac{\delta_-^{\parallel}}{\delta_-^{\perp}}, \tag{5.13}$$

and factors, which are combinations of those,

$$s_3 = \frac{\delta_+^{\parallel} + s_1 \delta_+^{\perp}}{\delta_-^{\parallel} + s_2 \delta_-^{\perp}}, \quad s_7 = \frac{\Lambda_+^{\parallel} + s_5 \Lambda_+^{\perp}}{\Lambda_-^{\parallel} + s_6 \Lambda_-^{\perp}}, \quad s_8 = \frac{1 + s_5}{1 + s_6}. \tag{5.14}$$

As the target polarization is independent of the orientation of the beam polarization, as seen in Fig. 5.3, the scale factors s_1 and s_2 are approximately one, and consequently also the scale factors s_3 and s_8. An overview over all scale factors for the various photon energy settings is given in Fig. 5.4.

With these scale factors the linear combinations of the polarized cross sections are

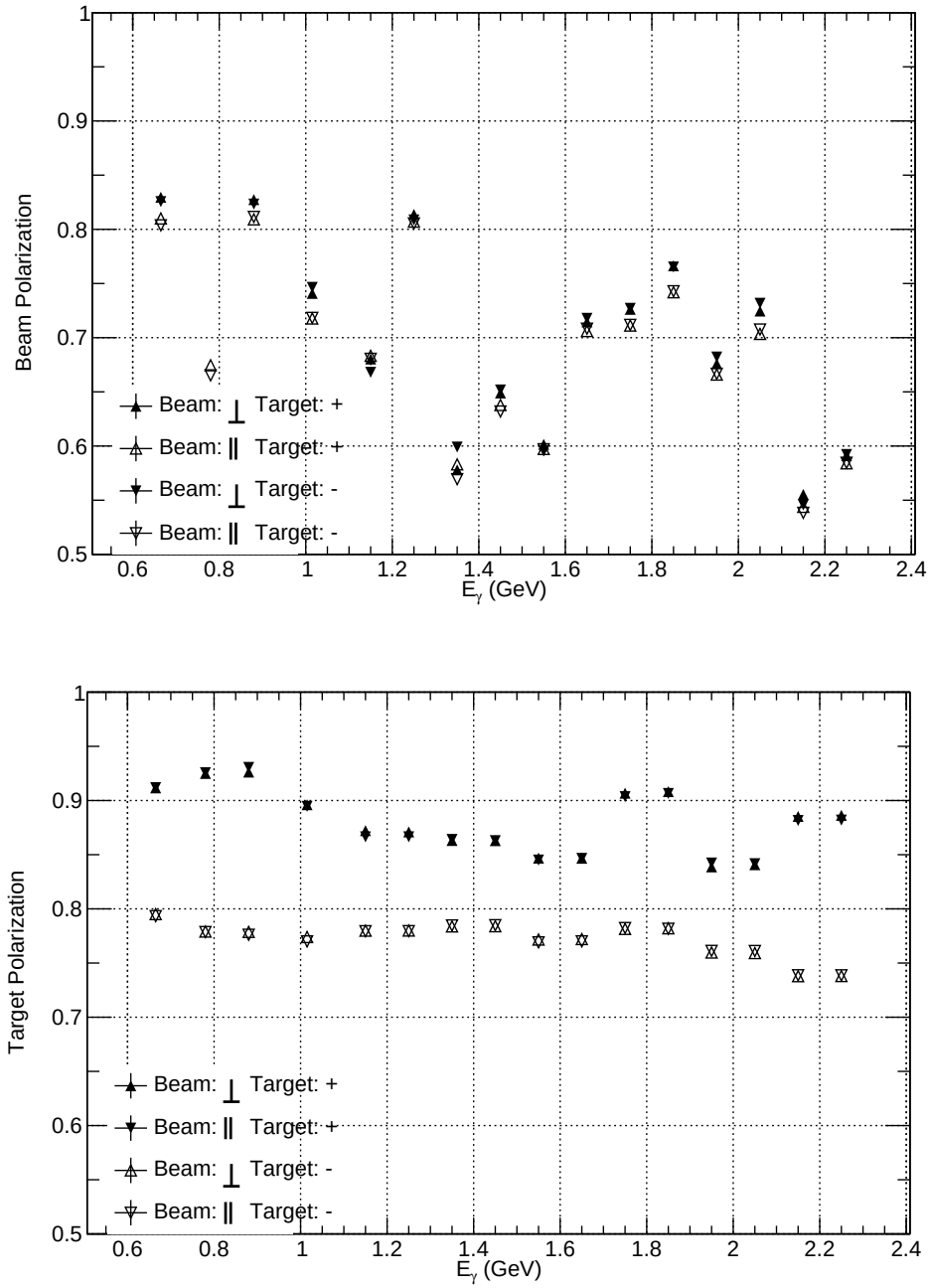

Figure 5.3 The polarization degrees for different polarization configurations. The upper panel shows is the beam polarizations for all four cases and the down panel shows represents the target polarization degrees.

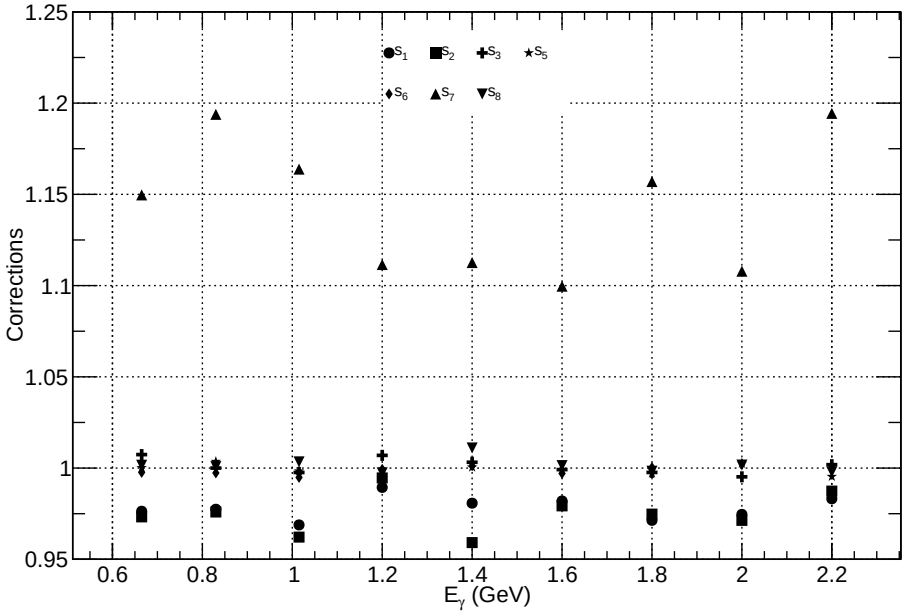

Figure 5.4 The values for the scale factors. Most of the constants are very close to one. However, the constant s_7, which is dominated by the asymmetries between positive and negative target polarization orientations, differs from one significantly.

$$\begin{cases} (s_1\sigma_+^{\perp} - \sigma_+^{\parallel}) - s_3(s_2\sigma_-^{\perp} - \sigma_-^{\parallel}) = \sigma_0 \left\{C_1^a + C_2^a(\sin 2\phi_{lab} P_z^s - \cos 2\phi_{lab} P_z^c)\right\} \\ (s_5\sigma_+^{\perp} + \sigma_+^{\parallel}) - s_8(s_6\sigma_-^{\perp} + \sigma_-^{\parallel}) = \sigma_0 \left\{C_1^c P_z + C_2^c(\sin 2\phi_{lab} P_z^s - \cos 2\phi_{lab} P_z^c)\right\} \\ (s_5\sigma_+^{\perp} + \sigma_+^{\parallel}) + s_7(s_6\sigma_-^{\perp} + \sigma_-^{\parallel}) = \sigma_0 \left\{C_1^d + C_2^d(\sin 2\phi_{lab} P_z^s - \cos 2\phi_{lab} P_z^c)\right\}, \end{cases} \tag{5.15}$$

where the constants C are expressions of the beam and target polarizations. Their experimental values are shown in Fig. 5.5. These values are used in the analysis. To a very good approximation

$$C_1^a \approx C_2^c \approx C_2^d \approx 0, \tag{5.16}$$

$$C_2^a \approx 4\bar{\Lambda}\bar{\delta}, \tag{5.17}$$

$$C_1^c \approx 4\bar{\lambda}, \tag{5.18}$$

$$C_1^d \approx 4, \tag{5.19}$$

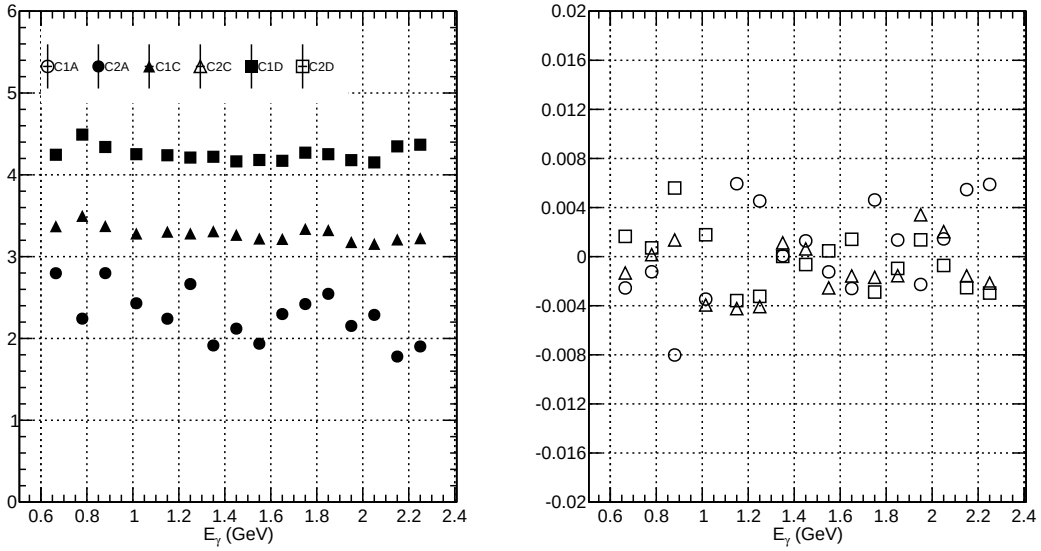

Figure 5.5 Experimental values of the constants C.

where $\bar{\Lambda}$ and $\bar{\delta}$ are the average degrees of the beam and target polarizations, respectively. The constants C_1^a, C_2^c, and C_2^d describe small admixtures to the leading term in the combinations of polarized cross sections, Eq. (5.15). They are typically $< 0.5\%$ and the approximation Eq. (5.16) is used in the analysis. For the other constants the experimental values are used. The cross-section asymmetries are then given by

$$\begin{cases} \dfrac{(s_1\sigma_+^\perp - \sigma_+^\parallel) - s_3(s_2\sigma_-^\perp - \sigma_-^\parallel)}{(s_5\sigma_+^\perp + \sigma_+^\parallel) + s_7(s_6\sigma_-^\perp + \sigma_-^\parallel)} = \dfrac{C_2^a}{C_1^d}(\sin 2\phi_{lab} P_z^s - \cos 2\phi_{lab} P_z^c) \\ \dfrac{(s_5\sigma_+^\perp + \sigma_+^\parallel) - s_8(s_6\sigma_-^\perp + \sigma_-^\parallel)}{(s_5\sigma_+^\perp + \sigma_+^\parallel) + s_7(s_6\sigma_-^\perp + \sigma_-^\parallel)} = \dfrac{C_1^c}{C_1^d} P_z \end{cases} \tag{5.20}$$

5.4 Background subtraction

The derivation of asymmetries Eq. (5.20) in the previous section is based on the assumption of a free polarized proton target without any background. However, in the FROST experiment, the butanol target contains not only the free protons, but also the bound, unpolarized nucleons. The background subtraction is necessary in

order to exclude the effect from bound nucleons. The scale and dilution factors are introduced to estimate the background. Scale factor (denoted as symbol α) is principally the ratio between the number of bound protons in the butanol target and that in the carbon target, while the dilution factor is the ratio of the free-proton yield in the butanol target to the total yield in the butanol target.

The yields from the butanol and carbon targets are the measured quantities of the experiment, from which the asymmetries, the background contribution, and finally the observables are obtained. As discussed earlier, the CLAS acceptance cancels in the yield asymmetries. Table 5.1 gives a set of measurable and derived yields which help to evaluate the background in the following sections.

Table 5.1 Yields from various targets (butanol and carbon) and nuclei (free protons and bound protons).

Symbol	Explanation	Measurable
Y_{But}	Yield of Butanol	Yes
Y_{Car}	Yield of Carbon	Yes
Y_0	Unpolarized Yield from free nuclei in butanol	No
Y_b	Unpolarized Yield from bound nuclei in butanol	No
Y_f	Unpolarized Yield from free protons in carbon	No

Y_{But} and Y_{Car} are the total normalized yields from butanol and carbon targets, respectively, which include the yields from free and bound protons,

$$\begin{cases} Y_{But} = Y_0(1 + \Lambda P_z + \delta[\sin 2\phi_{lab}(I_s + \Lambda P_z^s) - \cos 2\phi_{lab}(I_c + \Lambda P_z^c)]) \\ \qquad\qquad + Y_b(1 + \delta[\sin 2\phi_{lab} I_s' - \cos 2\phi_{lab} I_c']) \\ \alpha Y_{Car} = Y_f(1 + \delta[\sin 2\phi_{lab} I_s - \cos 2\phi_{lab} I_c]) + Y_b(1 + \delta[\sin 2\phi_{lab} I_s' - \cos 2\phi_{lab} I_c']) \end{cases} \tag{5.21}$$

The primed polarization observables are the beam polarization observables for the quasi-free reaction off bound nucleons. After scaling the yield off the carbon target

by the scale factor α, the bound-nucleon yield in Y_{But} matches that in Y_{Car}.

Determination of the scale factor

Both the butanol and carbon targets contain unpolarized bound nucleons. Events off the carbon target were taken as measure of the background from quasi-free production off these nuclei. The side bands in the missing mass distributions are similar in shape for both targets in a given kinematic bin. The fraction of bound-nucleon background in butanol-target events can therefore be estimated by scaling the carbon-target yield to that of butanol to fit the side bands in the missing-mass-square distributions,

$$N_b(MM^2) = \alpha N_c(MM^2) + N_H \exp\left[-\frac{1}{2}\left(\frac{MM^2-\mu}{\sigma}\right)^2\right]. \tag{5.22}$$

The scale factor α and the peak parameters μ, σ, and N_H were fit parameters. The first parameter is α, the coefficient of the missing mass squared for carbon, which represents the scale factor. This factor directly determines the background contribution. The parameters of the Gaussian function, μ and σ, are also important because the missing mass cut range, mentioned above, is determined from these two parameters.

The butanol and scaled carbon missing-mass-squared distributions for each of the four topologies are shown in Fig. 5.6 for the kinematic bin with $W = 1.59$ GeV and $\Phi_{CM} = 285°$. The side bands of both distributions overlap each other. The middle peak is due to events off polarized free hydrogen. The difference of the butanol and scaled carbon missing-mass-squared distributions shows the free proton yield; see Fig. 5.7.

Figure 5.8 shows the scale factors for all the kinematic bins. Each panel shows the ϕ_{CM} distribution of α for a given E_γ bin. Due to acceptance effects, the scale factor is not a constant in the experiment. The butanol target has length around 6 cm, sitting in the center of CLAS detector and carbon target is located 3 cm downstream from the

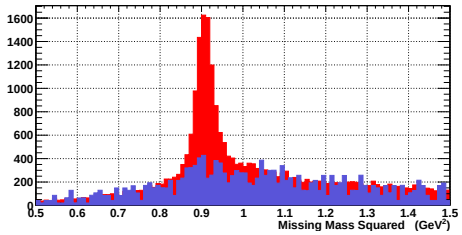

(a) Topology1 – all particles detected

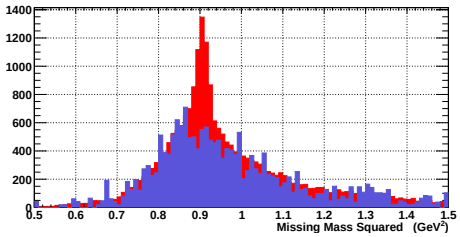

(b) Topology2 – proton undetected

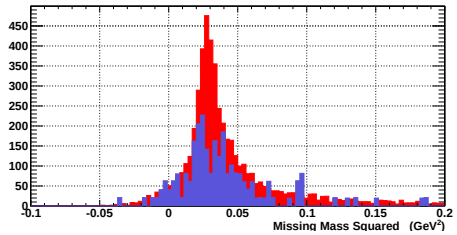

(c) Topology3 – π^+ undetected

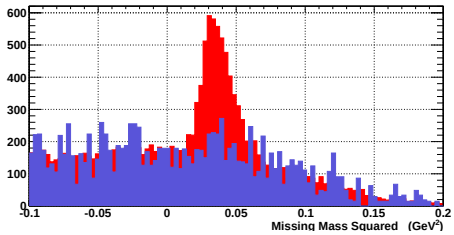

(d) Topology4 – π^- undetected

Figure 5.6 The missing-mass-squared distributions of butanol- (red) and scaled carbon-target (blue) events for the four topologies at $W = 1.59$ GeV and $\Phi_{CM} = 285°$.

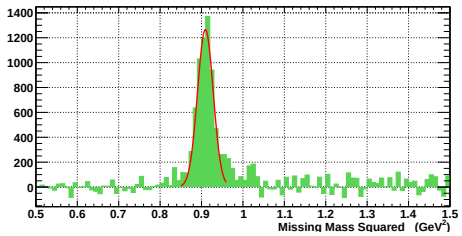

(a) Topology1 – all particles detected

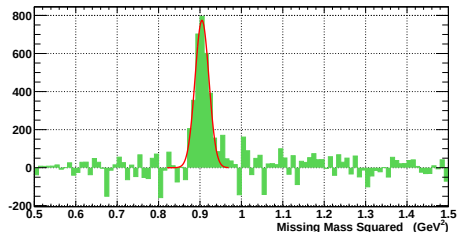

(b) Topology2 – proton undetected

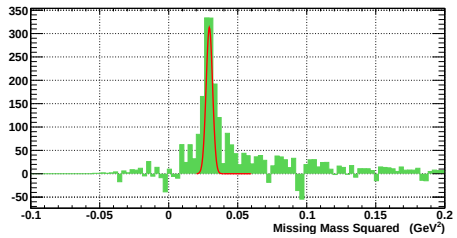

(c) Topology3 – π^+ undetected

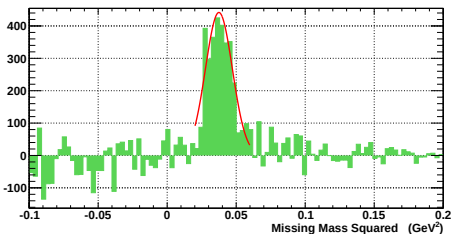

(d) Topology4 – π^- undetected

Figure 5.7 Difference of the butanol and scaled carbon missing-mass-squared distributions for the four topologies at $W = 1.59$ GeV and $\Phi_{CM} = 285°$.

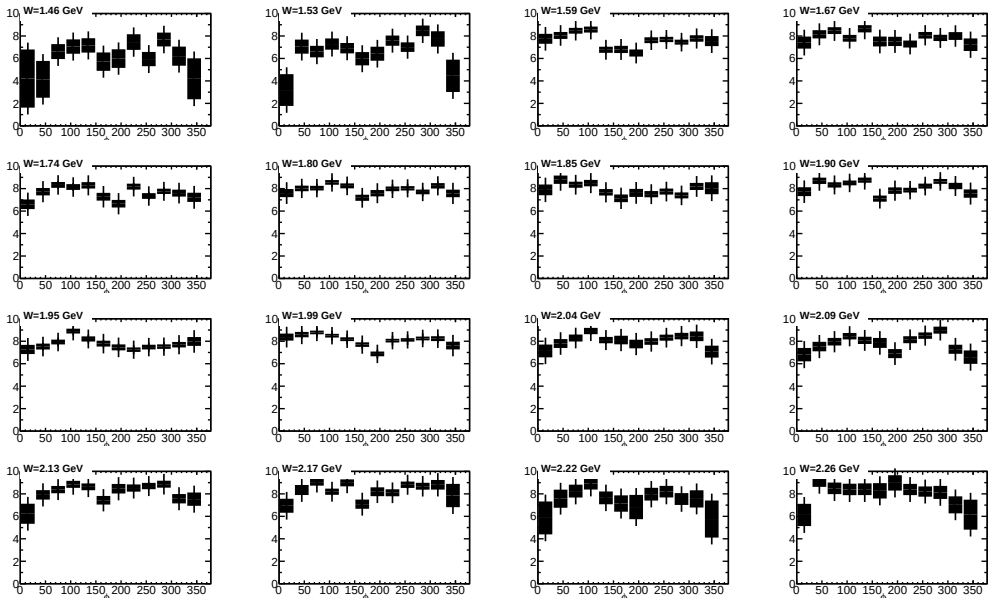

Figure 5.8 The scale factors for all the kinematic bins. Each plot shows one of the energy bins.

center of CLAS. The detector acceptance for butanol-target and carbon-target events and therefore also their relative yield may differ, due to the different target positions. In the analysis, the scale and dilution factors were determined independently for each kinematic bin.

Yield ratio d_1

Similar to the linear combinations of the polarized free-proton cross sections, Eq. (5.15), and with the approximations of Eq. (5.16), the linear combinations of the butanol yields are

$$\begin{cases} (s_1 Y^{\perp}_{+But} - Y^{\parallel}_{+But}) - s_3(s_2 Y^{\perp}_{-But} - Y^{\parallel}_{-But}) = C_2^a Y_0(\sin 2\phi_{lab} P_z^s - \cos 2\phi_{lab} P_z^c) \\ (s_5 Y^{\perp}_{+But} + Y^{\parallel}_{+But}) - s_8(s_6 Y^{\perp}_{-But} + Y^{\parallel}_{-But}) = C_1^c Y_0 P_z \\ (s_5 Y^{\perp}_{+But} + Y^{\parallel}_{+But}) + s_7(s_6 Y^{\perp}_{-But} + Y^{\parallel}_{-But}) = C_1^d (Y_0 + Y_b) \end{cases} \tag{5.23}$$

The bound-nuclear background contributions cancel in the target-polarization differences, the first two equations of Eq. (5.23), they are proportional to the free-proton yield, Y_0. The background contributions contribute in the unpolarized, target-polarization sum, in the last equation. This combination is proportional to the sum of the unpolarized free-proton and background yields, $Y_0 + Y_b$.

The yield asymmetries of the butanol-target events,

$$\begin{cases} \dfrac{(s_1 Y^{\perp}_{+But} - Y^{\parallel}_{+But}) - s_3(s_2 Y^{\perp}_{-But} - Y^{\parallel}_{-But})}{(s_5 Y^{\perp}_{+But} + Y^{\parallel}_{+But}) + s_7(s_6 Y^{\perp}_{-But} + Y^{\parallel}_{-But})} = \dfrac{C_2^a}{C_1^d}\dfrac{Y_0}{Y_0+Y_b}(\sin 2\phi_{lab} P_z^s - \cos 2\phi_{lab} P_z^c) \\ \dfrac{(s_5 Y^{\perp}_{+But} + Y^{\parallel}_{+But}) - s_8(s_6 Y^{\perp}_{-But} + Y^{\parallel}_{-But})}{(s_5 Y^{\perp}_{+But} + Y^{\parallel}_{+But}) + s_7(s_6 Y^{\perp}_{-But} + Y^{\parallel}_{-But})} = \dfrac{C_1^c}{C_1^d}\dfrac{Y_0}{Y_0+Y_b} P_z \end{cases} \tag{5.24}$$

are diluted relative to the free-proton asymmetries, Eq. (5.20), by a factor,

$$h = \frac{Y_0}{Y_0 + Y_b} \tag{5.25}$$

This dilution factor, h, is a measure of how much smaller the yield asymmetry from butanol-target events is compared to the asymmetry from polarized protons due to the background of unpolarized protons in the target.

The ratio of the background-subtracted butanol yield to the total yield off the butanol target,

$$\begin{aligned} d_1 &= 1 - \alpha \, \frac{(s_5 Y^{\perp}_{+Car} + Y^{\parallel}_{+Car}) + s_7(s_6 Y^{\perp}_{-Car} + Y^{\parallel}_{-Car})}{(s_5 Y^{\perp}_{+But} + Y^{\parallel}_{+But}) + s_7(s_6 Y^{\perp}_{-But} + Y^{\parallel}_{-But})} \\ &= \frac{C_1^d(Y_0 + Y_b) - C_1^d(Y_f + Y_b)}{C_1^d(Y_0 + Y_b)} \\ &= \frac{Y_0 - Y_f}{Y_0 + Y_b}, \end{aligned} \tag{5.26}$$

is only approximately equal to the dilution factor due to the contribution of free-proton events from the hydrogen contamination of the carbon target, Y_f. The determination of Y_f is discussed in the following section.

Experimental values of the extracted yield ratio, d_1, are shown in Fig. 5.9 as a function of the lab azimuthal, $\phi_{\rm lab}$. The yield ratio is approximately independent

of ϕ_{lab}. Some more significant deviations from the constant behavior at the highest values of W need to be looked at in a more detailed study.

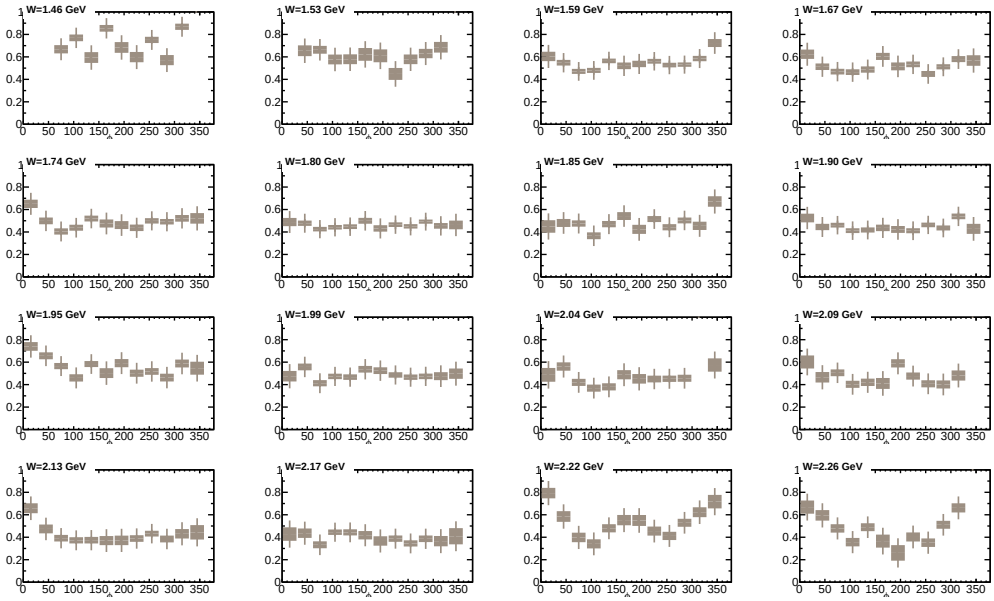

Figure 5.9 The approximate dilution factors, d_1, for all the kinematic bins. Each plot shows one of the energy bin. The average approximate dilution factors are obtained by the constant fit, which can effectively cancel out the impact from observables.

Hydrogen contamination of the carbon target

In the g9a run of the FROST experiment, the downstream side of the carbon target was contaminated with hydrogen. Events from the carbon target are no longer a pure sample of events off bound nuclei. One of the approaches to solve this problem is to cut away the contaminated region in a z-vertex cut. As a consequence a large amount of events would be lost and statistical uncertainties would increase dramatically. Since the contamination is independent of a particular reaction or kinematic bin under study, the yield ratio of events off unpolarized protons in the carbon target, Y_f, to events off polarized protons in butanol target, Y_0,

$$d_2 = \frac{Y_f}{Y_0}, \tag{5.27}$$

is constant for the whole experiment. The ratio is determined by a fit to the bound-nucleon background in the missing-mass-squared distribution. Figure 5.10 illustrates the procedure of the determination of the ratio d_2 for various E_γ bins. The butanol missing-mass distribution is shown in red and the carbon distribution in blue.

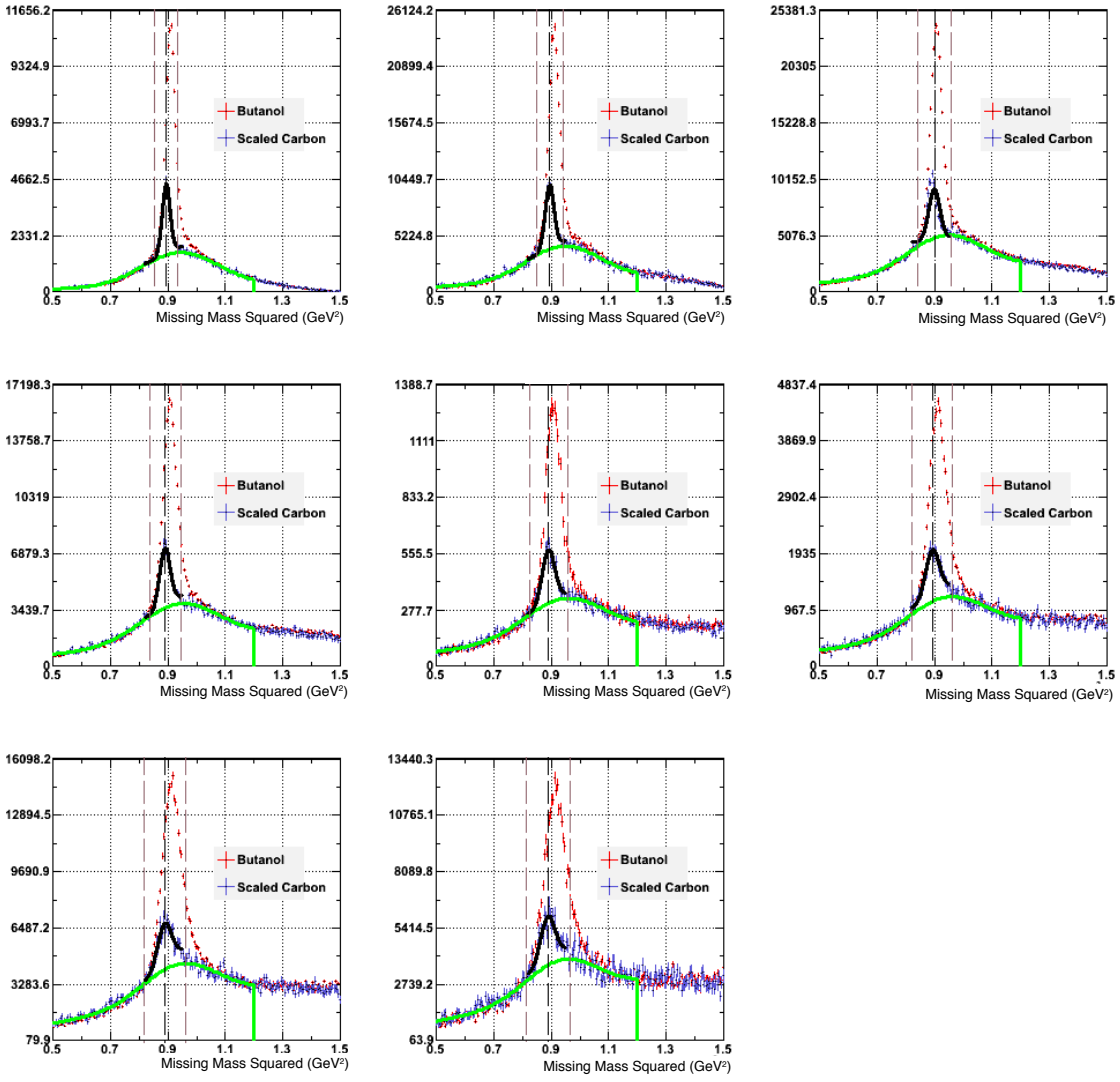

Figure 5.10 The fits to obtain the dilution factor d_2. The red histogram is the missing-mass squared distribution from the butanol target. The blue histogram is the scaled carbon missing-mass squared distribution and the green curve is the fit to the side bands. The eight panels are for eight photon-energy bins.

The missing-mass-squared distributions for both butanol- and carbon-target events

are scaled such that the side bands fit each other. The side bands (excluding a 3σ region around the peak) of the carbon missing-mass-squared distribution were fit with

$$F_{bound} = p_0 e^{-\frac{(MM^2-p_1)^2}{2p_2^2}} + (p_3 + p_4 MM^2), \tag{5.28}$$

reproducing the background shape due to bound nuclei for both butanol and carbon targets. The fits to the sidebands are shown as green curves in Fig. 5.10 and describe the bound-nucleon background. The black curve shows a fit of the carbon missing-mass-squared distribution including the free-proton peak.

The ratio d_2 was then determined from the background subtracted carbon and butanol yields,

$$d_2 = \frac{\sum Y_{Car}(MM^2) - F_{bound}(MM^2)}{\sum Y_{But}(MM^2) - F_{bound}(MM^2)} = \frac{Y_f}{Y_0} \tag{5.29}$$

Figure 5.11 gives the results for eight photon-energy bins. The data were fit with a

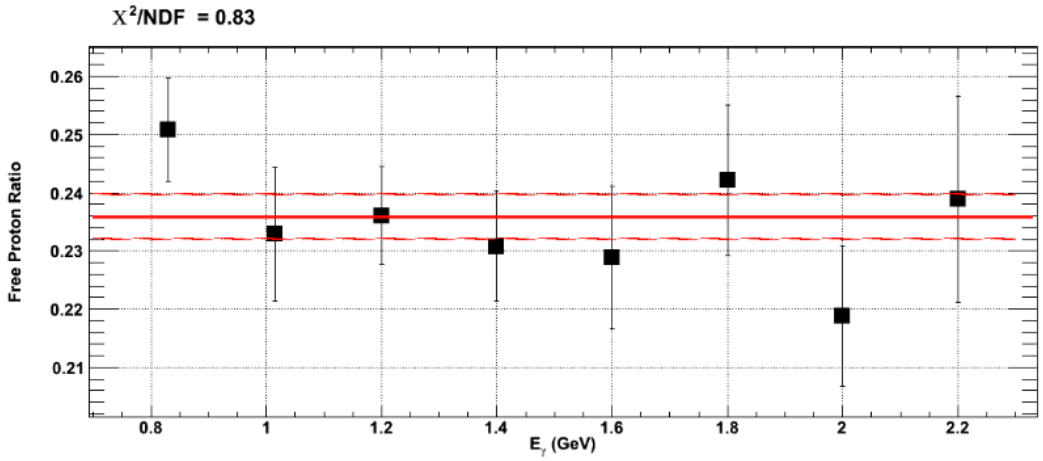

Figure 5.11 The fraction of carbon-to-butanol free-proton yields, d_2. The red line is a constant fit to the d_2 ratio with a χ^2 per degree of freedom of 0.83.

constant to get the mean value and uncertainty of d_2. The normalized χ^2 test shows that the assumption of an energy independent (constant) value of d_2 is justified. The final value of d_2 is determined to be 0.236 ± 0.004. This value is consistent with the value of 0.228 ± 0.011, which was found for the g9a experiment in an analysis of the $\gamma p \to \pi^+ n$ reaction channel [68].

The dilution factor h is finally calculated from the ratios d_1 and d_2,

$$h = \frac{d_1}{1 - d_2} = \frac{Y_0}{Y_0 + Y_b} \tag{5.30}$$

5.5 Extraction of observables

ϕ_0 offset

The ϕ_0 angle is an offset of the actual photon beam-polarization direction from its nominal par and perp directions, due to a mis-alignment of the diamond crystal-lattice plane. It is independent of the coherent edge position and other kinematic variables and needs to be included in the analysis.

The offset cannot be studied in the $\gamma p \to p\pi^+\pi^-$ channel, because the polarized cross section does depend on both the $\sin 2\phi_{lab}$ and $\cos 2\phi_{lab}$ terms. An angular offset in ϕ_{lab} only changes the coefficients of these functions, which are the unknown polarization observables P_z^s and P_z^c. Josephine McAndrew [78] studied the ϕ_0 offset from the linearly polarized g9a data in the $\gamma p \to p\pi^0$ channel with rich statistics. The angular dependence of the polarized yield in the single-pion reaction channel is a function of $\cos 2\phi_{lab}$ only. An offset in ϕ_{lab} appears here as unphysical phase shift. The phase shift can be determined in a fit of the experimental yield asymmetry,

$$\frac{N(\phi_{lab})_\perp - N(\phi_{lab})_\parallel}{N(\phi_{lab})_\perp + N(\phi_{lab})_\parallel} = \delta\Sigma \cos(2(\phi_{lab} - \phi_0)), \tag{5.31}$$

where Σ is the beam-spin asymmetry and δ the degree of photon-beam polarization. Figure 5.12 shows the asymmetry, Eq. (5.31), and the result of the fit with a value of $\phi_0 = 0.21 \pm 0.23^\circ$ for the offset. The value 0.21° was used in this analysis.

The ϕ_0 offset has a $\pm 0.23^\circ$ statistical uncertainty, $\delta\phi_0$, in addition to the 0.21° constant offset. The impact of this uncertainty on the extraction of the double-polarization observables can be seen from the ϕ angular dependence of the polarized

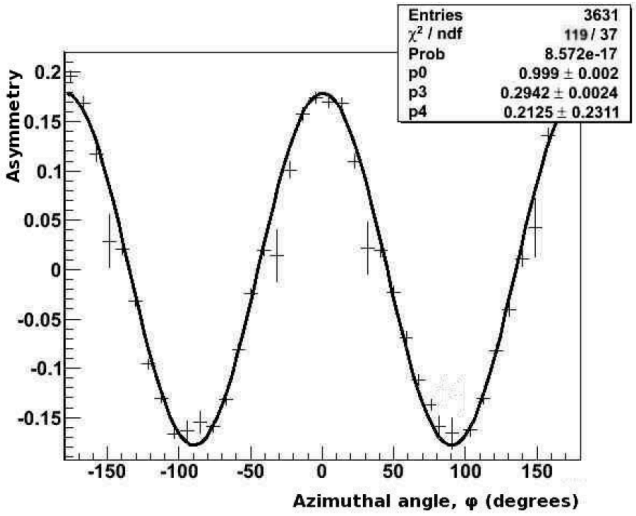

Figure 5.12 Cross-section asymmetry in the $\gamma p \to p\pi^0$ reaction with fit to obtain the systematic ϕ_0 angle. This plot shows the asymmetry and the result of the fit to find angle ϕ_0. The parameter p_4 stands for the offset. Analysis of Ref. [78].

cross section,

$$P_z^s \sin[2(\phi \pm \delta\phi_0)] - P_z^c \cos[2(\phi \pm \delta\phi_0)] \tag{5.32}$$

$$=(P_z^s \cos 2\delta\phi_0 \mp P_z^c \sin 2\delta\phi_0) \sin 2\phi - (P_z^c \cos 2\delta\phi_0 \pm P_z^s \sin 2\delta\phi_0) \cos 2\phi \tag{5.33}$$

$$\approx(P_z^s \mp 2P_z^c \delta\phi_0) \sin 2\phi - (P_z^c \pm 2P_z^s \delta\phi_0) \cos 2\phi \tag{5.34}$$

The relative uncertainties of the double-polarization observables due to the uncertainty in the ϕ_0 offset are therefore of the order $2\delta\phi_0 \approx 0.008$. The double-polarization observables extracted from this analysis have values of less than 0.2; the maximum uncertainty due to ϕ_0 is very small, approximately 0.0016.

Combination of topologies

The analysis of asymmetries and observables are based on a certain topology. However, due to the acceptance of the CLAS detector, a single topology covers only a limited range of the full phase space. Combining all four topologies allows to increase the overall acceptance for this reaction.

Because the determination of the asymmetry is based on the missing mass cut and dilution factors, it is impossible to combine the topologies before the asymmetries constructed; missing-mass-based event selection and dilution factors are different for each topology.

The combined asymmetry, A, is the weighted average of the asymmetries, A_i, of each of the four topologies,

$$A(\beta) = \frac{\sum_{i=1}^{4} w_i A_i(\beta)}{\sum_{i=1}^{4} w_i}, \tag{5.35}$$

where the weights w_i are given by the statistical uncertainties of the asymmetries for each topology, σ_{A_i},

$$w_i = \frac{1}{\sigma_{A_i}^2}. \tag{5.36}$$

The uncertainty of the summed asymmetry is the inverse of the square root of the summed weights w

$$\sigma_A = \frac{1}{\sqrt{\sum_{i=1}^{4} w_i}} \tag{5.37}$$

Figures 5.13 to 5.16 show the β angular distributions of the beam-target yield asymmetries at $W = 1.59$ GeV for 12 Φ_{CM} bins and topologies 1, 2, 3, and 4. Figure 5.17 shows their weighted mean value.

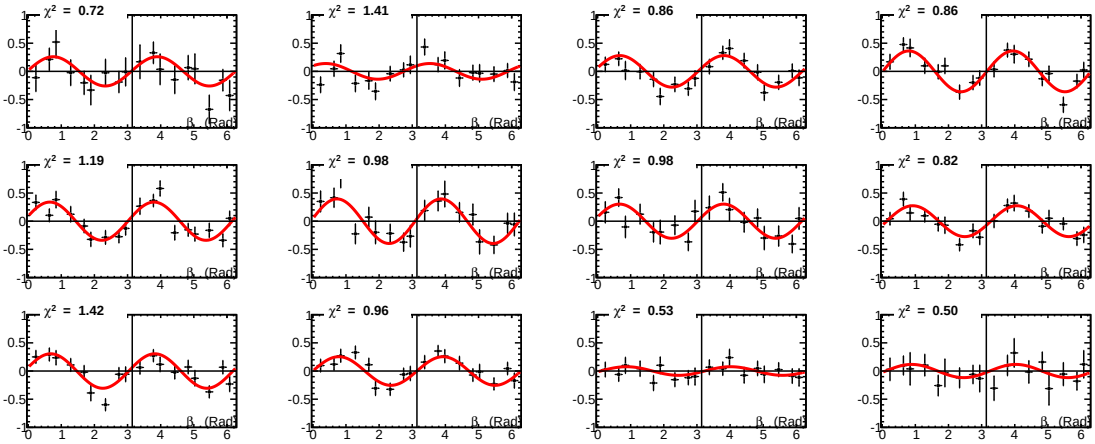

Figure 5.13 Angular distributions of beam-target yield asymmetries for topology 1 (all particles detected) at $W = 1.59$ GeV. Each panel corresponds to a Φ_{CM} bin; $0 \leq \Phi_{CM} \leq 360°$.

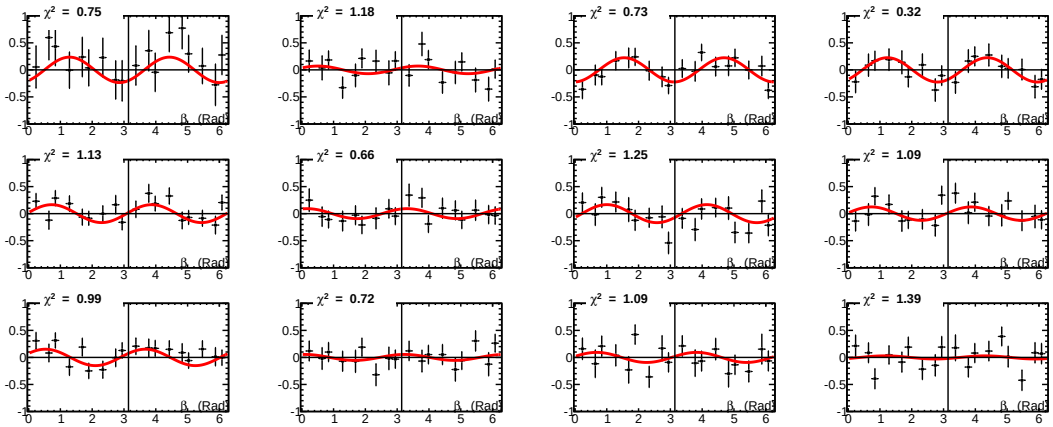

Figure 5.14 Angular distributions of beam-target yield asymmetries for topology 2 (missing proton) at $W = 1.59$ GeV. Each panel corresponds to a Φ_{CM} bin; $0 \leq \Phi_{CM} \leq 360°$.

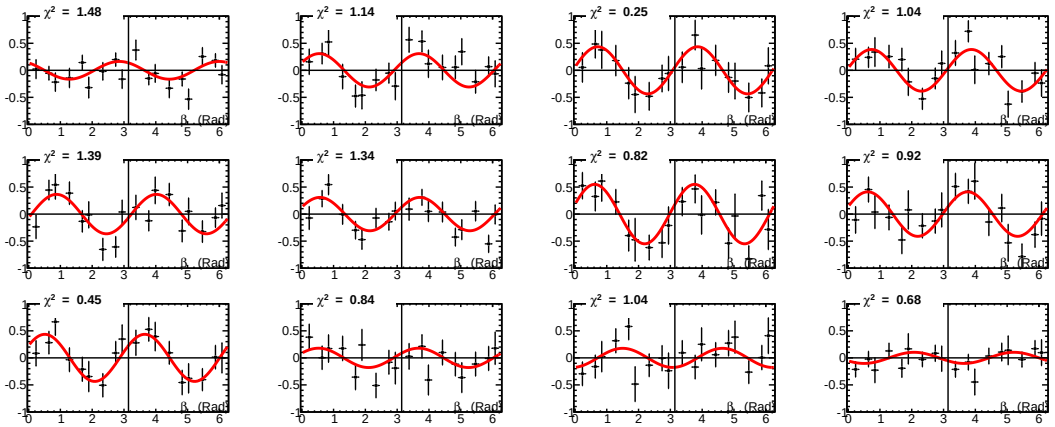

Figure 5.15 Angular distributions of beam-target yield asymmetries for topology 3 (missing π^+) at $W = 1.59$ GeV. Each panel corresponds to a Φ_{CM} bin; $0 \leq \Phi_{CM} \leq 360°$.

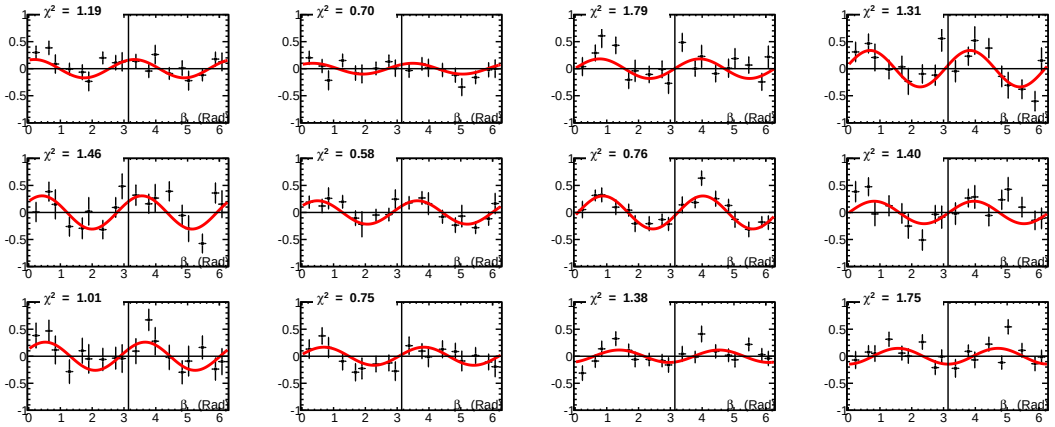

Figure 5.16 Angular distributions of beam-target yield asymmetries for topology 4 (missing π^-) at $W = 1.59$ GeV. Each panel corresponds to a Φ_{CM} bin; $0 \leq \Phi_{CM} \leq 360°$.

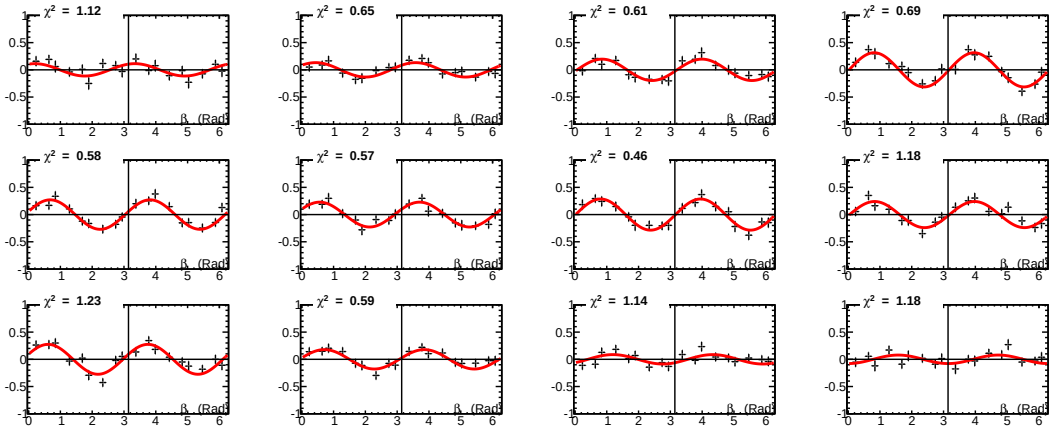

Figure 5.17 Angular distributions of beam-target yield asymmetries for combined data of all four topologies at $W = 1.59$ GeV. Each panel corresponds to a Φ_{CM} bin; $0 \leq \Phi_{CM} \leq 360°$.

Results of extracted observables

Fits to the scaled yield asymmetries were made to extract the single- and double-polarization observables. The fit functions are for the beam-target asymmetries

$$\sin 2\phi_{lab} P_z^s - \cos 2\phi_{lab} P_z^c = \frac{(s_1 Y^{\perp}_{+But} - Y^{\parallel}_{+But}) - s_3(s_2 Y^{\perp}_{-But} - Y^{\parallel}_{-But})}{(s_5 Y^{\perp}_{+But} + Y^{\parallel}_{+But}) + s_7(s_6 Y^{\perp}_{-But} + Y^{\parallel}_{-But})} \frac{C_1^d}{C_2^a} \frac{1}{h} \quad (5.38)$$

and for the target asymmetries

$$P_z = \frac{(s_5 Y^{\perp}_{+But} + Y^{\parallel}_{+But}) - s_8(s_6 Y^{\perp}_{-But} + Y^{\parallel}_{-But})}{(s_5 Y^{\perp}_{+But} + Y^{\parallel}_{+But}) + s_7(s_6 Y^{\perp}_{-But} + Y^{\parallel}_{-But})} \frac{C_1^d}{C_1^c} \frac{1}{h}. \quad (5.39)$$

The asymmetries are scaled by the factors C to account for the degrees of the beam and target polarizations and by the factor $1/h$ to account for the asymmetry dilution due to the bound-nucleon background. The results for the observables P_z^s and P_z^c were also corrected for the effect of the finite bin size $\sin\Delta\phi/\Delta\phi$; see Eq. (5.11). As examples, Fig. 5.18 shows the beam-target and Fig. 5.19 shows target asymmetry curves at $W = 1.59$ GeV. The asymmetries are fit with Eqs. (5.38) and (5.39). The figures give also χ^2 values for each fit. The 12 panels in each figure shows the

asymmetries for a different Φ_{CM} bin; weighted mean of all topologies. The extracted observables, P_z, P_z^s and P_z^c are discussed in the following Chapter.

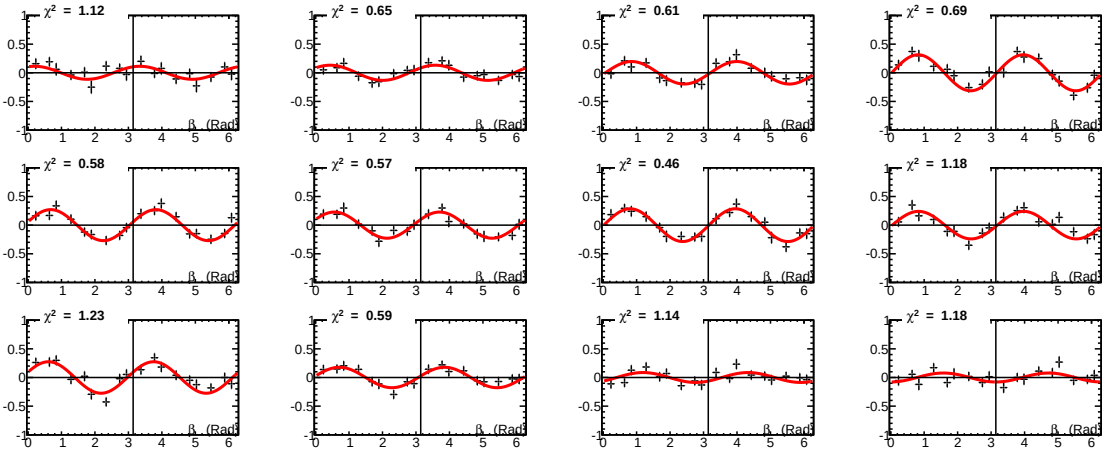

Figure 5.18 The asymmetries for double-polarization observables with W of 1.59 GeV, fitted by the trigonometric function.

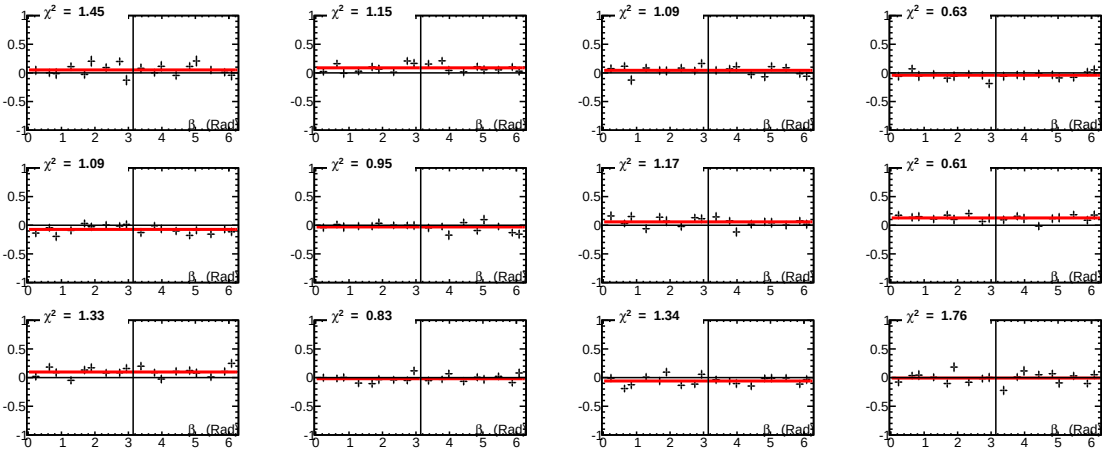

Figure 5.19 The asymmetries for single-polarization observables with W of 1.59 GeV, fitted by a constant value.

The fit quality directly influences the reliability of the final result. Because the fit method used is the minimization of χ^2, the most useful tool to check the quality of the fit is to check the value of the normalized χ^2, which is normalized to the number of degrees of freedom in the fit. The expectation value for the normalized χ^2 value is

one. The left plot of Fig. 5.20 shows the histogram of all the χ^2 from the trigonometric fit and the right plot is that from the constant fit. It is easy to find from the plots that most of the χ^2 are in between 0.5 to 2 and both distributions peak around 1. This means that most of the fits are reliable.

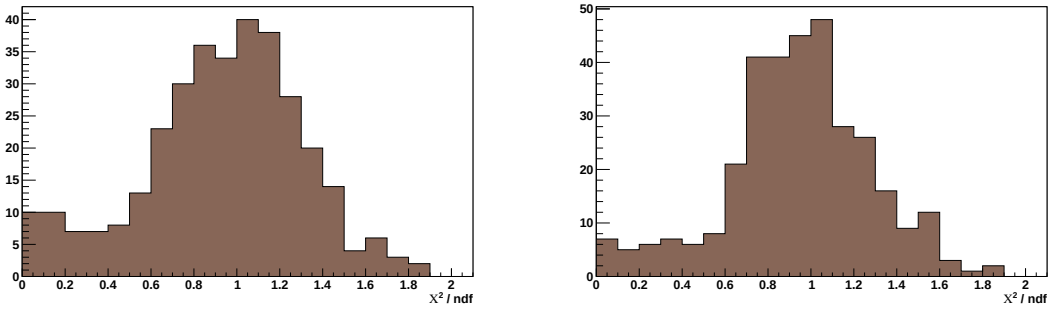

Figure 5.20 The quality of the fit can be reflected by the normalized χ^2. The left plot shows the histogram of all the normalized χ^2 from the trigonometric fit and the right plot is that from the constant fit.

Chapter 6

Results and Discussion

This chapter shows the extracted observables P_z, P_z^s and P_z^c in (W, Φ_{CM}) kinematics bins. The W range 1.46 – 2.25 GeV is covered by 16 bins and the Φ_{CM} range 0° – 360° is covered by 12 bins. Each observable exhibits the expected symmetry property of being either an odd or an even function of Φ_{CM}. Results for an additional binning in invariant mass are also shown and a comparison with model predictions is discussed. These observables, extracted for the first time here, will play an important role to improve the understanding of baryon resonances.

6.1 Results for polarization observables

Two typical examples of the polarization observables P_z, P_z^s, and P_z^c extracted in this work, are shown in Fig. 6.1 and Fig. 6.2, for $W = 1.59$ GeV and for $W = 1.67$ GeV, respectively. Parity conservation in the nuclear reaction implies that each observable is either odd or even under the transformation $\Phi_{CM} \rightarrow 2\pi - \Phi_{CM}$ [52]. Parity conservation also implies that the odd observables should vanish for $\Phi_{CM} = 0°$ and $\Phi_{CM} = 180°$, when all particles are coplanar. Visual analysis of the distributions in Fig. 6.2 suggests that P_z and P_z^c are odd functions of Φ_{CM} while P_z^s is an even function. To quantify the level of consistency between the experimental estimates and the expectations, $P_z(\Phi_{CM})$ and $P_z^c(\Phi_{CM})$ were each fitted to a series of sine functions, while $P_z^s(\Phi_{CM})$ was fitted to a series of cosine functions

$$P_z(\Phi_{CM}), P_z^c(\Phi_{CM}) = p_1 \sin(\Phi_{CM}) + p_2 \sin(2\Phi_{CM}) + p_3 \sin(3\Phi_{CM}) + p_4 \sin(4\Phi_{CM}), \tag{6.1}$$

$$P_z^s(\Phi_{CM}) = p_0 + p_1\cos(\Phi_{CM}) + p_2\cos(2\Phi_{CM}) + p_3\cos(3\Phi_{CM}) + p_4\cos(4\Phi_{CM}). \quad (6.2)$$

Terms up to 4^{th} order were kept in the fits, based on previous studies of this reaction [44]. The solid lines in Fig. 6.1 and Fig. 6.2 show the fits. To demonstrate the quality of the fits we quote in the figures the normalized χ^2, which ranges from 0.73 to 3.26. The extracted distributions have the symmetry properties implied by parity conservation, which supports the reliability of our analysis.

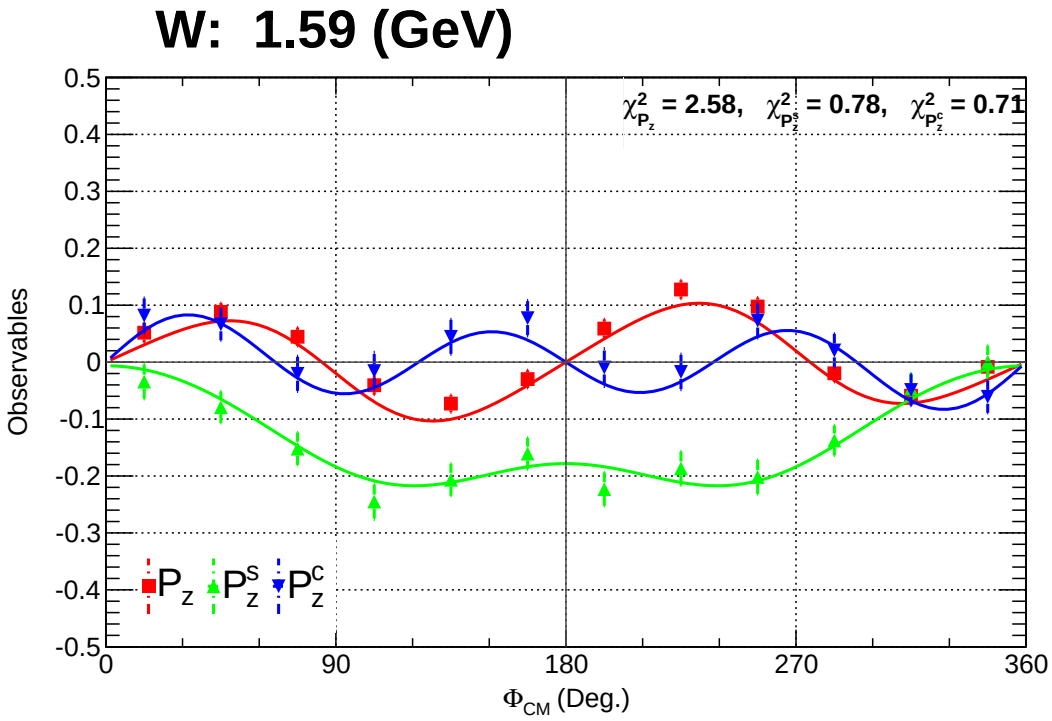

Figure 6.1 Example azimuthal distributions of the single-polarization observable P_z and double-polarization observables P_z^c and P_z^s for $W = 1.59$ GeV. The solid lines show fits with sine (to P_z and P_z^c) and cosine (to P_z^s) functions. To demonstrate the fit quality, the normalized χ^2 are reported. The relatively large χ^2 value of 3.26 is for the fit to the observable with the very small statistical uncertainties (smaller than the symbol size) and may be a signature that the bin-to-bin systematic uncertainties (not included in the error bars) are not negligible. The experimental estimates exhibit the symmetry properties expected from parity conservation.

The estimates of the observables P_z, P_z^s and P_z^c for all kinematic bins are shown in Fig. 6.3, Fig. 6.4, and Fig. 6.5, respectively. The observables are shown as a function of Φ_{CM} for fixed W.

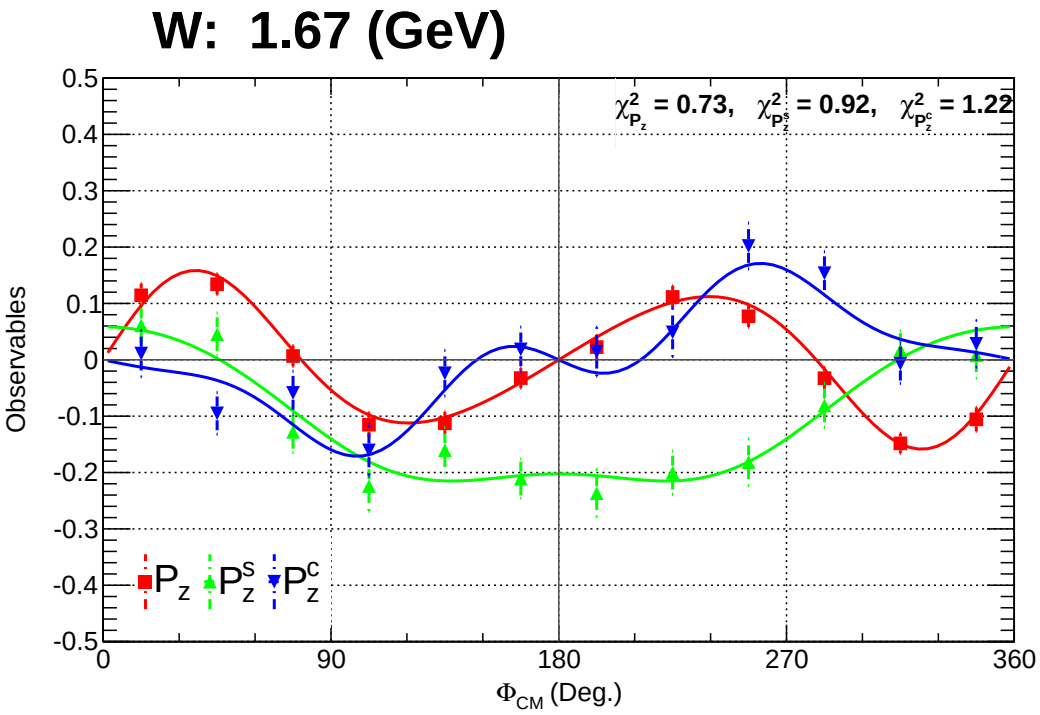

Figure 6.2 Example azimuthal distributions of the single-polarization observable P_z and double-polarization observables P_z^c and P_z^s for $W = 1.67$ GeV. The solid lines show fits with sine (to P_z and P_z^c) and cosine (to P_z^s) functions. To demonstrate the fit quality, the normalized χ^2 are reported. The experimental estimates exhibit the symmetry properties expected from parity conservation.

The amplitude of the extracted observables is relatively small, typically less than 0.25. The largest amplitudes and the richest structures of $P_z(\Phi_{CM})$ and $P_z^s(\Phi_{CM})$ are observed at the lowest center-of-mass energies. The variation of the amplitude of $P_z^c(\Phi_{CM})$ with W is more complex. This observable shows significantly non-zero amplitudes not only at some low and mid center-of-mass energies, but also at the two highest W bins. The full information about the kinematic evolution of the observables can be obtained by extracting estimates in 5-dimensional kinematic bins. However, the statistics collected in g9a does not allow for such a fine binning.

The data are compared with model predictions of Fix and Arenhövel, Ref. [26]. The model values are experimental-yield-weighted mean values of the theoretical results for each kinematic bin. In this way the finite acceptance of the CLAS detector

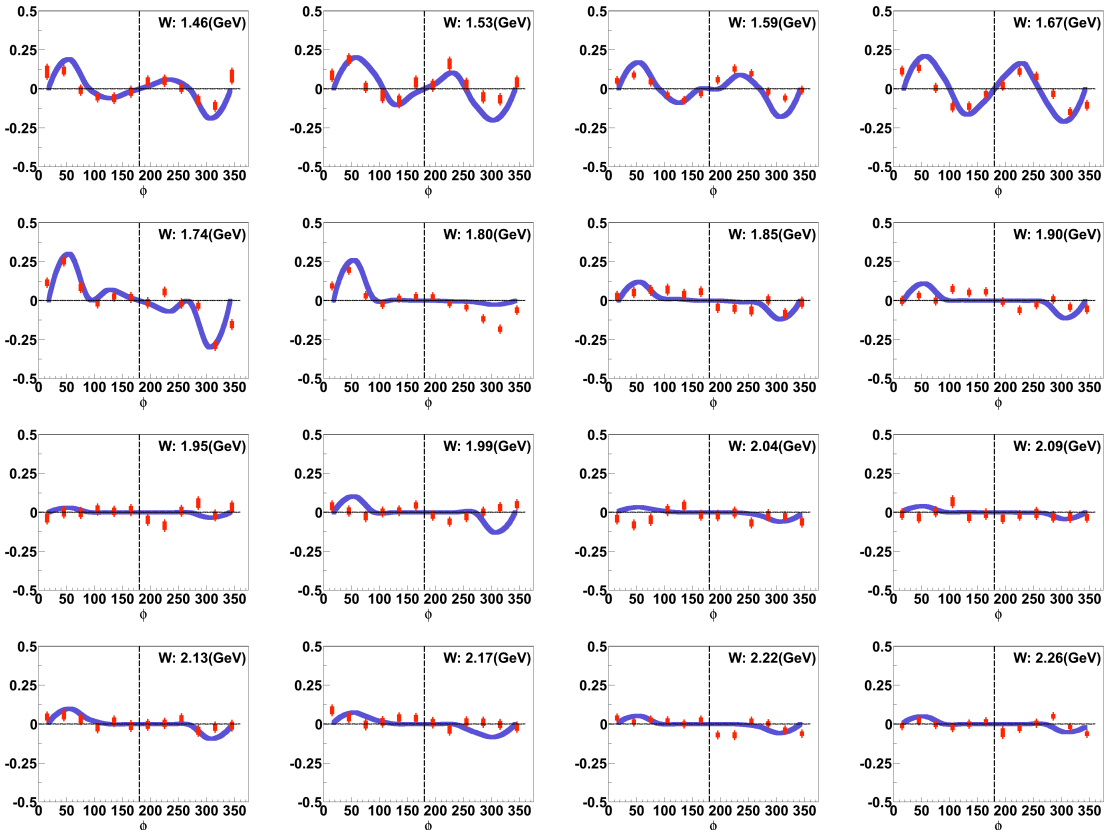

Figure 6.3 Experimental Φ_{CM} distributions of the single-polarization observable P_z for various center-of-mass energies. The error bars indicate the statistical uncertainties only. The solid line is the model prediction of [26].

is taken into account in the comparison. The model describes basic features of the observables well, but not some of the details in the distributions.

Given the sensitivity of the observables to intermediate-resonance excitation, physics interpretation of the reported results requires comparison with a theoretical model or/and incorporation in partial-wave or coupled-channel analyses.

6.2 Sensitivity of observables to two-particle invariant mass

In view of the general objective of this work to make a contribution to the study of baryon resonances, the investigation of the dependence of the polarization observables on the invariant mass, IM, of a pair of final-state particles has a special importance.

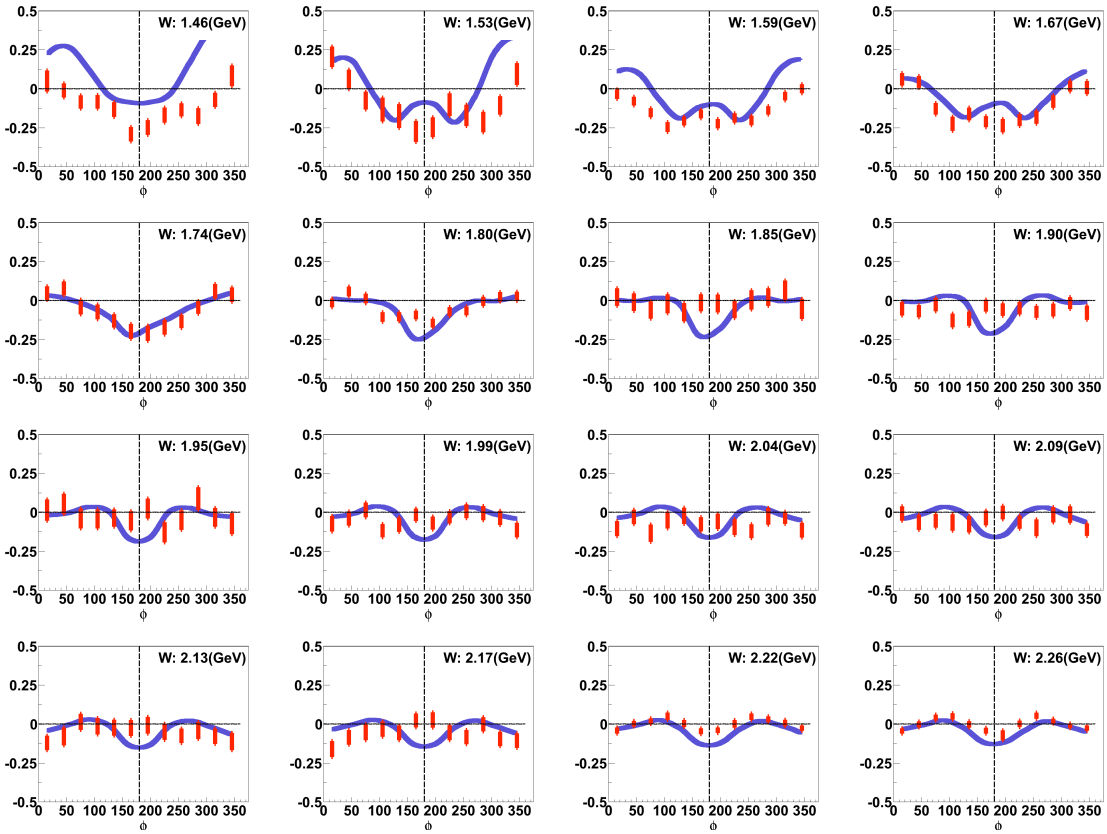

Figure 6.4 Experimental Φ_{CM} distributions of the double-polarization observable P_z^s for various center-of-mass energies. The error bars indicate the statistical uncertainties only. The solid line is the model prediction of [26].

This is due to the fact, that the shape of the invariant-mass event distribution is directly related to the properties of excited resonance states. A typical example is the event distribution over $IM^2_{p\pi^+}$ (shown in Fig. 6.6), where one can clearly identify a peak positioned at the mass-squared of Δ^{++}. Other intermediate resonances, such as ρ, which can lead to the $p\pi^+\pi^-$ final state, also contribute to the invariant-mass distributions. While very few resonances decaying to πN can be visually identified as peaks in the invariant mass distribution of their decay particles, by selecting a certain range in invariant mass, one can suppress events from certain reaction mechanisms and enhance the contribution of others. To demonstrate the sensitivity of the observables to the invariant mass of pairs of final-state particles, $P_z(\Phi_{CM})$, $P_z^s(\Phi_{CM})$, and

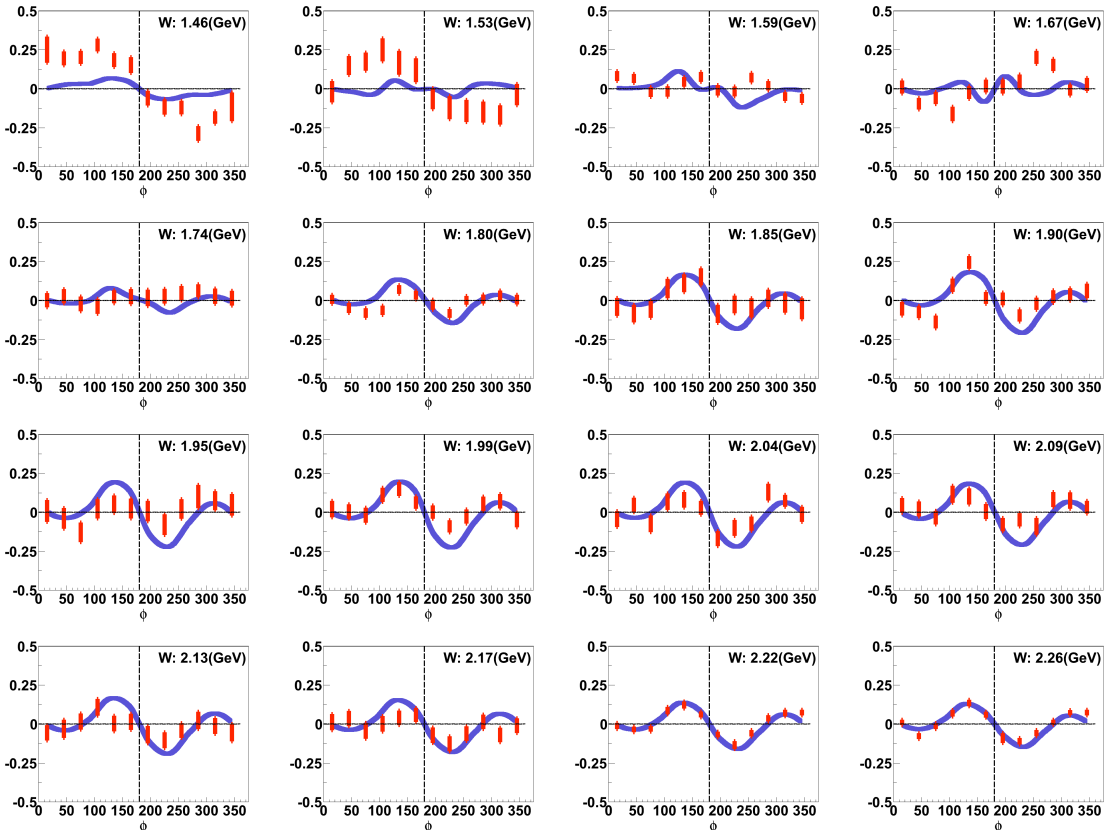

Figure 6.5 Experimental Φ_{CM} distributions of the double-polarization observable P_z^c for various center-of-mass energies. The error bars indicate the statistical uncertainties only. The solid line is the model prediction of [26].

$P_z^c(\Phi_{CM})$ are extracted in a bin of $IM^2_{p\pi^+}$ from 1.2 to 1.8 GeV^2. In this mass-squared range the contribution from intermediate Δ^{++} is enhanced, while contributions from ρ or Δ^0 are suppressed. Figure 6.7 shows the observables for $W = 1.85$ GeV without and with the additional binning in $IM^2_{p\pi^+}$.

The binning in the third kinematic variable does not affect the symmetry properties of the observables. However, the amplitudes of the observables are clearly enlarged. Further estimates of the observables in other $IM^2_{p\pi^+}$ or in bins of $IM^2_{p\pi^-}$ and $IM^2_{\pi^+\pi^+}$ will be very valuable for the study of baryon resonances in a specific mass range.

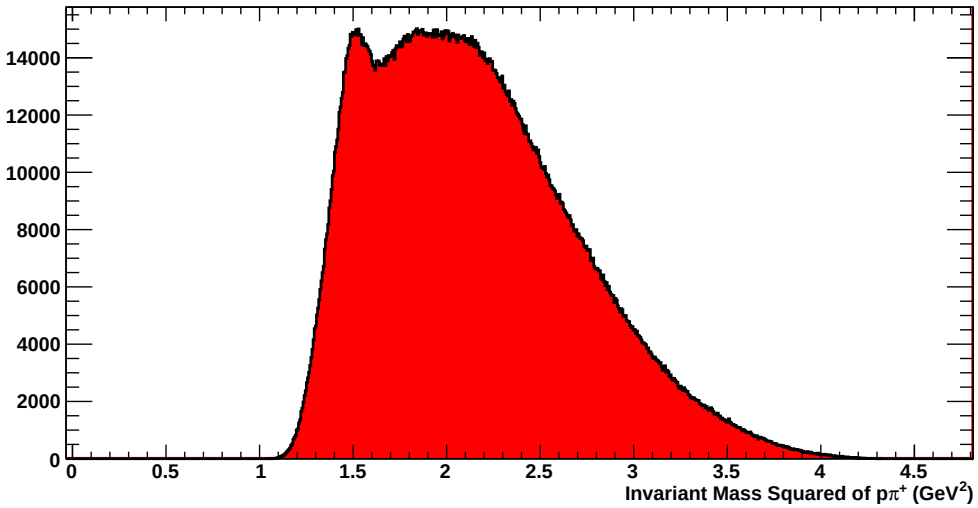

Figure 6.6 Proton-π^+ invariant-mass-squared ($IM^2_{p\pi^+}$) distribution for center-of-mass energy of 1.85 GeV^2. One can clearly see the peak due to intermediate Δ^{++} resonance. To suppress contributions from non-Δ^{++} mechanisms, the observables are extracted in $IM^2_{p\pi^+}$ bin ranging from 1.2 GeV^2 to 1.8 GeV^2.

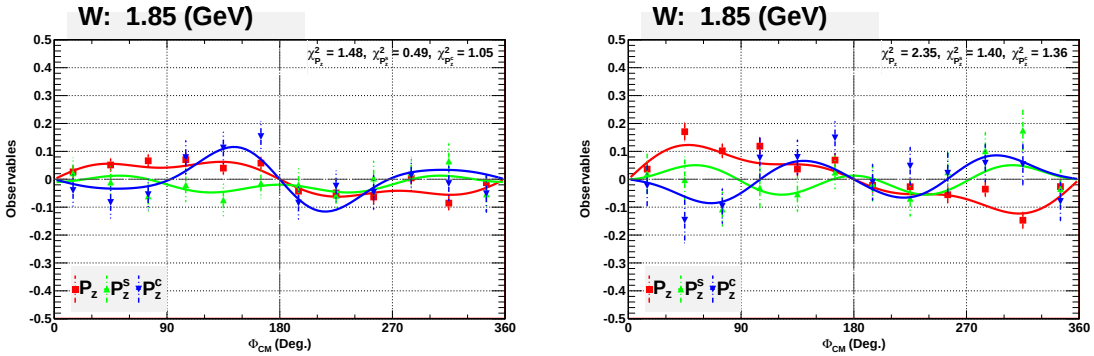

Figure 6.7 Left: Extracted observables for $W = 1.85$ GeV^2, integrated over the entire $IM^2_{p\pi^+}$ range. Right: Extracted observables for $W = 1.85$ GeV^2 and $IM^2_{p\pi^+} \in [1.2, 1.8]$ GeV^2. One can clearly see that the selection of this invariant-mass-squared range enhances the amplitudes of the observables. This demonstrates the sensitivity of the polarization observables to the underlying reaction mechanisms.

6.3 Discussion and outlook

This analysis estimated the polarization observables P_z, P^s_z, and P^c_z in a W range from 1.46 GeV to 2.25 GeV and in the full range of the angle Φ_{CM} between the scattering and double-pion planes. The observables were extracted from the normalized yields

by the construction of various yield asymmetries. The single-polarization observable P_z was extracted by means of a linear fit to the target asymmetry, Eq. (5.39), while the double-polarization observables were extracted by means of a trigonometric-functions fit to the beam-target asymmetry, Eq. (5.38). The fit quality was monitored by the χ^2 distribution of the fits. The χ^2 of all the fits were in in range from 0.5 to 2, indicating the reliability of the observables extracted. The observables from experimental data were compared with experimental-yield-weighted model predictions. The comparison shows that the measured observables will help constrain the model and the model parameters.

This work presented the initial extraction of the polarization observables P_z, P_z^s, and P_z^c. More studies need to be done in the future. First, the dependence of the polarization observables on the kinematics of the reaction can be studied in more detail. Cuts on kinematic variables other than Φ_{CM}, like invariant masses $m(p\pi^+)$ or $m(\pi^+\pi^-)$, can help study various decay channels and constrain reaction mechanisms.

Second, the observable extraction is based on binned angular distributions and the minimization of χ^2. Information is lost in the binning and the necessary integration over unspecified kinematic variables. An alternative is an unbinned maximum likelihood analysis. However, these analysis are complex and require the knowledge of the background or dilution factor for each event.

Finally, the FROST experiment has measured the $\gamma p \to p\pi^+\pi^-$ reaction channel with linearly polarized photons and longitudinally polarized target (this work), but also with circularly polarized photon and transversally polarized target. Multiple analyses have been conducted or are underway, which will result in a large set of new single- and double-polarization observables. Some of these observables are connected through inequality relations; see [52]. Different combinations of amplitudes contribute to the polarization observables. The amplitudes and phases of the amplitudes of the reaction could be strongly constrained by the set of new observables.

Bibliography

[1] V. Credé and W. Roberts, Rept.Prog.Phys. **76** (2013) 076301, 1302.7299.

[2] K. Olive *et al.*, Chin.Phys. **C38** (2014) 090001.

[3] D. Griffiths, *Introduction to elementary particles*, Wiley. com (2008).

[4] Löring, Ulrich and Metsch, Bernard C. and Petry, Herbert R., Eur.Phys.J. **A10** (2001) 395, hep-ph/0103289.

[5] R. Koniuk and N. Isgur, Phys.Rev.Lett. **44** (1980) 845.

[6] R. Arndt, W. Briscoe, I. Strakovsky, and R. Workman, Phys.Rev. **C74** (2006) 045205, nucl-th/0605082.

[7] B. Krusche, The European Physical Journal Special Topics **198** (2011) 199.

[8] J. Ahrens *et al.*, Physics Letters B **624** (2005) 173 .

[9] B. Krusche and S. Schadmand, Progress in Particle and Nuclear Physics **51** (2003) 399.

[10] R. Horgan and R. Dalitz, Nuclear Physics B **66** (1973) 135 .

[11] M. K. Gaillard, B. W. Lee, and J. L. Rosner, Reviews of Modern Physics **47** (1975) 277.

[12] P. Sauer, Czechoslovak Journal of Physics B **36** (1986) 278.

[13] K. Liu and C. Wong, Physical Review D **28** (1983) 170.

[14] E. Santopinto, Phys.Rev. **C72** (2005) 022201, hep-ph/0412319.

[15] S. Fleck, B. Silvestre-Brac, and J. Richard, Physical Review D **38** (1988) 1519.

[16] N. Isgur and J. Paton, Physical Review D **31** (1985) 2910.

[17] A. Casher, H. Neuberger, and S. Nussinov, Physical Review D **20** (1979) 179.

[18] N. Isgur and G. Karl, Phys. Rev. D **18** (1978) 4187.

[19] N. Isgur and G. Karl, Phys. Rev. D **19** (1979) 2653.

[20] S. Capstick and N. Isgur, Phys. Rev. D **34** (1986) 2809.

[21] L. Y. Glozman and D. O. Riska, Physics Reports **268** (1996) 263.

[22] K. F. Liu, S. J. Dong, T. Draper, D. Leinweber, J. Sloan, W. Wilcox, and R. M. Woloshyn, Phys. Rev. D **59** (1999) 112001.

[23] Z. Li and F. E. Close, Phys. Rev. D **42** (1990) 2207.

[24] S. Capstick, Phys. Rev. D **46** (1992) 1965.

[25] I. Aznauryan *et al.*, Phys.Rev. **C78** (2008) 045209, 0804.0447.

[26] A. Fix and H. Arenhövel, The European Physical Journal A - Hadrons and Nuclei **25** (2005) 115.

[27] A. Braghieri, L. Murphy, J. Ahrens, G. Audit, N. d'Hose, V. Isbert, S. Kerhoas, M. Mac Cormick, P. Pedroni, T. Pinelli, *et al.*, Physics Letters B **363** (1995) 46.

[28] M. Hirata, K. Ochi, and T. Takaki, Arxiv preprint nucl-th/9711031 .

[29] H. Kamano, arXiv preprint arXiv:1001.5080 .

[30] B. Julia-Diaz, T.-S. Lee, A. Matsuyama, T. Sato, and L. Smith, Physical Review C **77** (2008) 045205.

[31] A. Matsuyama, T. Sato, and T.-S. Lee, Physics reports **439** (2007) 193.

[32] A.-B.-B.-H.-H.-M. Collaboration, Phys.Rev. **175** (1968) 1669.

[33] E. Klempt, A. Anisovich, V. Nikonov, A. Sarantsev, and U. Thoma, Eur.Phys.J. **A29** (2006) 307.

[34] A. Anisovich, E. Klempt, A. Sarantsev, and U. Thoma, Eur.Phys.J. **A24** (2005) 111, hep-ph/0407211.

[35] A. Anisovich and A. Sarantsev, Eur.Phys.J. **A30** (2006) 427, hep-ph/0605135.

[36] A. Sarantsev, M. Fuchs, M. Kotulla, U. Thoma, J. Ahrens, *et al.*, Phys.Lett. **B659** (2008) 94, 0707.3591.

[37] A. Anisovich, R. Beck, E. Klempt, V. Nikonov, A. Sarantsev, *et al.*, Eur.Phys.J. **A48** (2012) 15, 1112.4937.

[38] Y. Assafiri, O. Bartalini, V. Bellini, J. Bocquet, S. Bouchigny, *et al.*, Phys.Rev.Lett. **90** (2003) 222001.

[39] U. Thoma, M. Fuchs, A. Anisovich, G. Anton, R. Bantes, *et al.*, Phys.Lett. **B659** (2008) 87, 0707.3592.

[40] J. Ahrens *et al.*, Phys.Lett. **B624** (2005) 173.

[41] S. Schumann, B. Boillat, E. Downie, P. Aguar-Bartolome, J. Ahrens, *et al.*, Eur.Phys.J. **A43** (2010) 269, 1001.3626.

[42] V. Kashevarov, A. Fix, S. Prakhov, P. Aguar-Bartolome, J. Annand, *et al.*, Phys.Rev. **C85** (2012) 064610, 1204.4058.

[43] F. Zehr, *Double pion photoproduction off the proton at threshold and in the second resonance region*, Ph.D. thesis, University of Basel (2010).

[44] S. Strauch *et al.*, Phys. Rev. Lett. **95** (2005) 162003.

[45] V. I. Mokeev *et al.*, Yad. Fiz. **64** (2001) 1368, [Phys. At. Nucl. **64**, 1292 (2001)].

[46] V. Burkert *et al.*, Nucl. Phys. **A737** (2004) S231.

[47] V. I. Mokeev *et al.*, Proc. NSTAR2004 (World Scientific, New Jersey, 2004), p. 321.

[48] D. Krambrich *et al.*, Phys.Rev.Lett. **103** (2009) 052002, 0907.0358.

[49] F. Zehr, B. Krusche, P. Aguar, J. Ahrens, J. Annand, *et al.*, Eur.Phys.J. **A48** (2012) 98, 1207.2361.

[50] M. Oberle, B. Krusche, J. Ahrens, J. Annand, H. Arends, *et al.*, Phys.Lett. **B721** (2013) 237, 1304.1919.

[51] L. Roca, Nuclear Physics A **748** (2005) 192 .

[52] W. Roberts and T. Oed, Phys.Rev. **C71** (2005) 055201, nucl-th/0410012.

[53] S. Strauch, AIP Conf.Proc. **1432** (2012) 283, 1108.3050.

[54] C. Hanretty, AIP Conf.Proc. **1432** (2012) 397.

[55] V. Sokhoyan, AIP Conf.Proc. **1432** (2012) 405, 1108.5283.

[56] Jefferson Lab Experiment E06-013, "Measurement of $\pi^+\pi^-$ Photoproduction in Double-Polarization Experiments using CLAS", M. Bellis, V. Credé, S. Strauch, spokespersons.

[57] C. W. Leemann, D. R. Douglas, and G. A. Krafft, Annual Review of Nuclear and Particle Science **51** (2001) 413, http://www.annualreviews.org/doi/pdf/10.1146/annurev.nucl.51.101701.132327.

[58] F. Rambo, J. Ahrens, H.-J. Arends, R. Beck, G. Galler, J. D. Kellie, H.-P. Krahn, A. Kraus, U. Ludwig, J. Peise, A. Schmidt, M. Schumacher, F. Smend, F. Wissmann, and S. Wolf, Phys. Rev. C **58** (1998) 489.

[59] K. Livingston, Nuclear Instruments and Methods in Physics Research Section A: Accelerators, Spectrometers, Detectors and Associated Equipment **603** (2009) 205 .

[60] F. Klein *et al.*, The Coherent Bremsstrahlung Facility in Hall B at Jefferson Lab, unpublished (2005).

[61] K. Livingston, Polarization from Coherent Bremsstrahlung Enhancement, CLAS Note 2011-020 (2011).

[62] N. Zachariou, Determination of the Azimuthal Asymmetry of Deuteron Photodisintegration in the Energy Region $E_\gamma = 1.1 - 2.3$ GeV, Ph.D. Dissertation, The George Washington University (2012).

[63] D. Sober *et al.*, Nuclear Instruments and Methods in Physics Research Section A: Accelerators, Spectrometers, Detectors and Associated Equipment **440** (2000) 263 .

[64] M. Anderson, `https://clasweb.jlab.org/rungroups/g9/wiki/index.php/Linear_Polarization_tables`.

[65] M. Dugger, Consistency corrections to the linear photon polarization for g8b data, Technical report, Arizona State University (2012).

[66] C. Keith, J. Brock, C. Carlin, S. Comer, D. Kashy, J. McAndrew, D. Meekins, E. Pasyuk, J. Pierce, and M. Seely, Nuclear Instruments and Methods in Physics Research Section A: Accelerators, Spectrometers, Detectors and Associated Equipment **684** (2012) 27.

[67] C. Keith *et al.*, Nuclear Instruments and Methods in Physics Research Section A: Accelerators, Spectrometers, Detectors and Associated Equipment **501** (2003) 327 .

[68] S. Strauch, "Polarization Observable E in the $\vec{p}(\vec{\gamma},\pi^+)n$ Reaction", CLAS-ANALYSIS 2014-101 (unpublished).

[69] B. Mecking *et al.*, Nuclear Instruments and Methods in Physics Research Section A: Accelerators, Spectrometers, Detectors and Associated Equipment **503** (2003) 513 .

[70] Y. Sharabian *et al.*, Nuclear Instruments and Methods in Physics Research Section A: Accelerators, Spectrometers, Detectors and Associated Equipment **556** (2006) 246 .

[71] M. Mestayer *et al.*, Nuclear Instruments and Methods in Physics Research Section A: Accelerators, Spectrometers, Detectors and Associated Equipment **449** (2000) 81 .

[72] M. Anghinolfi *et al.*, Nuclear Instruments and Methods in Physics Research Section A: Accelerators, Spectrometers, Detectors and Associated Equipment **537** (2005) 562 .

[73] M. Amarian *et al.*, Nuclear Instruments and Methods in Physics Research Section A: Accelerators, Spectrometers, Detectors and Associated Equipment **460** (2001) 239 .

[74] E. Smith, T. Carstens, J. Distelbrink, M. Eckhause, H. Egiyan, L. Elouadrhiri, J. Ficenec, M. Guidal, A. Hancock, F. Hersman, *et al.*, Nuclear Instruments and Methods in Physics Research Section A: Accelerators, Spectrometers, Detectors and Associated Equipment **432** (1999) 265.

[75] G. Adams, V. Burkert, *et al.*, Nuclear Instruments and Methods in Physics Research Section A: Accelerators, Spectrometers, Detectors and Associated Equipment **465** (2001) 414 .

[76] J. O'Meara *et al.*, IEEE Transactions on Magnetics **25** (1989) 1902.

[77] D. Carman, S. Dytman, R. Magahiz, M. Mestayer, R. Miskimen, J. Mueller, R. Schumacher, D. Tedeschi, R. Thompson, and G. Wilkin, Nuclear Instruments and Methods in Physics Research Section A: Accelerators, Spectrometers, Detectors and Associated Equipment **419** (1998) 315 .

[78] J. McAndrew, *Measurement of the G Double-Polarisation Observable in Positive Pion Photoproduction*, Ph.D. thesis, University of Edinburgh (2011).

Appendix A

Scale factors

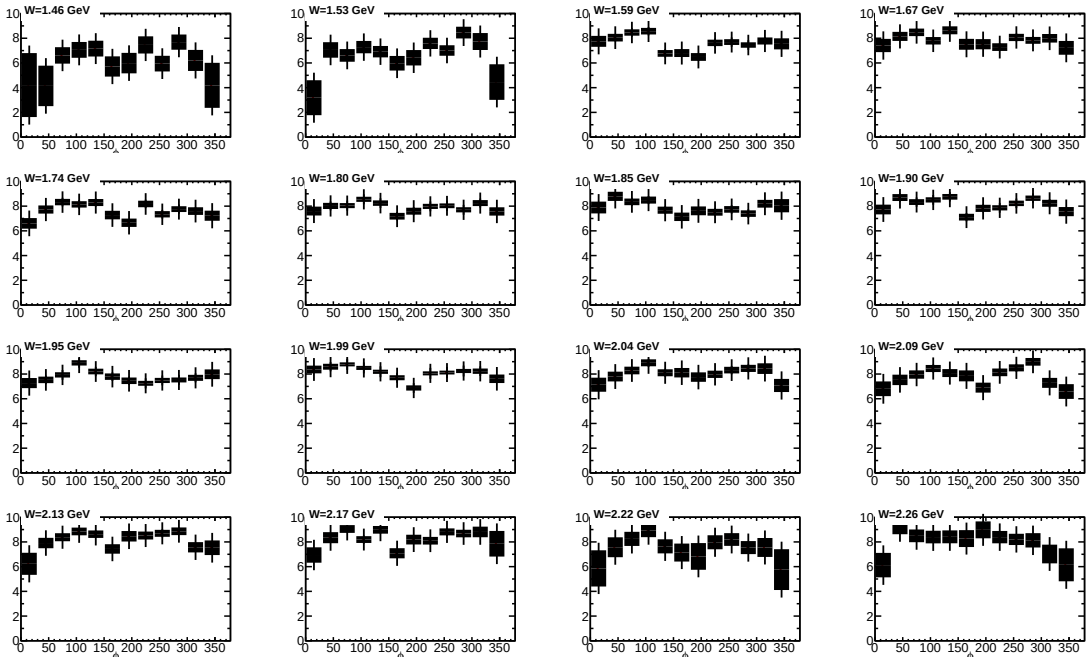

Figure A.1 The scale factor α for topology 1, where all the final-state particles detected. Each distribution is a function of Φ_{CM}.

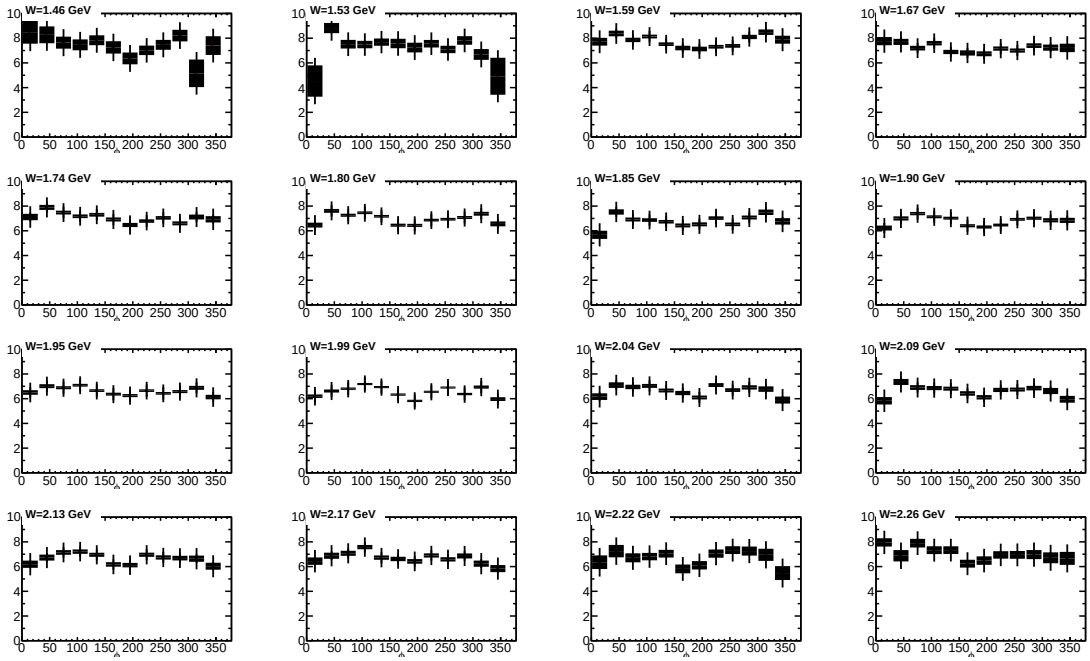

Figure A.2 The scale factor α for topology 2, where the proton is undetected. Each distribution is a function of Φ_{CM}.

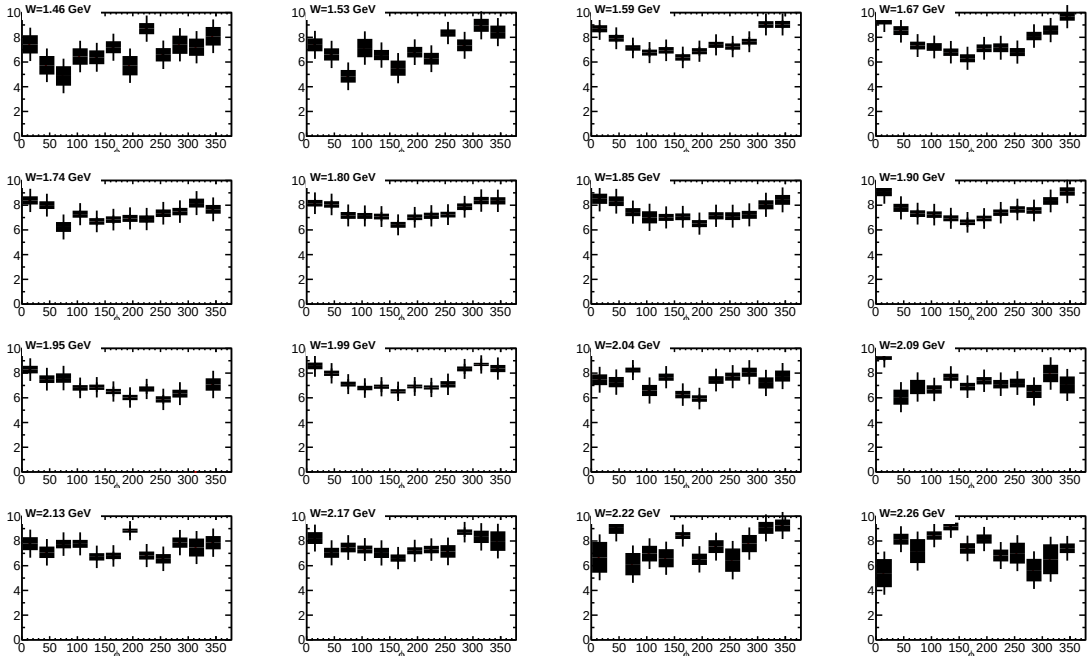

Figure A.3 The scale factor α for topology 3, where the π^+ is undetected. Each distribution is a function of Φ_{CM}.

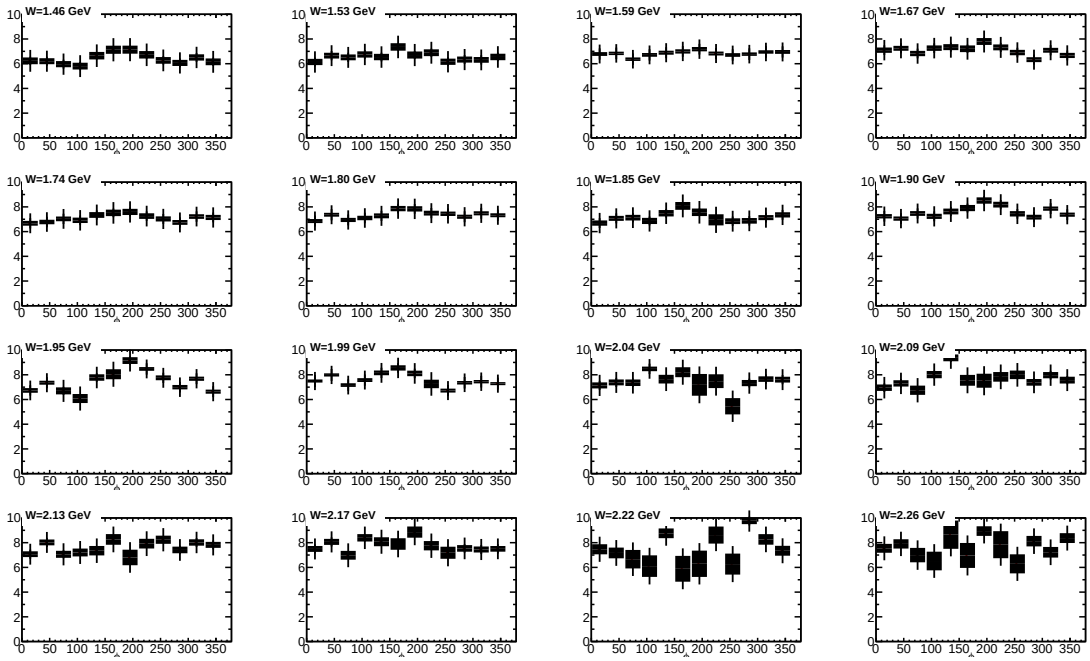

Figure A.4 The scale factor α for topology 4, where the π^- is undetected. Each distribution is a function of Φ_{CM}.

Appendix B

Dilution factors

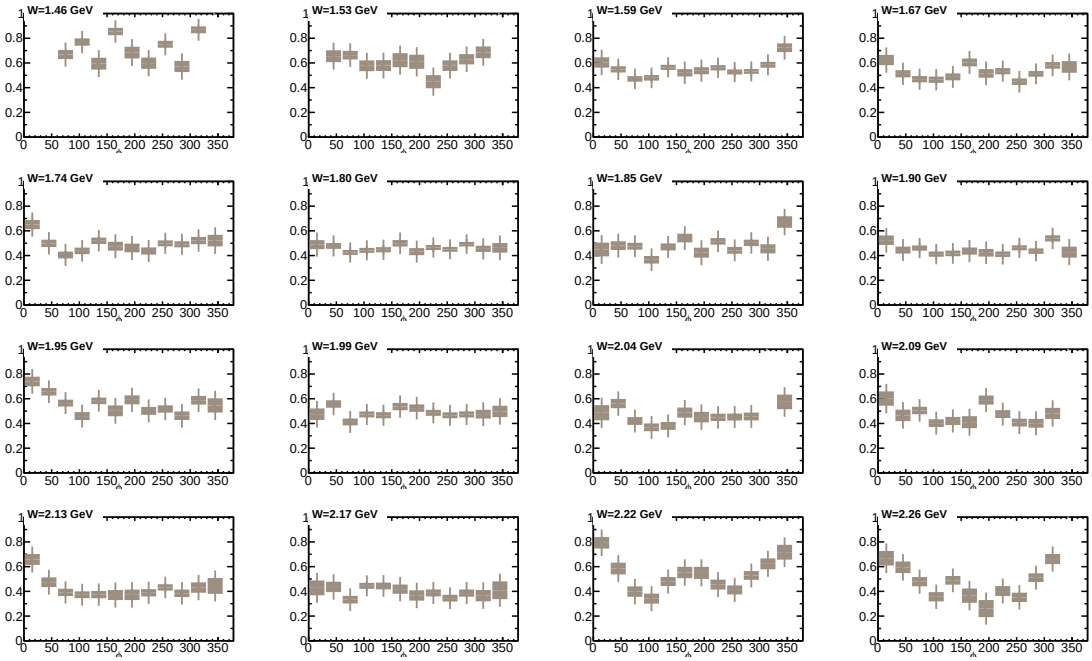

Figure B.1 The dilution factor d_1 for topology 1, where all final-state particles are detected. Each distribution is a function of Φ_{CM}.

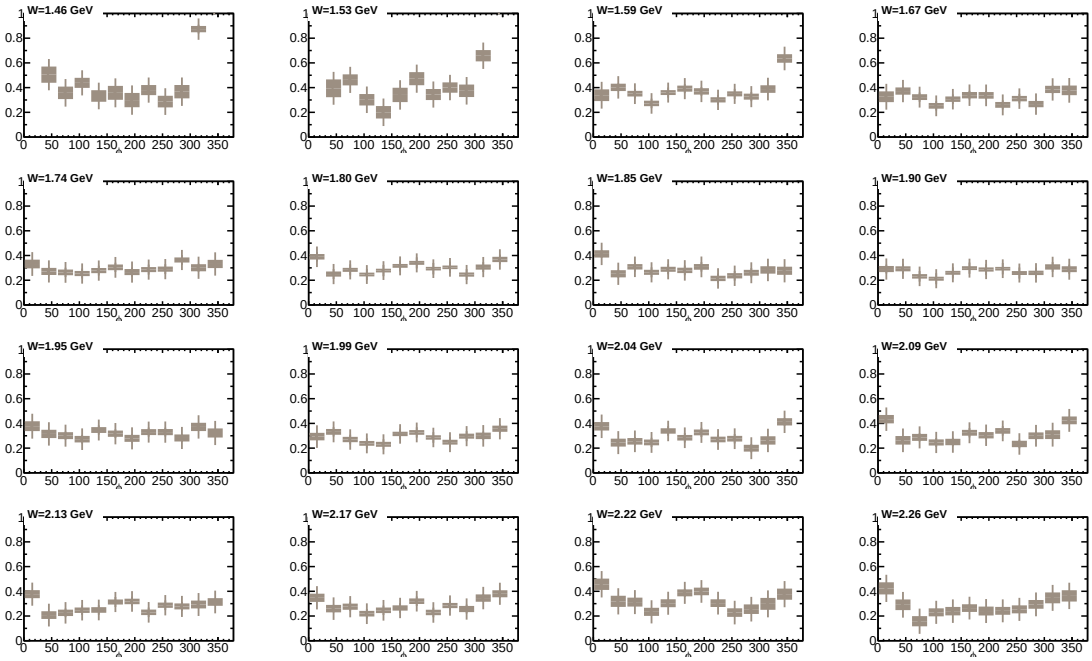

Figure B.2 The dilution factor d_1 for topology 2, where the proton is undetected. Each distribution is a function of Φ_{CM}.

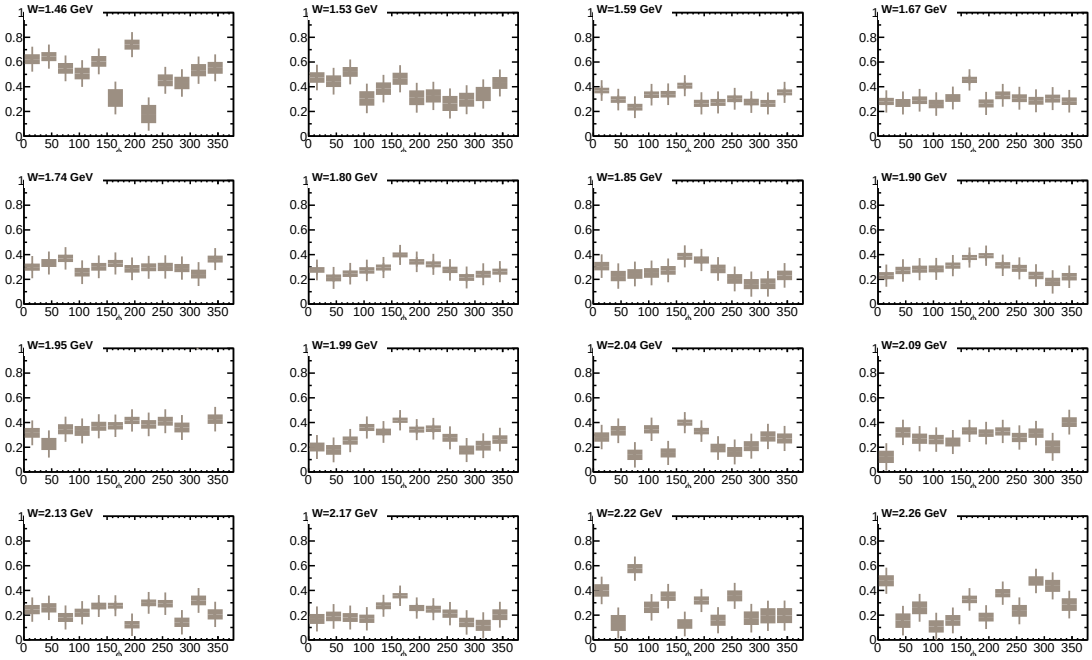

Figure B.3 The dilution factor d_1 for topology 3 where the π^+ is undetected. Each distribution is a function of Φ_{CM}.

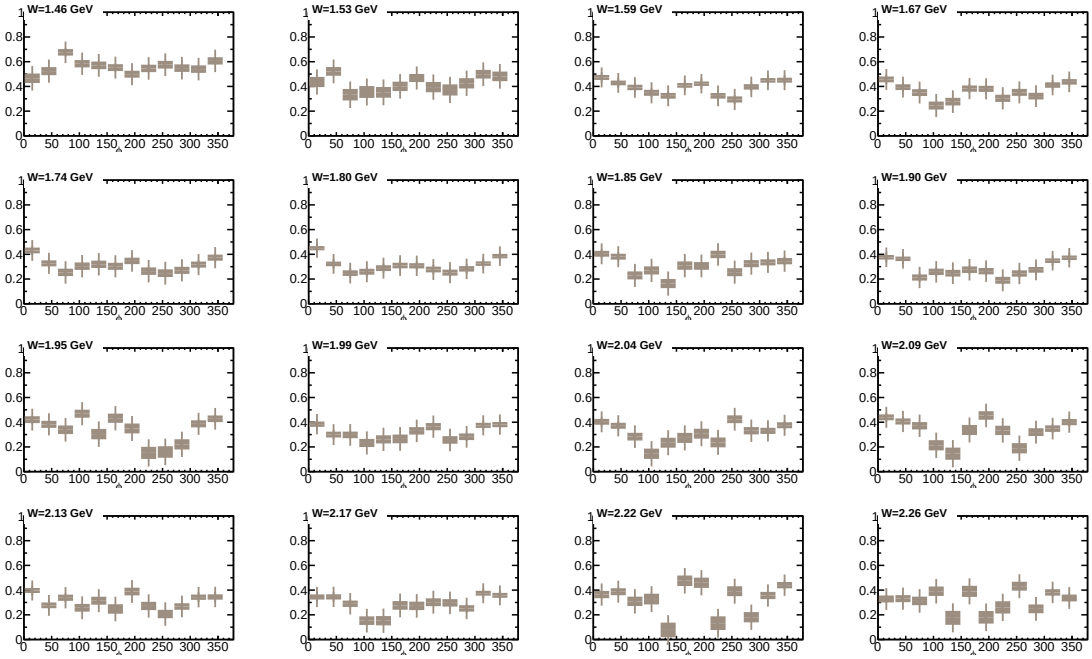

Figure B.4 The dilution factor d_1 for topology 4, where the π^- is undetected. Each distribution is a function of Φ_{CM}.